Spacecraft Environment Interactions

Henry B. Garrett and Insoo Jun
Jet Propulsion Laboratory

1 Introduction 3
1.1 Objectives 3
1.2 Basic Concepts 3
2 Space Environments 10
2.1 Ambient Particulate Environments 10
2.1.1 Overview 10
2.1.2 Solar Energetic Particle Events 11
2.1.2.1 Solar Proton Events 11
2.1.2.2 Heavy Ions 17
2.2 Ambient Photon Environments 18
2.2.1 General Environment 18
2.2.2 X-Ray Flares 23
2.2.3 Interplanetary e^- and H^+ 24
2.2.4 Trapped Radiation 24
2.2.4.1 Geomagnetic Field 26
2.2.4.2 Magnetic and Electric Field Effects 32
2.2.4.2.1 Basic Particle Motion 33
2.2.4.2.2 Invariants of the Particle Motion 36
2.2.4.3 Electron and Proton Belts 39
2.2.4.4 Long-Term and Short-Term Variations 43
2.2.4.5 Examples: Solar Cycle Effects, Storms, Substorms 43
2.2.4.6 AE8/AP8 Comparisons With The Crres Models 44
2.2.4.6.1 Coverage Limitations 44
2.2.4.6.2 Magnetospheric Heavy Ions 46
2.2.4.7 AP-9/AE-9: New Radiation Belt Model (Version Beta) 46
2.2.4.8 Conclusions 51
2.2.5 Extraterrestrial Trapped Radiation 51
2.2.5.1 Jupiter 53
2.2.5.1.1 Introduction 54
2.2.5.1.2 Jovian Coordinate System 56
2.2.5.1.3 Magnetic Field Model 56
2.2.5.1.4 Radiation Belt e^- and H^+ 57
2.2.5.2 Saturn 60
2.2.6 Galactic Cosmic Rays (GRC) 61
2.2.6.1 Overview 61
2.2.6.2 Magnetic Shielding 62
2.2.6.3 GCR Ion Spectra 65
2.2.6.4 GCR Variations 71
2.2.6.5 GCR Electrons 72
2.2.7 Neutral Particle Radiation 73
2.2.8 Nuclear Power Sources 74
2.2.8.1 Radioisotope Thermoelectric Generators (RTGs) 74
2.2.8.2 Radioisotope Heater Unit (RHU) 76

3 Shielding Effects and Interactions with Matter 80
3.1 Radiation-Induced Anomalies: IESD 81
3.2 Single Particle Interactions 85
3.2.1 Photon Interactions 85
3.2.2 Charged Particle Interactions 86
3.2.3 Neutron Interactions 87
3.3 Modeling The Effects Of Shielding 89
4 Radiation Environment Estimates 98
4.1 Example–The Clementine Program 98
4.1.1 AE8/AP8 Radiation Dosage Results 99
4.1.2 Solar Proton Events 102
4.1.3 Summary of Radiation Dosage Estimates 104
4.2 Mars Mission 106
4.3 Jovian Model Applications 109
4.4 Heinrich Flux Estimates 110
5 Conclusion 114
6 Acknowledgements 114
References 115

1 Introduction

1.1 Objectives

As electronic components have grown smaller in size and power and have increased in complexity, their enhanced sensitivity to the space radiation environment and its effects has become a major source of concern for the spacecraft engineer. As a result, the description of the sources of space radiation, the determination of how that radiation propagates through material, and, ultimately, how radiation affects specific circuit components are primary considerations in the design of modern spacecraft. The objective of this paper will be to address the first 2 aspects of the radiation problem. This will be accomplished by first reviewing the natural and man-made space radiation environments. These environments include both the particulate and, where applicable, the electromagnetic (i.e., photon) environment. As the "ambient" environment is typically only relevant to the outer surface of a space vehicle, it will be necessary to treat the propagation of the external environment through the complex surrounding structures to the point inside the spacecraft where knowledge of the internal radiation environment is required. While it will not be possible to treat in detail all aspects of the problem of the radiation environment within a spacecraft, by dividing the problem into these parts–external environment, propagation, and internal environment–a basis for understanding the practical process of protecting a spacecraft from radiation will be established. The consequences of this environment will be discussed by the other presenters at this seminar.

1.2 Basic Concepts

This section will provide an overview of the basic physical concepts and definitions that will be used throughout the presentation. In particular, the concepts of energy, flux, fluence, and dosage will be briefly described. The reader is referred to the many excellent texts on space physics or astronomy for more detailed explanations [1, 2].

Consider first the concept of energy. In the case of particles that have a rest mass, the fundamental equation relating particle mass and velocity to energy is:

$$E = 1/2mV^2 \tag{1}$$

where: m = particle mass

V = particle velocity

E = particle kinetic energy

For photons (which have no rest mass), the equivalent equation is:

$$E = h\nu \tag{2}$$

where:

h = Planck's constant

ν = frequency of the light

The fundamental units of energy E to be used in this study will be the erg, the joule, and electron volt. The erg is the basic unit of energy in the CGS system. It has units of g-cm^{2}-s^{-2}. The joule is the fundamental unit of energy in the MKS system (or "System Internationale") and is in units of 1 kg-m^{2}-s^{-2}. Thus, 1 erg = 10^{-7} joules (in MKS units). The electron volt or eV is also a measure of energy such that 1 eV = 1.602 x 10^{-12} ergs = 1.602 x 10^{-19} joules. It is the kinetic energy that an electron will acquire by being accelerated through an electric potential of one volt.

Closely coupled to the concept of energy is that of dose. Simply put, dose is the total energy accumulated in a given mass of a specific material due to the incident radiation. It is typically given in units of rads or "radiation absorbed dose" for a particular material (the material <u>must</u> be specified because energy absorption is dependent on the material). As an example, for silicon, 1 rad (Si) =100 ergs/g (Si). The corresponding unit for dose in the MKS system is called the gray. 1 Gy (gray) = 1 joule/kg = 100 rad =10^{4} ergs/g. Here we will, without exception, use the older unit "rad" as this is still the "preferred" unit in space physics and radiation effects analysis. It needs to be emphasized that, for the same incident flux, different materials will be affected differently dependent on the composition of the incoming radiation and the composition of the absorbing material. Other units such as the roentgen (quantity of γ- or X-rays that deposit, by ionization and energy absorption, 83 ergs/g in dry air) or the rem (roentgen equivalent per man) are also often used but will not be discussed here.

In addition to the energy and composition of a particle or photon, it is also necessary to describe how many of them there are. This is usually done in terms of intensity or flux and, when speaking in terms of a time interval, fluence. Confusion arises over the concepts of intensity/flux and fluence because there are many different ways to define these quantities. Here we will define the quantity "unidirectional differential intensity" $j(E,\theta,\varphi,t)$ as:

"The flux (number of particles or photons per unit time) of a given energy E per unit energy interval dE in a unit solid angle $(d\Omega = 2\pi\cos\theta\, d\theta\, d\varphi)$ about the direction of observation (in the θ,ϕ direction), incident on unit of surface area (dA) perpendicular to the direction of observation."

This is illustrated in Fig. 1 [2]. Typical units are particles-cm^{-2}-s^{-1}-sr^{-1}-KeV^{-1} for protons or electrons and particles-m^{-2}-s^{-1}-sr^{-1}-MeV^{-1}-μ^{-1} for heavy ions (where μ is "nucleon")–a typical spectrum for iron cosmic rays is presented in Fig. 2 [3]. The "unidirectional integral intensity"

(or flux) is defined as the intensity of all particles with energy greater than or equal to a threshold energy E:

$$j_{\geq E} = \int_{E}^{\infty} j dE \tag{3}$$

with units of particles $cm^{-2}s^{-1}sr^{-1}$

FLUX

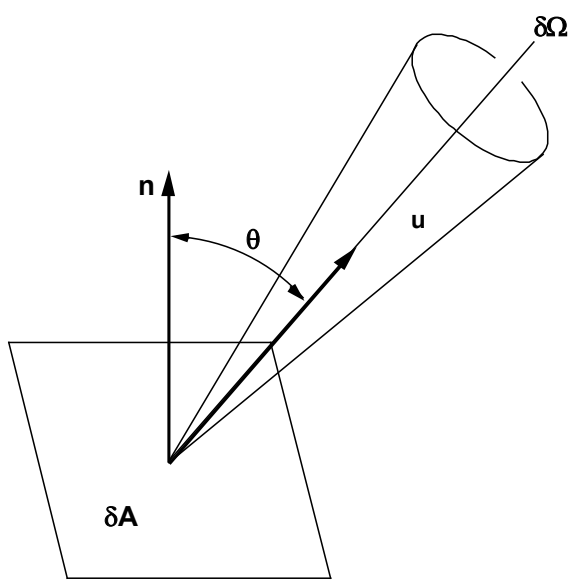

Figure 1. The flux (number of particles or photons per unit time) of a given energy E per unit energy interval dE in a unit solid angle $(d\Omega = 2\pi \cos\theta \; d\theta \; d\phi)$ about the direction of observation (in the θ, ϕ direction), incident on unit of surface area (dA) perpendicular to the direction of observation [2].

We define the "omnidirectional flux" J as:

$$J = \int_{4\pi} j d\Omega \tag{4}$$

Fluence I is the integral of the flux over a given time interval (i.e., one hour, one year, etc.):

$$I = \int_{\delta t} j dt \tag{5}$$

Here, when we refer to omnidirectional fluence I(≥E), we will normally mean the "omnidirectional integral (in energy) fluence" such that:

$$I_{>E} = \int_E^{\infty} dE \int_{4\pi} d\Omega \int_{\delta t} j dt \tag{6}$$

The units of this quantity are particles-cm^{-2} for some specified threshold energy E (typically 1 MeV or higher for radiation effects) and for a specified time interval (often 1 year).

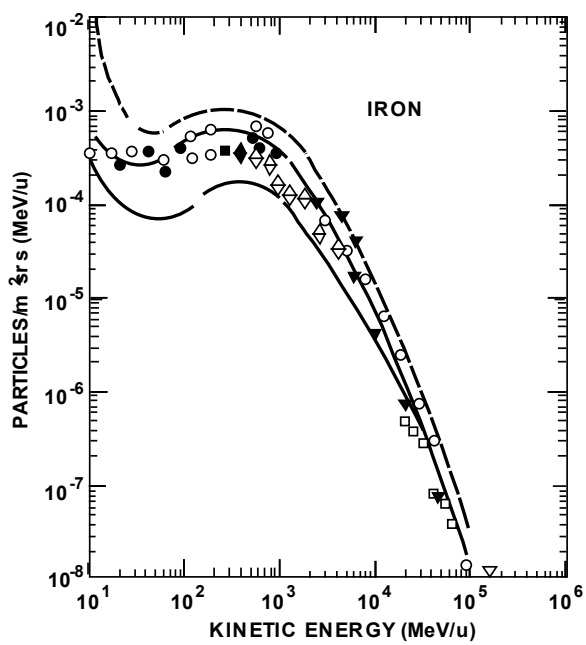

Figure 2. The cosmic ray iron spectrum: The solid curves are for solar maximum (lower) and solar minimum (upper). The dashed curve is the 90% worst-case iron spectrum, which is implied by comparison with the cosmic ray helium spectrum [3].

To allow comparisons between different energies, particle types, and dosages, it is common practice to talk in terms of "1-MeV equivalent" (typically 1-MeV electrons or 1-MeV neutrons in silicon). First, the energy dependence of the damage and energy content of the spectra for the environment to be considered are used to determine what fluence of 1-MeV particles (electrons or neutrons) would produce the same amount of damage or dose in the material (typically silicon or aluminum). A curve for neutrons, in units of MeV-mb (where b is a barn or 10^{-24} cm^2 and the "relative displacement damage" is defined in terms of the cross section times the energy of the incident particle), is given in Figure 3 [4]. As an illustration, for 14 MeV neutrons, the 1-MeV neutron dose damage equivalent is given by multiplying the 14 MeV dose

by 2.5 (obtained from Fig. 3). (Note: because of variations in the damage parameter with material and property, it should always be kept in mind that the use of a damage equivalent is not exact but an approximation for comparison purposes.)

A final quantity related to energy absorption and flux to be used here is the Linear Energy Transfer or LET. The LET is the energy transferred by radiation per unit length of absorbing material. That is LET = dE/dx. For ionization and excitation effects, it is often expressed in MeV/μm of the primary particle track length or, if the density of the material is known, MeV-cm^2-mg^{-1} (this is typically the "unit" when the reference is to an LET between 1 and 30 and is given by: $\frac{1}{\rho}\frac{dE}{dx}$).

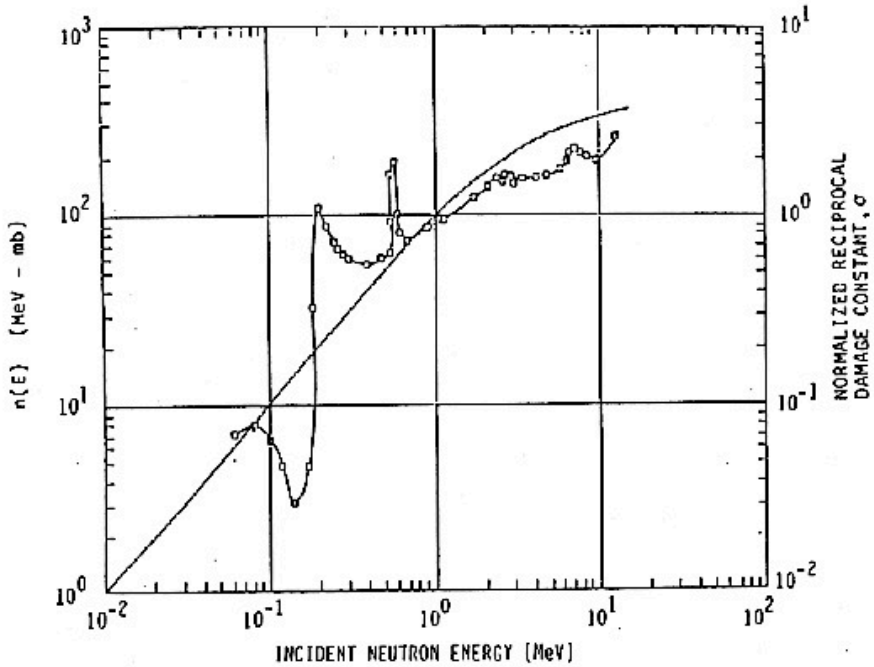

Figure 3. Illustration of a neutron displacement damage equivalence curve. The curves (actual and fitted), in units of MeV-mb (where b is a barn or 10^{-24} cm^2), are for neutrons. The "relative displacement damage" is defined in terms of the cross section times the energy of the incident particle. As an example, for 14 MeV neutrons, the 1-MeV neutron dose damage equivalent is given by multiplying the 14 MeV dose by 2.5 [4].

The concept of LET can be crudely derived as follows. First assume a target of mass *M*, density ρ, area δA, and thickness $\delta\tau$:

$$\delta\tau = \frac{M}{\rho\delta A} \tag{7}$$

Next approximate the fluence (number *N* of particles per unit area δA normal to target surface) versus energy. Call this *f(E)* at energy *E* by:

$$f(E) \approx \frac{N(E)}{\delta A} \tag{8}$$

Estimate energy change δE in crossing target thickness $\delta\tau$ for particle energy E:

$$\delta E \approx \delta\tau \left.\frac{dE}{dx}\right|_E \tag{9}$$

The dose per particle of energy E is approximated by:

$$D(E) \approx \frac{\delta E}{M} \approx \left.\frac{dE}{dx}\right|_E \frac{\delta\tau}{M} \approx \frac{1}{\rho}\left.\frac{dE}{dx}\right|_E \frac{1}{\delta A} \tag{10}$$

The total dose at energy E is then:

$$D_T(E) \approx ND(E) \approx \frac{1}{\rho}\left.\frac{dE}{dx}\right|_E f(E) \tag{11}$$

Finally, for total integral dose, integrate over the range E_0 to ∞. The LET, $\frac{1}{\rho}\frac{dE}{dx}$, and the fluence, *f(E)*, are fundamental to the determination to dose.

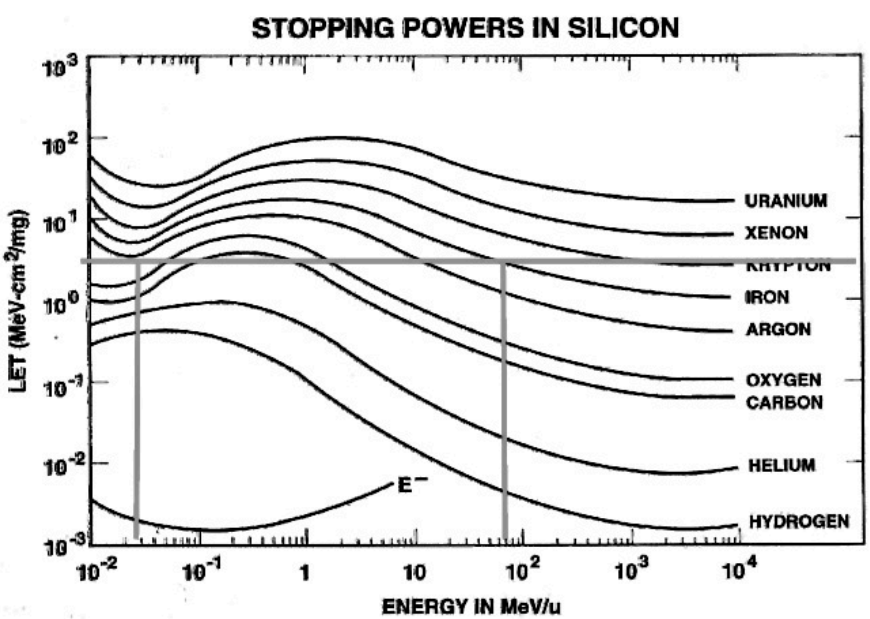

Figure 4. Linear Energy Transfer Function (LET) versus energy per atomic mass unit (AMU) for particles in silicon [3]. The horizontal line corresponds to a given LET value. The vertical lines are the energies for Iron that correspond to that LET. As illustrated, there can be multiple values of energy that correspond to the same value of LET.

The concept of LET is also important when discussing single event upsets (SEU) or "soft errors". These occur when a particle, typically an ionized, high energy atomic nucleus, deposits enough energy in the sensitive region of an electronic device to cause a change in the logic state of the device. Upsets occur only when the energy deposited exceeds a critical level in the

sensitive region of the device. This is often computed in terms of LET. When viewed as a function of LET, the probability of upset is, in its simplest form, a threshold phenomenon: any particle with a minimum LET (L_o) or greater will cause an upset. This behavior is illustrated in Fig. 4 where the energy deposited per unit length (LET) is plotted versus incident particle energy–note how the curve has a peak rate. A useful way of presenting the environment in terms of LET is the Heinrich curve. The Heinrich curve gives the integral flux as a function of LET rather than particle energy. The Heinrich flux F_H is the flux of particles for a single species with a (threshold) LET of LET_1 or greater:

$$F_H(LET_1) = \int_{LET_1}^{\infty} F_H(LET)\,d(LET) \tag{12}$$

where: F_H is the particle flux for the species as a function of LET rather than energy and for LETs greater than or equal to the threshold LET_1 (a representative integral Heinrich curve for iron is plotted in Fig. 5 [5]). As the LET depends not only on particle energy but the target material as well, the LET versus energy curve will be different for all particle species. Experiments have shown, however, that to first order it is the LET which is important for determining upsets and not the particle energy or its species. The Heinrich flux versus LET plot is the principal means of presenting radiation data for use in SEU calculations just as the particle flux versus energy is the main means of presenting radiation data for dosage calculations.

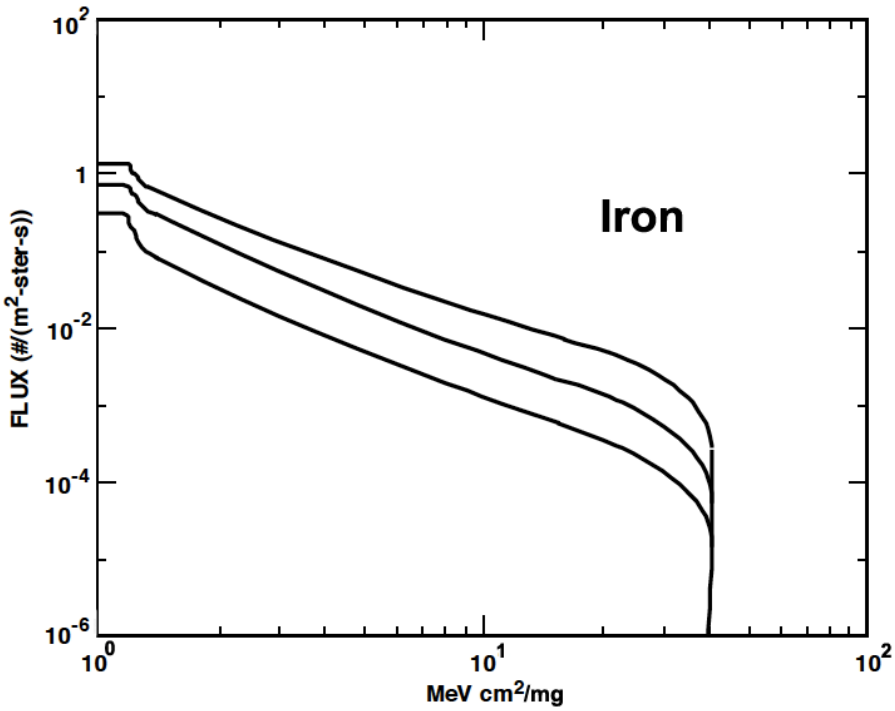

Figure 5. Integral fluxes for iron cosmic rays versus LET [3] for the differential iron flux spectra versus energy per AMU in Fig. 2 for a 90% worst case (upper), solar minimum (middle), and solar maximum (lower). The spectra are at 1 AU behind 25 mils of aluminum shielding.

To summarize, this section has defined the basic terminology used to describe the radiation environment. "Dose", "Flux/Intensity", "Fluence", "LET", and "1-MeV Equivalent" have been defined. The reader is referred to books and articles by Roederer [2], Smart and Shea [6], and others for more complete descriptions of these concepts.

2 Space Environments

2.1 Ambient Particulate Environments

2.1.1 Overview

The high energy particle radiation environment responsible for effects on electronics is usually considered to consist of electrons with energies greater than 100 KeV, protons or neutrons with energies greater than 1 MeV, and heavy ions with energies above 1 MeV/nucleon (note: in reality energies as low as a few eV can contribute to radiation effects on materials, particularly surfaces but those will not be considered here). The populations are characterized in terms of their kinetic energy, charge state (or lack thereof), and composition. Unlike photons which travel uniformly at the speed of light, particles can vary in velocity from a few m/s up to a

sizable fraction of the speed of light in the case of cosmic rays. The discussion will be roughly divided into five families of radiation based on these characteristics:

1) Protons and other heavy nuclei associated with solar proton events.
2) Trapped radiation (for the Earth, the Van Allen Belts);
3) Galactic Cosmic Rays which consist of interplanetary protons, electrons, and ionized heavy nuclei;
4) Neutrons (primarily Cosmic Ray Albedo Neutrons or CRAN particles).
5) Photons (γ-rays, X-rays, UV/EUV, Optical, Infra-Red, and Radio)

The first of these is highly variable on the scale of minutes to a few days in response to events on the Sun. The next two sources are relatively constant or change on long time scales of days to years (e.g., the 11 year solar cycle). The fourth is a secondary population because the relatively short lifetime of neutrons severely limits any solar produced fluxes at 1 AU or beyond. The fifth source is the electromagnetic spectrum. Of importance here are the γ-rays, X-rays, and UV/EUV photons. Each type of radiation has a characteristic spectrum and preferred interaction mode with matter that supports this simple division. They will be discussed separately in the following sections.

2.1.2 Solar Energetic Particle Events

2.1.2.1 Solar Proton Events

A Solar Energetic Particle (SEP) or Solar Proton Event (SPE) are names for a very energetic process, and potentially damaging situation that occurs when very strong magnetic fields in the solar photosphere reach a critical instability. On time scales of seconds, the strong fields are unstable enough to "snap", thereby adjusting and relaxing to remove the instability. A considerable amount of energy, up to 0.1% of the total solar energy output or about 10^{32} ergs, is released during this solar event. A solar flare typically lasts from a few minutes to a few hours and heats the surrounding corona to temperatures in excess of 2×10^7 K. Associated with the heating, large fluxes of atomic particles, primarily electrons and protons, are accelerated and expelled from the Sun (so-called coronal mass ejections or CMEs). There are also substantial radio bursts and X-ray emissions. Many of the particles escape the Sun and into the interplanetary medium where they follow the solar wind magnetic field out through the ecliptic plane into interstellar space. As a result of the complexity of this field structure, both the intensity and the spectrum of the particles observed at Earth can vary significantly with position. These quantities depend critically on the positions of the Earth and the flare on the Sun relative

to each other. Variations as large as 100 in the particle fluxes from the same event at different points around the Earth's orbit have been observed. A schematic illustrating the time scales for the different solar flare events is presented in Fig. 6 (the 27 day period is the approximate rotation rate of the Sun as seen from the Earth). Note that solar particle events are typically divided into two classes: a) Gradual Events: These are typically the largest events and associated with CME shocks. They typically last for several days; b) Impulsive Events: Often called Solar Flares, these are short, longitudinally localized events on the solar surface. There are usually less than 10 gradual events a year. The particle abundances in these events are similar to the solar corona's. They have sharp rise times and decay slowly over hours to days and cover a large longitudinal extent. The impulsive events, associated with instabilities on the solar surface are rich in heavy ions and show a sharp peak in X-rays. These two types of events are illustrated in Fig. 7.

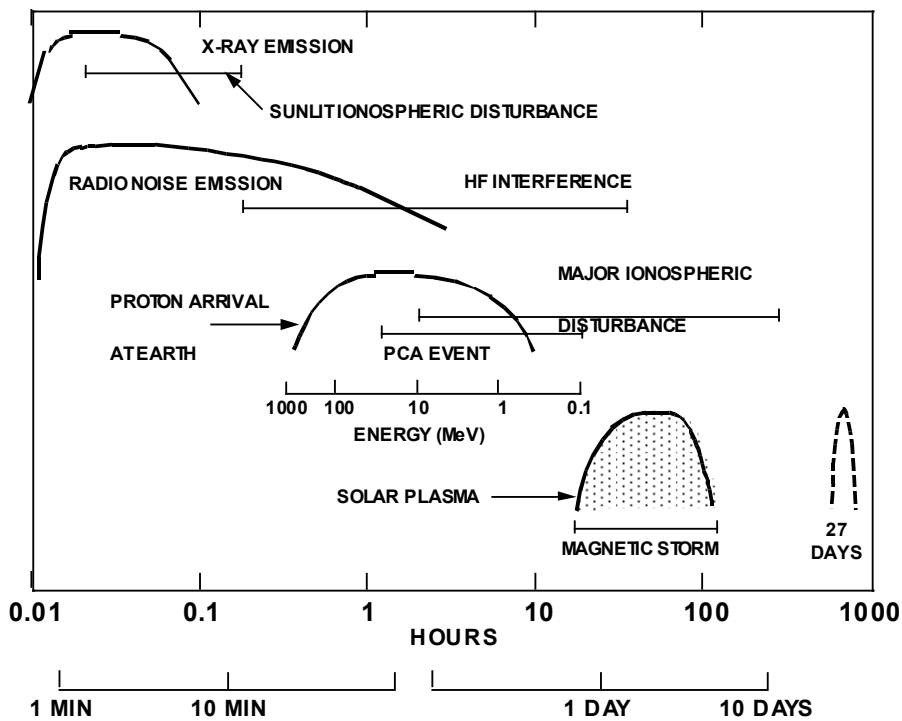

Figure 6. Schematic plot of the relative variations in time of the amplitudes of the X-ray, radio noise, high energy particle, and solar plasma fluxes for a "typical" large solar flare.

The intensity and number of very large solar events (CMEs) varies dramatically from solar cycle to solar cycle (Fig. 8). The seeming lack of correlation between sunspots and proton events in Fig. 8 illustrates the difficulty in reliably predicting the level or frequency of activity for the future (see, however, Feynman et al. [7]). Adding to the problem is that most data on large solar events is from only the last few cycles making statistical studies very difficult. One

fact is clear, however, and that is that solar event related effects occur far more frequently during solar maximum (Fig. 9). Although solar flares are less frequent during solar minima, these flare related effects can be greater in the terrestrial magnetosphere because the interplanetary fields, through which the flare particles travel, are less complicated and the particles can more easily gain access to the Earth's polar caps. As an example, even though the number of geomagnetic storms goes down during minima in solar activity, the level of a given storm, even during the lowest levels of solar activity, can be among the highest ever seen. A particularly good example was the great solar proton event of 1972 which occurred nearly 4 years after the peak in solar activity. It is compared in Fig. 10 with the large event in October 1989 for E>10 MeV protons.

The intense fluxes of high energy protons that are associated with the solar proton events are very damaging to electronics both from the SEU and total dose standpoint (note: solar proton events are often referred to as solar flares; strictly speaking, a solar flare, which involves many processes, may or may not have a classifiable proton event). Hydrogen and heavy nuclei in the ~1 MeV/nucleon to ~10 GeV/nucleon energy range are ejected during solar proton events. Their intensities are generally a few to several orders of magnitude larger than those of GCR at these lower energies, depending obviously on the size of solar flare. Adams and his collaborators at the Naval Research Laboratory (NRL) have developed several detailed models of the radiation environment associated with a flare [3, 8-10]. Typically, these and other flare models are based on the large proton event of 1972.

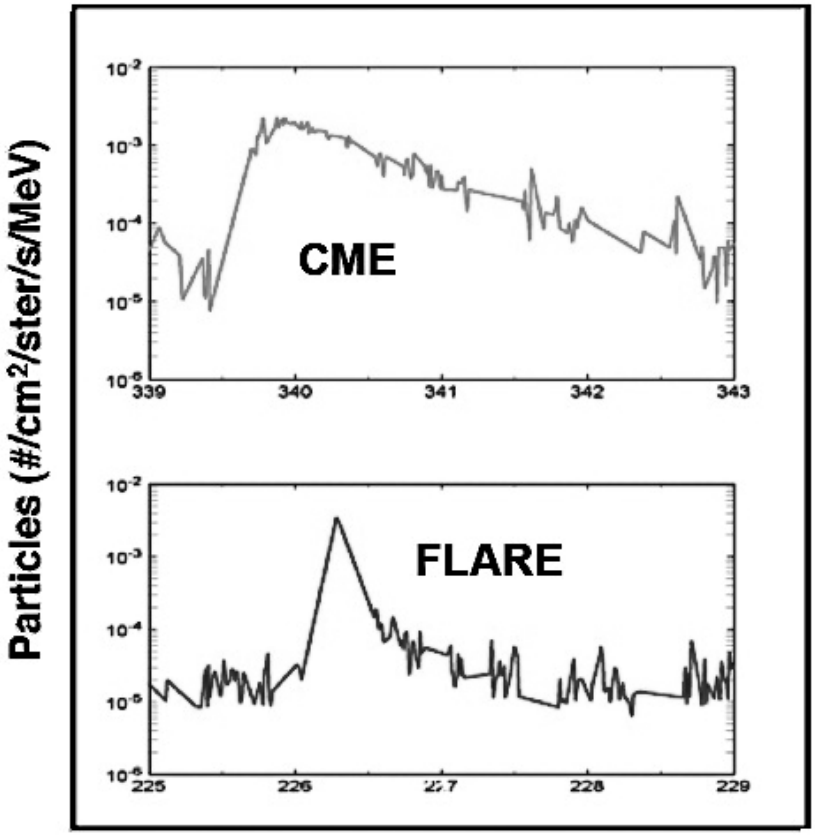

Figure 7. Two types of solar proton events: a) Gradual Events: These are typically the largest events and associated with CME shocks. They typically last for several days; b) Impulsive Events: Often called Solar Flares, these are short, longitudinally localized events on the solar surface [11].

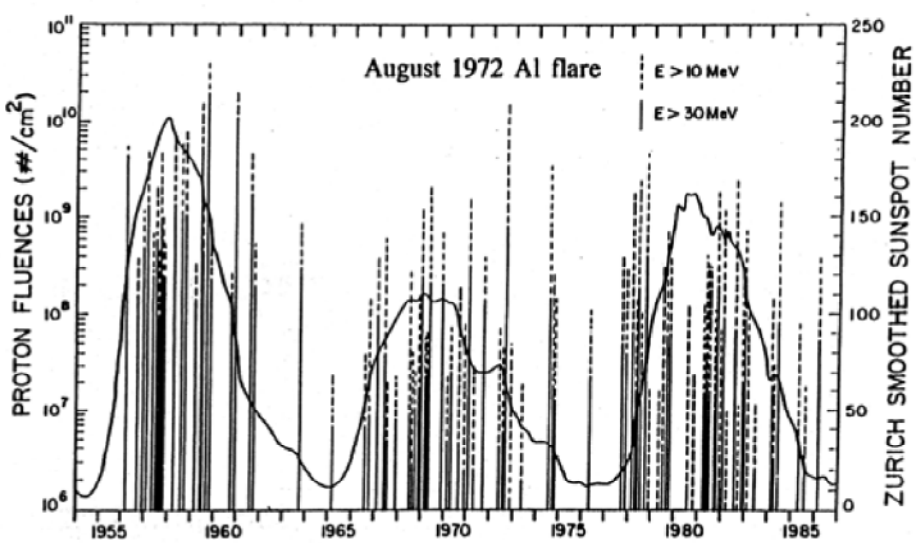

Figure 8. Large solar proton fluences (vertical lines) superimposed on the sunspot cycle (continuous curve). Solid lines correspond to E>30 MeV, dashed lines to E>10 MeV proton fluences.

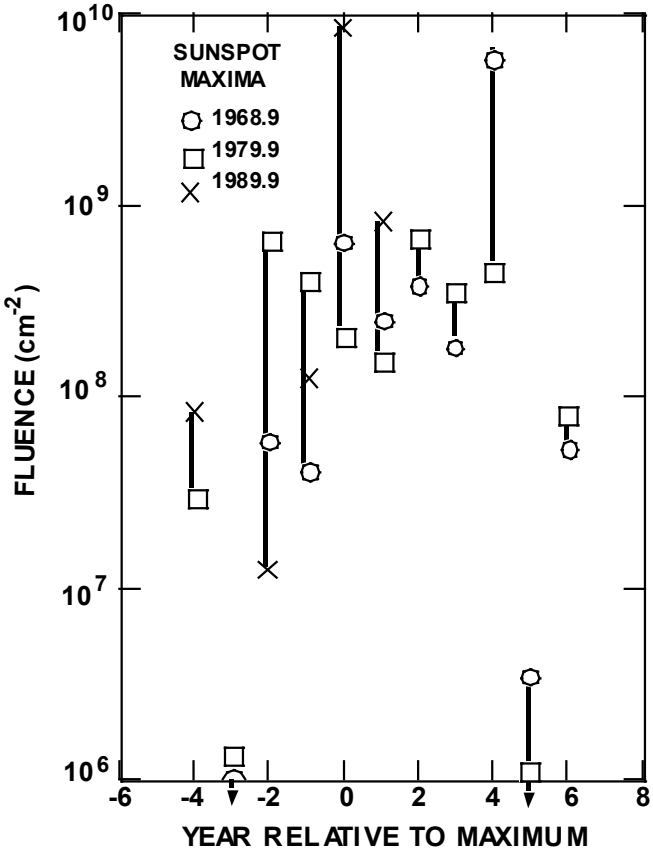

Figure 9. Yearly Event Fluences for Protons of Energy >30 MeV vs Year Relative to Sunspot Maximum [7].

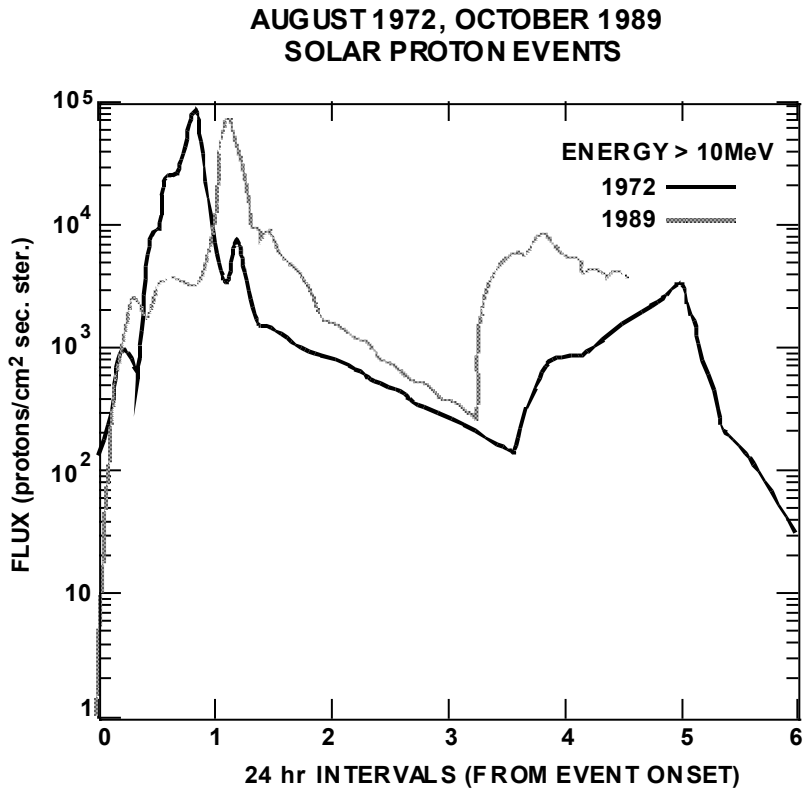

Figure 10. Comparison of the E > 10 MeV proton flux as a function of time for the great solar proton events of August 1972 and the October 1989.

For many years, there has been an ongoing discussions over how to model the probability of the occurrence of solar flare proton events and to estimate their radial variations. Feynman and colleagues have developed a comprehensive model of these events that largely replaces previous models [7]. A major change has been the realization that instead of there being three types of flares (typical, worst-case, and anomalously large) in terms of energy output, there is indeed a continuum when the total output energy of the solar proton events in a series is integrated. In fact, when plotted in terms of the statistical occurrence frequency, it was found that the likelihood of the occurrence of a solar proton event amplitude in a given time interval could be predicted. This model, as represented in Figures 11 and 12 [7], has been used to estimate the likelihood of encountering a given mission-integrated fluence for various interplanetary spacecraft. Fig. 11 plots the cumulative probability of occurrence of a solar proton event fluence of the indicated level or less between 1963 and 1991 (the scale is for a log normal probability such that a log normal distribution will be a straight line). Fig. 12 uses these data to predict the probability of seeing a total proton dose (E>10 MeV) equal to or less than the graphed value for various mission lengths during solar maximum (the 7 years centered around solar maximum–the other 4 years are assumed to have 0 flux). Similar plots are available for other energy intervals and are currently being extended to other ions. In a later subsection, these data are used to estimate the total dose due to protons on a representative space mission.

Feynman and Gabriel [12] assume a (conservative) radial dependence of r^{-3} for the flux inside 1 AU and a radial dependence of r^{-2} outside 1 AU. This implies that the fluence and dose will be trajectory dependent for interplanetary vehicles such as Galileo and Cassini.

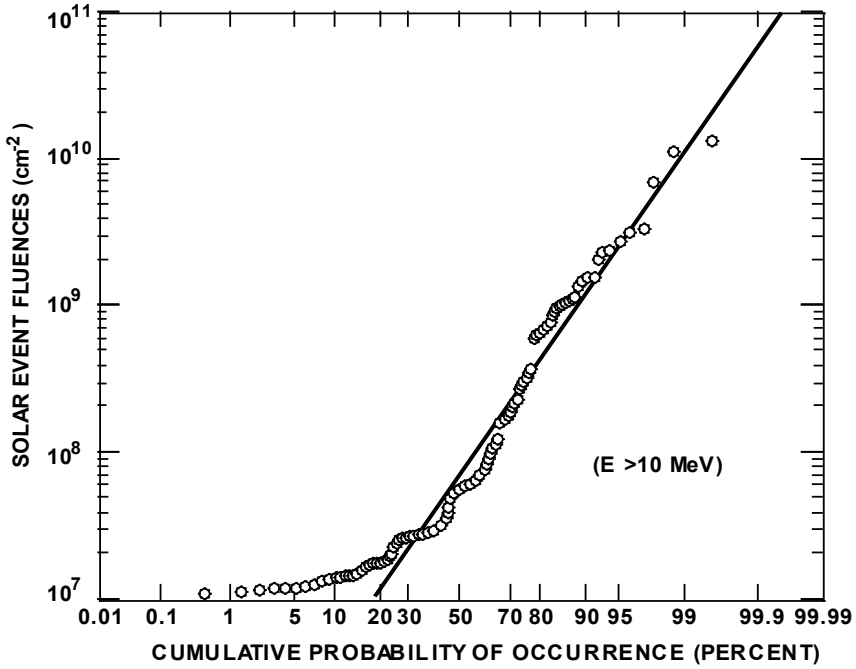

Figure 11. Distribution of Solar Event Fluences for Solar Active Years between 1963 and 1991 for Protons of Energy > 10 MeV for which Daily Averaged Flux exceeds 1.0 cm^{-2}-s^{-1}-sr^{-1}. The straight line is the selected log normal distribution. [7]

2.1.2.2 Heavy Ions

In addition to intense proton fluxes, solar flare events also typically are accompanied by small but variable amounts of heavy ions. Tables 1 and 2 [9] summarize the abundances of the heavy ions found in solar particle events relative to hydrogen. The abundance ratios from the tables are multiplied by the proton spectrum to get the individual ion spectra. For the Adams' model, the worst-case composition for the elements from copper to uranium can be estimated by multiplying the abundance ratios of Table 2 by 1.92 exp ($z^{.79}$/6.89). Although the solar heavy ions are usually assumed to be fully ionized, they may not be, particularly in the $0.5 \leq E \leq 2.5$ MeV/nucleon energy range [13]. Fischer et al. [14] and MeWaldt and Stone [15] showed that solar energetic heavy ions in the energy range $5 \leq E \leq 20$ MeV/nucleon may also not be fully ionized and that the upper limits on the charge to mass ratio of the heavy ions may be as low as 0.1 (~0.5 for fully ionized heavy ions). Breneman and Stone [16] have indirect evidence that heavy ions in the energy range 3.5 to 50 MeV/nucleon may have the same distribution of charge states as for the 0.5 to 2.5 MeV/nucleon ions observed by Luhn et al. [13]. The importance of the charge state of the ions is that it affects their entry into the Earth's magnetosphere–the higher

the charge state of a given atomic species, the less likely it is to get through the Earth's magnetic field for the same energy. Heavy ion maximum design fluxes versus LET for SPE intervals of 5 minutes, 1 day, and 1 week behind 25 mils of aluminum shielding as given by the CREME96 model are compared with the GCR at solar minimum (when the GCR flux is a maximum) in Fig. 13. Fluxes are to be used for determining SEU rates at a solar distance of 1 AU.

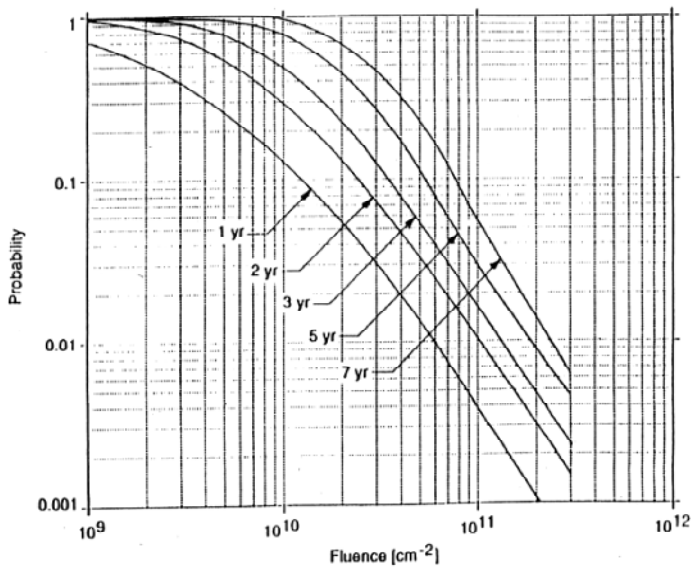

Figure 12. Fluence Probability Curves for Protons of Energy Greater than 10 MeV for Various Mission Lengths [7].

2.2 Ambient Photon Environments

2.2.1 General Environment

Fig. 14 illustrates the solar photon spectrum. This document shall discuss the electromagnetic radiation environment in two frequency ranges (although there is an ambient γ-ray environment, this population does not contribute significantly to radiation effects on microelectronics and will not be considered here):

1) Optical (infrared, visible, UV): 10^{12} Hz-10^{16} Hz
2) EUV/X-ray: 10^{16} Hz-10^{21} Hz

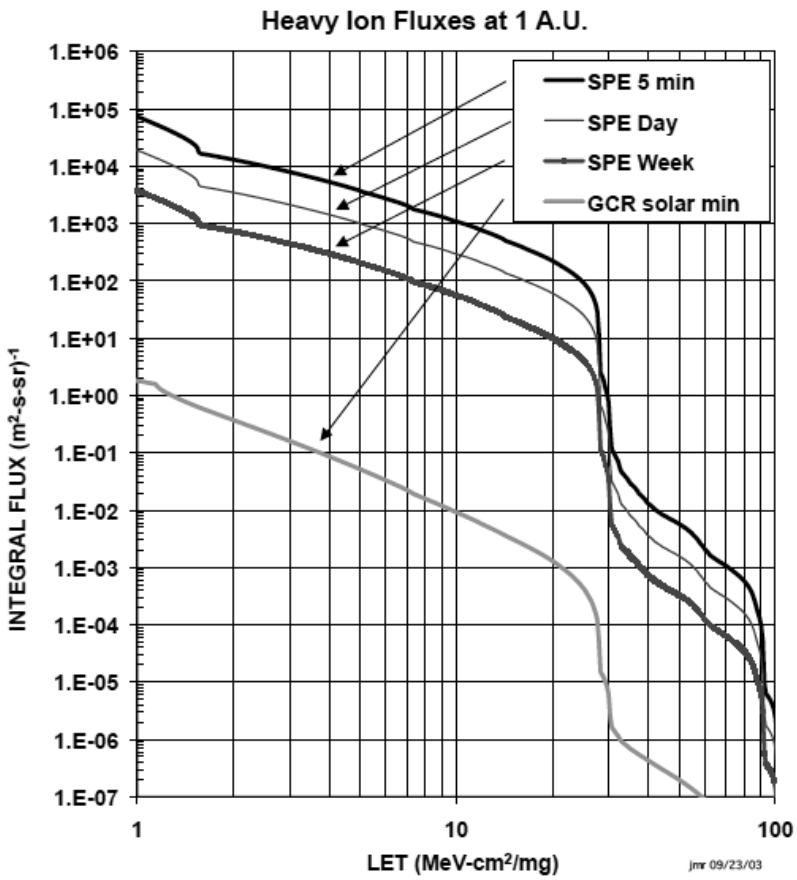

Figure 13. Heavy ion maximum design fluxes for the GCR at solar minimum (when the GCR flux is a maximum) and SPE intervals of 5 minutes, 1 day, and 1 week behind 25 mils of aluminum shielding as given by the CREME96 model. Fluxes are to be used for determining SEU rates at a solar distance of 1 A.U. Courtesy M. Ratliff, JPL.

First consider the infrared and visible spectrum. The visible (~3500 Å to ~7000 Å) and infrared (~0.7 mm to ~7 mm) portions of the spectrum are dominated by the solar flux. As shown in Fig. 14 [17], the solar spectral irradiance peaks between ~4500 Å to ~7000 Å and accounts for most of the solar constant, the total solar energy flux just outside the Earth's atmosphere. It is currently estimated to be ~1370 W/m^2 (~8.4 x 10^{11} MeV/cm^2-s or 1.96 cal-cm^{-2}-min^{-1}). Although there are additional sources of visible and infrared light (such as light reflected by the Moon, atmospheric dayglow, infrared radiation from the Earth, and light from auroral displays), these contribute little to the penetrating radiation environment as defined in this report (they are, of course, critical to the detailed thermal balance of a spacecraft) and will not be discussed further.

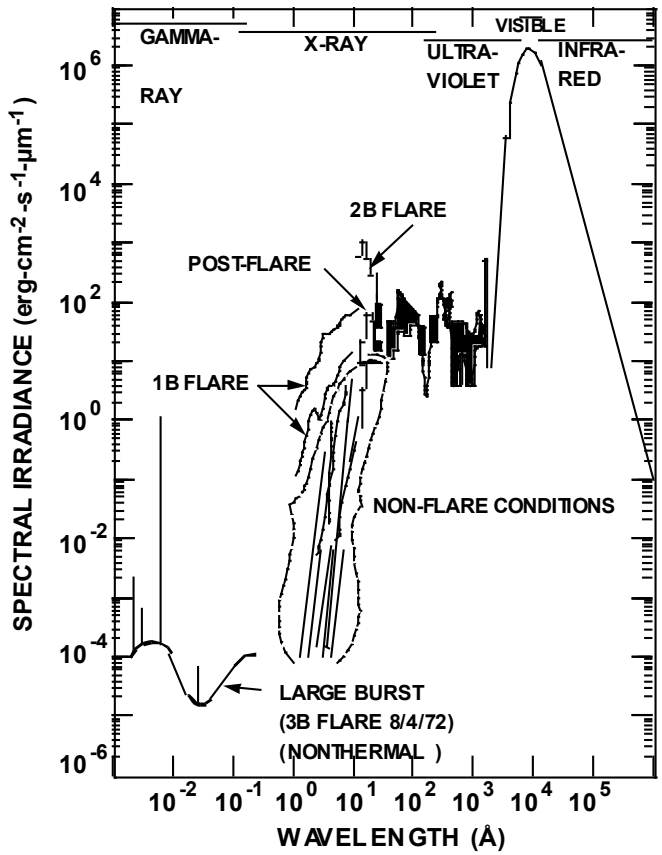

Figure 14. The spectral distribution of solar irradiance [17] from a wavelength of 10^{-3} Å to 10 m.

Table 1. Mean and Worst-Case Solar Particle Event Composition for Low Z Ions. [3]

Element	Mean case	Worst case	Element	Mean case	Worst case
H	1	1	P	2.3×10^{-7}	1.1×10^{-6}
He	1.0×10^{-2}	3.3×10^{-2}	S	8.0×10^{-6}	5.0×10^{-5}
Li	0	0	Cl	1.7×10^{-7}	8.0×10^{-7}
Be	0	0	Ar	3.3×10^{-6}	1.8×10^{-5}
B	0	0	K	1.3×10^{-7}	6.0×10^{-7}
C	1.6×10^{-4}	4.0×10^{-4}	Ca	3.2×10^{-6}	2.0×10^{-5}
N	3.8×10^{-5}	1.1×10^{-4}	Sc	0	0
O	3.2×10^{-4}	1.0×10^{-3}	Ti	1.0×10^{-7}	5.0×10^{-7}
F	0	0	V	0	0
Ne	5.1×10^{-5}	1.9×10^{-4}	Cr	5.7×10^{-7}	4.0×10^{-6}
Na	3.2×10^{-5}	1.3×10^{-5}	Mn	4.2×10^{-7}	2.3×10^{-6}
Mg	6.4×10^{-5}	2.5×10^{-4}	Fe	4.1×10^{-5}	4.0×10^{-4}
Al	3.5×10^{-6}	1.4×10^{-5}	Co	1.0×10^{-7}	5.5×10^{-7}
Si	5.8×10^{-5}	1.9×10^{-4}	Ni	2.2×10^{-6}	2.0×10^{-5}

Next consider the UV, EUV, and X-ray portion of the spectrum. As in the case of the visible and infrared portions of the spectrum, the Sun generally dominates the short wavelength portion of the spectrum in direct sunlight. The shortest wavelengths, 10 Å-100 Å or less, are referred to as X-rays. This spectral range is important because it contributes to the ionization of the E-region. The spectral region from about 100 Å to 1000 Å, called extreme ultraviolet or EUV, is related to the photoionization processes of O_2, N_2, and O in the ionosphere and to thermospheric heating. UV radiation is the continuum and line spectrum between roughly 1000 Å and 3500 Å. This spectral region contributes to photo-dissociation, absorption, and scattering processes in the mesosphere, stratosphere, and troposphere. The spectral range from 10-1750 Å is absorbed in the lower thermosphere and effects the production of oxygen atoms and their vertical distribution above the mesopause. The Lyman-alpha line at 1216 Å plays a major role in the mesosphere through the disassociation of O_2, H_2O, and CO_2 and the ionization of nitric oxide. The spectral region between 1750 to 2400 Å leads to the dissociation of O_2 and to ozone production in the mesosphere and stratosphere. Between 2400 Å and 3300 Å, the solar irradiance is responsible for the disassociation of ozone and other trace gases that play a role in the stratospheric budget.

UV, EUV, and X-ray radiation are not only important to atmospheric and ionospheric dynamics but, through material surface changes and photoelectron emission, are a major environmental factor in space system design at all altitudes. The energy in this spectral range is represented by a solar flux between 10^7 and 10^{10} photons/cm^2-s below 1000 Å. The flux rises almost exponentially to 10^{16} photons/cm^2-s between 1000 Å and 10000 Å. The flux is not constant but varies in time due to a number of factors, one of which is the solar cycle variability. This radiation spectrum is also a complex variable of the atmospheric attenuation as a spacecraft moves in and out of the Earth's shadow [18].

Table 2. Mean Solar Particle Event Compositions for High Z Ions [3].

Element	Mean case	Element	Mean case	Element	Mean case
Cu	2.0×10^{-8}	Sn	2.0×10^{-10}	Lu	2.0×10^{-12}
Zn	6.0×10^{-8}	Sb	1.4×10^{-11}	Hf	8.0×10^{-12}
Ga	2.0×10^{-9}	Te	3.0×10^{-10}	Ta	9.0×10^{-13}
Ge	5.0×10^{-9}	I	6.0×10^{-11}	W	1.0×10^{-11}
As	3.0×10^{-10}	Xe	2.7×10^{-10}	Re	2.0×10^{-12}
Se	3.0×10^{-9}	Cs	2.0×10^{-11}	Os	3.0×10^{-11}
Br	4.0×10^{-10}	Ba	2.0×10^{-10}	Ir	3.0×10^{-11}
Kr	2.0×10^{-9}	La	2.0×10^{-11}	Pt	6.0×10^{-11}
Rb	3.0×10^{-10}	Ce	5.0×10^{-11}	Au	1.0×10^{-11}
Sr	1.0×10^{-9}	Pr	8.0×10^{-12}	Hg	1.0×10^{-11}
Y	2.0×10^{-10}	Nd	4.0×10^{-11}	Tl	9.0×10^{-12}
Zr	5.0×10^{-10}	Pm	0	Pb	1.0×10^{-10}
Nb	4.0×10^{-11}	Sm	1.0×10^{-11}	Bi	6.0×10^{-12}
Mo	2.0×10^{-10}	Eu	4.0×10^{-12}	Po	0
Tc	0	Gd	2.0×10^{-11}	At	0
Ru	9.0×10^{-11}	Tb	3.0×10^{-12}	Rn	0
Rh	2.0×10^{-11}	Dy	2.0×10^{-11}	Fr	0
Pd	6.0×10^{-11}	Ho	4.0×10^{-12}	Ac	0
Ag	2.0×10^{-11}	Er	1.0×10^{-11}	Th	2.0×10^{-12}
Cd	7.0×10^{-11}	Tm	2.0×10^{-12}	Pa	0
In	9.0×10^{-12}	Yb	9.0×10^{-12}	U	1.2×10^{-12}

Other forms of electromagnetic waves considered of importance to radiation analysis are γ-rays, Cerenkov radiation, and Bremsstrahlung radiation. Whereas X-rays are typically photons produced by inner electron shell transitions, γ-rays are photons normally associated with nuclear transitions. As such, although the higher energy X-rays overlap with the lower energy γ-rays, the latter usually represent wavelengths shorter than 0.1 Å and frequencies above 10^{20} Hz. Electromagnetic radiation emitted when a charged particle is accelerated by the coulomb field of a nucleus, usually X- or γ-rays from relativistic electrons decelerating in a solid, is called Bremsstrahlung (or "stopping") radiation. This radiation is important as it is responsible for the radiation level below which it is impractical to shield a spacecraft (usually around 3 g/cm^2). The final form of electromagnetic radiation is Cerenkov radiation. It is the ultraviolet and visible light emitted when a charged particle passes through a transparent dielectric medium with a relative speed exceeding the phase velocity of light in the medium.

2.2.2 X-Ray Flares

A primary source of naturally occurring X-rays are the so-called solar X-ray flares. An X-ray flare is associated with the sudden, short-lived brightening of a localized region in the solar chromosphere. X-ray flares nearly always occur in the plage of an active region, and are usually only visible in monochromatic light. They are classified according to their area (0,1,2,3,4) and their visible brightness (F,N,B), and/or by their X ray intensity (C,M,X). The X-ray classification levels are, in terms of the peak X-ray emission in the 1-8 Å band:

1) C event: The peak emission is between 1.0 and 9.9 x 10^{-3} ergs/cm^2-s. The actual level is given by the designator (i.e., C5.3 means the peak emission was 5.3 x10^{-3} ergs/cm^2-s). This is the least energetic solar X-ray flare level.

2) M event: The M event is a moderate level solar event and is characterized by an X-ray burst peak emission level between 1.0 and 9.9 x 10^{-2} ergs/cm^2-s (M6.6 means 6.6 x 10^{-2} ergs/cm^2-s).

3) X event: This is a major solar flare as defined by the X-ray burst level. The peak X-ray emission must be in excess of 0.1 ergs/cm^2-s (as before, X3.5 means the peak emission was 3.5 x10^{-1} ergs/cm^2-s).

A "typical" X-ray flare is plotted in Fig. 15 [19]. The data are from the November 26, 1982 X-class flare. Note the nearly exponential decay of the X-ray levels following the initial sharp rise.

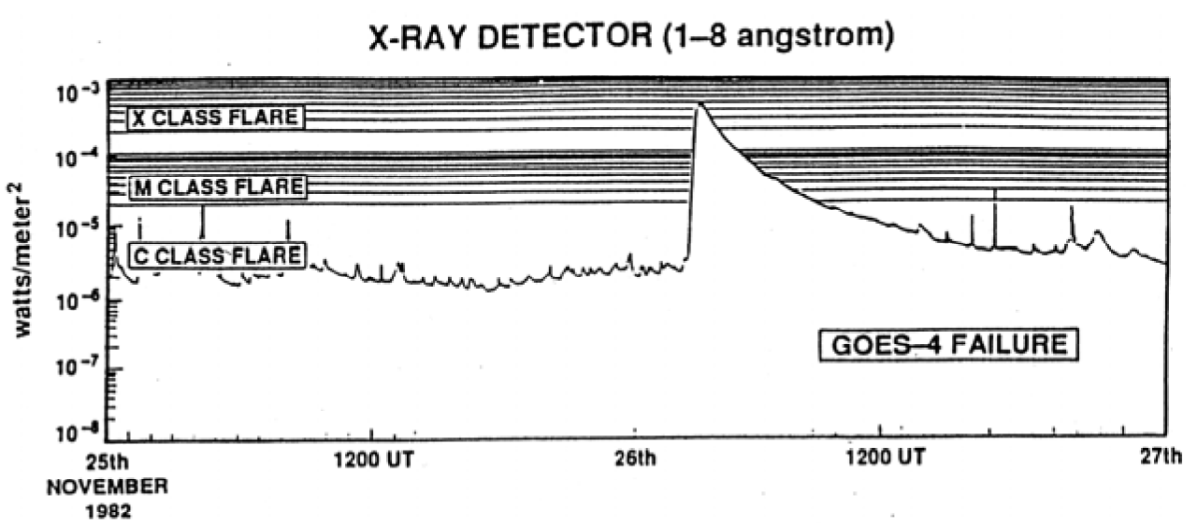

Figure 15. X-ray flux (watts/m^2) between 1 and 8 Å versus time for the November 26, 1982 solar flare as measured by the NOAA GOES spacecraft at geosynchronous orbit [19]. Also shown are the various classes of X-ray flares.

2.2.3 Interplanetary e^- and H^+

Although the interplanetary proton and electron environments are of little impact on the radiation environment, they are included here for completeness. The models for interplanetary electrons and protons are taken from NASA SP-8118 [20]. These particles fall in the energy interval between the very low energy solar wind and the energetic solar protons (approximately 1 keV and 10 MeV). NASA SP-8118 gives the integral intensities (in units of $m^{-2} s^{-1} sr^{-1}$) for these particles in terms of the following functions:

For intermediate energy protons:

$$I_{ave} = \frac{1.0 \times 10^6}{r^2 E^{1.7}} \qquad 10^{-3} < E < 10 \text{ MeV} \tag{13}$$

For intermediate energy electrons:

$$I_{ave} = \frac{400}{r^2 E^2} \qquad 2\text{x}10^{-5} < E < 10 \text{ MeV} \tag{14}$$

where E is in MeV, r in AU, and the fluence $= \iint I \, d\Omega \, dt$. The dose due to these particles is much smaller than that due to the typical solar flare environment and is thus ignored in most radiation calculations.

2.2.4 Trapped Radiation

First discovered by J. Van Allen and his collaborators on Explorer I, trapped radiation at the Earth consists principally of energetic protons and electrons, with lesser percentages of heavy ions such as O^+, contained in toroidal belts by the Earth's magnetic field. This toroid is commonly known as the "Van Allen belt(s)" [21] and consists of (at least) two zones: a low altitude zone, or "inner belt"; and a high altitude zone, or "outer belt". The inner belt extends from ~100s of km to ~ 6,000 km in altitude and is populated by high-energy (~10s of MeV) protons and high energy (1-10 MeV) electrons, while the outer belt, up to 60,000 km in altitude, is predominately high energy electrons. Schematics of the radiation flux contours for the Van Allen belts are illustrated in Fig. 16 (note the difference in scale between the electrons and protons). The detailed mechanism by which particles are entrapped in the belt regions is not well understood nor is the primary source clearly identified (as will be discussed, albedo neutrons are considered an important source of the intense proton and electron fluxes in the inner belt while

the outer belt may be primarily due to entrapment of low-energy solar wind plasma by the geomagnetic field followed by local acceleration)–observations of abundance ratios imply both terrestrial and interplanetary sources. Once captured, the motion of charged particles in the Earth's magnetic field is governed by the Lorentz force (see later). The trapped radiation environment also exhibits large temporal variations. The inner belt zone, because of the dominance of the Earth's main field, is relatively stable. Most temporal variations in this population occur as the solar cycle proceeds and the Earth's neutral atmospheric density at a given altitude changes causing variations in the altitude at which radiation particles can mirror without being scattered. In contrast, the outer belt, which is more influenced by the Earth's highly variable geomagnetic tail, experiences much greater temporal fluctuations. The electron concentration in the outer zone may experience temporal fluctuations as large as a factor of 1000. Fortunately, most of the physical damage caused by the trapped radiation is largely attributable to the long-term cumulative (or integral) dose received by the spacecraft rather than the instantaneous fluctuations of the radiation.

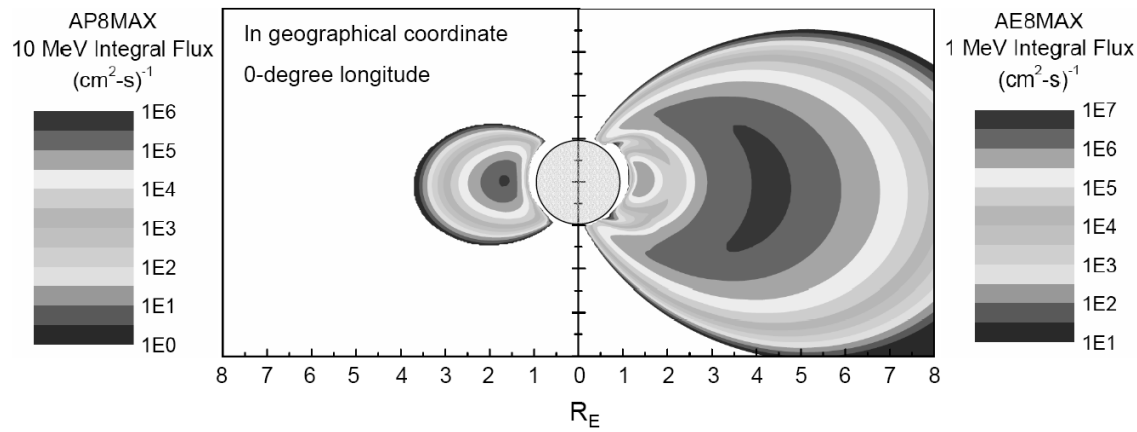

Figure 16. The Earth's radiation belts in idealized dipole space, according to the AP8 and AE8 models. Average omnidirectional integral fluxes for 1 MeV electrons and 10 MeV protons energy thresholds are shown.

In this section, to better understand the preceding description, we first discuss the primary characteristics of the Earth's magnetic field as this is the dominant force controlling the formation and changes associated with these trapped radiation belts. Following this discussion, a brief review of the basic concepts of particle entrapment such as gyro radius, mirror point, and pitch angle will be presented. Although the details of these concepts are not critical to an understanding of the basic effects of radiation on spacecraft, they are critical to understanding how the radiation belts are modeled and how one goes about determining the external dose on a particular vehicle. In particular, the concept of adiabatic invariants will be summarized–this concept is critical to an understanding of why we use B-L coordinates, the basis of almost all

modern radiation models, in describing the radiation belts. Following these descriptions, several examples of the trapped radiation environment will be presented in terms of the AE8/AP8 radiation models and the predictions compared with actual data. As will become evident, given the rapid temporal variations observed in the space environment, models are only reliable in a long term predictive sense–this is a crucial issue in establishing design margins for spacecraft.

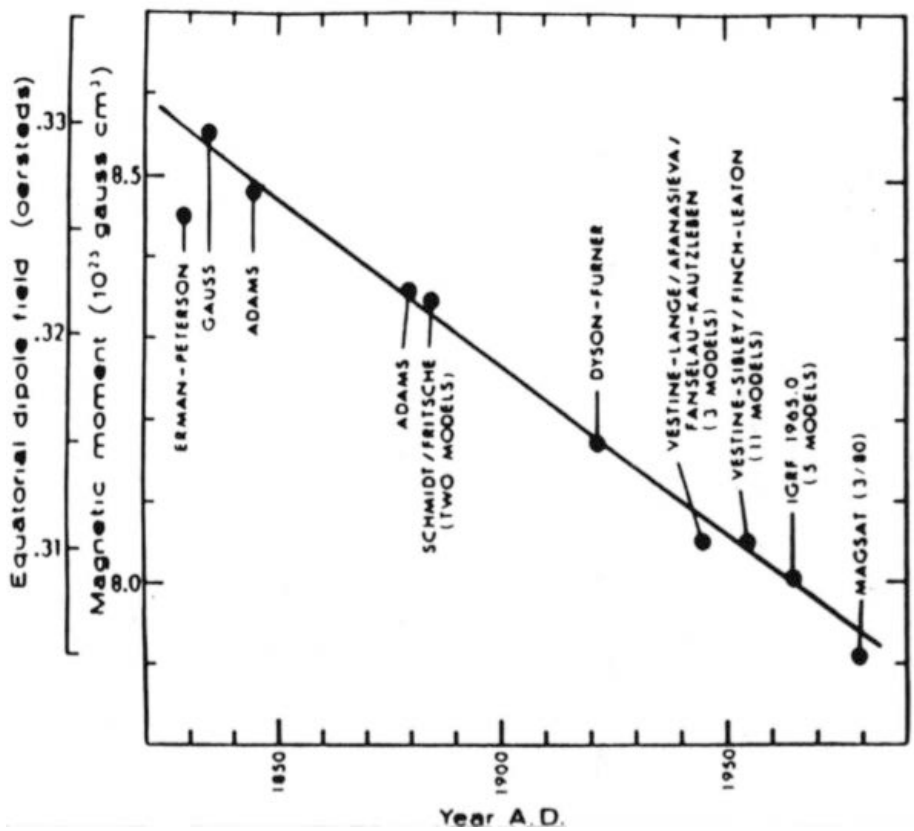

Figure 17. Decay of the Equatorial Dipole Field Strength with Time [22].

2.2.4.1 Geomagnetic Field

Above 1000 km, the dominant geophysical environment of interest is the magnetic field of the Earth–the source of the Earth's magnetosphere. Below 1000 km, the Earth's magnetic field, primarily through the control of the ionospheric plasma, plays an important though reduced role in the dynamics of the natural environment. The Earth's geomagnetic field, B, is composed of three distinct components (or current systems): the "core" field, the "crustal" field, and the "external" field [22]. The core field is a steady field due primarily to the convective motion of the conducting fluid in the Earth's internal core. The distribution of the crustal field, which is the remnant or induced magnetization of ferromagnetic materials near the Earth's surface, results in surface magnetic anomalies associated with the geologic and tectonic features of the crust. The core and crustal fields are usually combined and referred to as the "internal" or "main" field, B_i.

B_i varies slowly on the order of a hundred years--currently ~0.05% per year--as illustrated in Fig. 17 [22] (be aware that while it is critical to use a magnetic field model appropriate for the year that the magnetic field estimates are required, it is typical in radiation modeling to use the magnetic field model for the year that the radiation belt model was derived–this has caused serious problems in the past). B_i dominates at LEO and accounts for more than ~99% of B even during extremely large geomagnetic storms (massive variations in the Earth's magnetosphere brought about by changes in the solar environment that encompasses the Earth's magnetic field). In contrast, the external field, B_e, which makes up ~1% of the field at LEO, is due primarily to extra-terrestrial sources--primarily the Earth's ring current and the solar wind. It varies rapidly in time (from on the order of milliseconds to periods as long as the 11 year solar cycle) and is closely correlated with geomagnetic activity and solar interactions. Models of the external component of the geomagnetic field are available but are of limited importance to the trapped radiation belts [23-25].

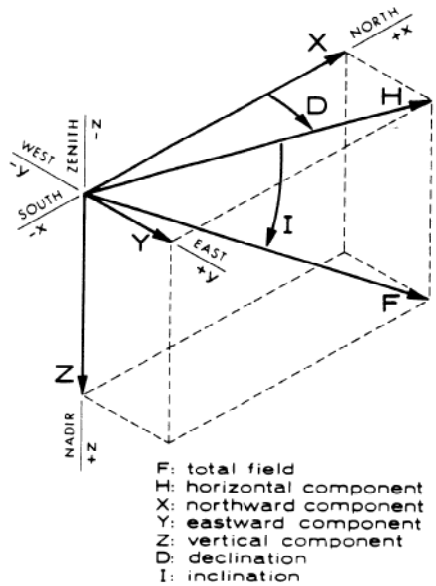

Figure 18. Geomagnetic Field Magnetic Elements [22].

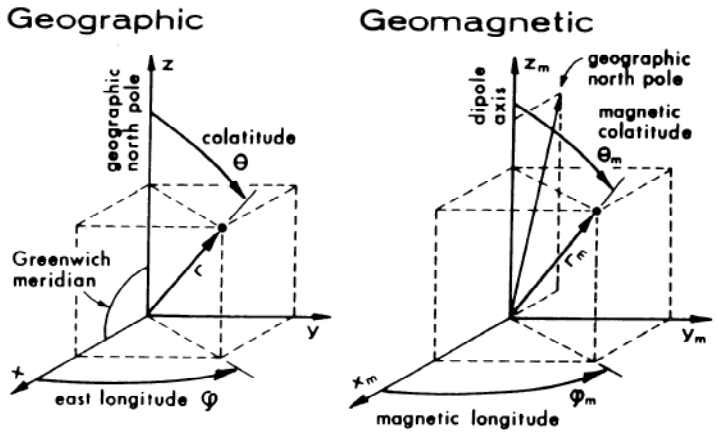

Figure 19. Spherical Coordinate System for Geographic and Geomagnetic Coordinates [22].

Seven basic quantities, called "magnetic elements", are used to specify the geomagnetic field [22]. Their definitions and relations are given in Fig. 18. Three independent quantities (e.g., (H, D, Z) or (X, Y, Z)) are required to uniquely define B. For spacecraft operating in the radiation belts, the most convenient system to use is either the geographic (also known as geocentric) or the geomagnetic coordinate system. These systems, based on spherical coordinates, are schematically defined in Fig. 19. Geographic coordinates correspond to a geocentric longitude/latitude system based on the Greenwich Prime Meridian. Geomagnetic coordinates are similarly Earth centered, but have the north pole of the system passing near the geomagnetic pole, which is offset from the geographic pole, at ~78.5° latitude and ~291.1° E. Geomagnetic longitude is measured from the great circle passing through the geographic and geomagnetic poles. Details about other coordinate systems can be found in Knecht and Shuman [22].

Aside from the gravitational field of the Earth, the magnetic field due to the internal geomagnetic field is the most accurately known of the natural environments. It can be crudely modeled in terms of a tilted (-11° from geographic north) magnetic dipole of magnitude $M = 8 \times 10^{25}$ G-cm^3 (G is the magnetic unit Gauss). Ignoring the tilt for the moment, in the geomagnetic coordinate system, the magnetic field intensity induced by M at the point (r, θ, ϕ) is given by the expression:

$$B_i = -(M / r^3) \cdot (3\cos(\theta) + 1)^{0.5} \tag{15}$$

In the Gaussian unit system, r is in cm, and B_i is in G. Given the above value for *M*, B_i is then found to have a maximum value of ~0.6 G near the polar cap and a minimum value of ~0.3 G near the equator at the Earth's surface.

Eq. 18 is valid only for an idealized configuration of a centered dipole. In reality, large scale discrepancies (as high as $\pm 25\%$) exist between the measured data and the ideal, dipole expression. Modifying the configuration from a centered dipole to an eccentric dipole reduces the discrepancies to the ~10% level, but this is still unacceptably large. For most purposes, the IGRF series of models is the official standard. The latest version of the International Geomagnetic Reference Field, IGRF-2010, is a computer model based on numerical fitting of measured data with a magnetic scalar potential expanded in terms of spherical harmonics [26, 27]. The model calculates the seven magnetic elements of B_i for any given geographical location. Specifically, a scalar "potential" is found such that:

$$V(r,\theta,\phi) = a\sum_{n=1}^{N}\sum_{m=0}^{n}\left\{\left[A_{n,m}\cos m\phi + B_{n,m}\sin m\phi\right]\left(\frac{a}{r}\right)^{n+1} + \left[C_{n,m}\cos m\phi + D_{n,m}\sin m\phi\right]\left(\frac{r}{a}\right)^{n}\right\}P_{n,m}(\cos\theta) \tag{16}$$

where:

a = radius of Earth

r = radial distance in units of a

N = order of expansion

θ = colatitude

ϕ = east longitude

$A_{n,m}$, $B_{n,m}$ = constants for internal terms

$C_{n,m}$, $D_{n,m}$ = constants for external terms

The magnetic field components are then given by:

$$B_r = \frac{\partial V}{\partial r}$$

$$B_\theta = -\frac{1}{r}\frac{\partial V}{\partial \theta} \tag{17}$$

$$B_\phi = -\frac{1}{r\sin\theta}\frac{\partial V}{\partial \phi}$$

Values of A, B, C, and D are presented in Table 3 for the IGRF 2010 model. As discussed earlier, the epoch of the magnetic model is important and should correspond either to the same date as the date of the radiation model (~1970 for AE8/AP9) used or to a model epoch as close to the present as possible if only the current magnetic field value is desired (i.e., IGRF 2010 plus the dB/dt correction for 2011).

Figs. 20a and 20b show the 3 dimensional character of the Earth's magnetic field. Fig. 20a is a cross section of the Earth's magnetic field in the noon-midnight meridian showing the structure of the field lines and the plasma regions they contain. Fig. 20b illustrates typical results from calculations of the magnetic field amplitude over the northern hemisphere at a constant altitude of 400 km. The field amplitude varies from a minimum of 0.25 G near the equator to 0.5 G over the polar caps. Two peaks exist in the magnitude of the magnetic field over the north pole (if vector components are considered, the maximum at 270° east longitude is the true "dip" magnetic pole). Likewise, there are two minima near the equator--the largest of these is responsible for the so-called South Atlantic Anomaly, a region critical in determining radiation exposure in LEO. Finally, it should be noted that geomagnetic storm variations are superimposed on this main field. These are typically less that 0.01 G so that even during a severe geomagnetic storm, magnetic fluctuations are small at low altitudes compared to the average field (even though this is a very small change in the Earth's field, the effect of geomagnetic storms on particle fluxes in the polar ionosphere can be tremendous). They are critical, however, at geosynchronous orbit where the main magnetic field is of comparable strength and dominate the magnetic field at higher altitudes.

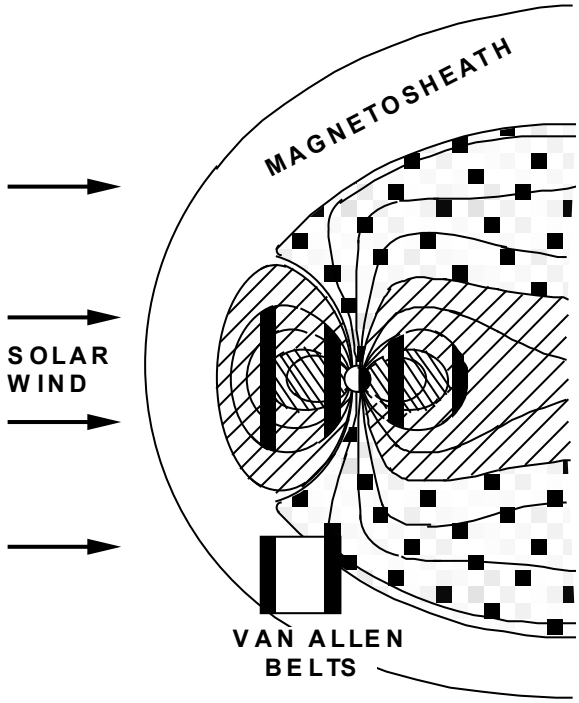

(A)

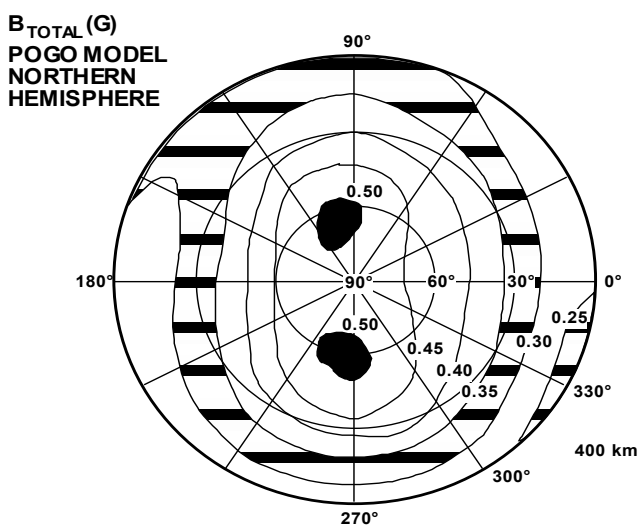

(B)

Figure 20. A) Cross section of the Earth's magnetic field in the noon-midnight meridian showing the structure of the field lines and the plasma regions they contain. B) Illustration of the magnetic field amplitude over the northern hemisphere at a constant altitude of 400 km. The field amplitude varies from a minimum of 0.25 G near the equator to 0.5 G over the polar caps.

Table 3. Spherical-Harmonic Coefficients for the IGRF 2010 [27].
Units are nT and nT/yr.

cos/sin g/h	degree n	order m	IGRF 2010	dB/dt 2010-15
g	1	0	-29496.5	11.4
g	1	1	-1585.9	16.7
h	1	1	4945.1	-28.8
g	2	0	-2396.6	-11.3
g	2	1	3026.0	-3.9
h	2	1	-2707.7	-23.0
g	2	2	1668.6	2.7
h	2	2	-575.4	-12.9
g	3	0	1339.7	1.3
g	3	1	-2326.3	-3.9
h	3	1	-160.5	8.6
g	3	2	1231.7	-2.9
h	3	2	251.7	-2.9
g	3	3	634.2	-8.1
h	3	3	-536.8	-2.1
g	4	0	912.6	-1.4
g	4	1	809.0	2.0
h	4	1	286.4	0.4
g	4	2	166.6	-8.9
h	4	2	-211.2	3.2
g	4	3	-357.1	4.4
h	4	3	164.4	3.6
g	4	4	89.7	-2.3
h	4	4	-309.2	-0.8
g	5	0	-231.1	-0.5
g	5	1	357.2	0.5
h	5	1	44.7	0.5
g	5	2	200.3	-1.5
h	5	2	188.9	1.5
g	5	3	-141.2	-0.7
h	5	3	-118.1	0.9
g	5	4	-163.1	1.3
h	5	4	0.1	3.7
g	5	5	-7.7	1.4
h	5	5	100.9	-0.6
g	6	0	72.8	-0.3
g	6	1	68.6	-0.3
h	6	1	-20.8	-0.1
g	6	2	76.0	-0.3
h	6	2	44.2	-2.1
g	6	3	-141.4	1.9
h	6	3	61.5	-0.4
g	6	4	-22.9	-1.6
h	6	4	-66.3	-0.5
g	6	5	13.1	-0.2
h	6	5	3.1	0.8
g	6	6	-77.9	1.8
h	6	6	54.9	0.5
g	7	0	80.4	0.2
g	7	1	-75.0	-0.1
h	7	1	-57.8	0.6
g	7	2	-4.7	-0.6
h	7	2	-21.2	0.3
g	7	3	45.3	1.4
h	7	3	6.6	-0.2
g	7	4	14.0	0.3
h	7	4	24.9	-0.1
g	7	5	10.4	0.1
h	7	5	7.0	-0.8
g	7	6	1.6	-0.8
h	7	6	-27.7	-0.3
g	7	7	4.9	0.4
h	7	7	-3.4	0.2
g	8	0	24.3	-0.1
g	8	1	8.2	0.1
h	8	1	10.9	0.0
g	8	2	-14.5	-0.5
h	8	2	-20.0	0.2
g	8	3	-5.7	0.3
h	8	3	11.9	0.5
g	8	4	-19.3	-0.3
h	8	4	-17.4	0.4
g	8	5	11.6	0.3
h	8	5	16.7	0.1
g	8	6	10.9	0.2
h	8	6	7.1	-0.1
g	8	7	-14.1	-0.5
h	8	7	-10.8	0.4
g	8	8	-3.7	0.2
h	8	8	1.7	0.4
g	9	0	5.4	0.0
g	9	1	9.4	0.0
h	9	1	-20.5	0.0
g	9	2	3.4	0.0
h	9	2	11.6	0.0
g	9	3	-5.3	0.0
h	9	3	12.8	0.0
g	9	4	3.1	0.0
h	9	4	-7.2	0.0
g	9	5	-12.4	0.0
h	9	5	-7.4	0.0
g	9	6	-0.8	0.0
h	9	6	8.0	0.0
g	9	7	8.4	0.0
h	9	7	2.2	0.0
g	9	8	-8.4	0.0
h	9	8	-6.1	0.0
g	9	9	-10.1	0.0
h	9	9	7.0	0.0
g	10	0	-2.0	0.0
g	10	1	-6.3	0.0
h	10	1	2.8	0.0
g	10	2	0.9	0.0
h	10	2	-0.1	0.0
g	10	3	-1.1	0.0
h	10	3	4.7	0.0
g	10	4	-0.2	0.0
h	10	4	4.4	0.0
g	10	5	2.5	0.0
h	10	5	-7.2	0.0
g	10	6	-0.3	0.0
h	10	6	-1.0	0.0
g	10	7	2.2	0.0
h	10	7	-4.0	0.0
g	10	8	3.1	0.0
h	10	8	-2.0	0.0
g	10	9	-1.0	0.0
h	10	9	-2.0	0.0
g	10	10	-2.8	0.0
h	10	10	-8.3	0.0
g	11	0	3.0	0.0
g	11	1	-1.5	0.0
h	11	1	0.1	0.0
g	11	2	-2.1	0.0
h	11	2	1.7	0.0
g	11	3	1.6	0.0
h	11	3	-0.6	0.0
g	11	4	-0.5	0.0
h	11	4	-1.8	0.0
g	11	5	0.5	0.0
h	11	5	0.9	0.0
g	11	6	-0.8	0.0
h	11	6	-0.4	0.0
g	11	7	0.4	0.0
h	11	7	-2.5	0.0
g	11	8	1.8	0.0
h	11	8	-1.3	0.0
g	11	9	0.2	0.0
h	11	9	-2.1	0.0
g	11	10	0.8	0.0
h	11	10	-1.9	0.0
g	11	11	3.8	0.0
h	11	11	-1.8	0.0
g	12	0	-2.1	0.0
g	12	1	-0.2	0.0
h	12	1	-0.8	0.0
g	12	2	0.3	0.0
h	12	2	0.3	0.0
g	12	3	1.0	0.0
h	12	3	2.2	0.0
g	12	4	-0.7	0.0
h	12	4	-2.5	0.0
g	12	5	0.9	0.0
h	12	5	0.5	0.0
g	12	6	-0.1	0.0
h	12	6	0.6	0.0
g	12	7	0.5	0.0
h	12	7	0.0	0.0
g	12	8	-0.4	0.0
h	12	8	0.1	0.0
g	12	9	-0.4	0.0
h	12	9	0.3	0.0
g	12	10	0.2	0.0
h	12	10	-0.9	0.0
g	12	11	-0.8	0.0
h	12	11	-0.2	0.0
g	12	12	0.0	0.0
h	12	12	0.8	0.0
g	13	0	-0.2	0.0
g	13	1	-0.9	0.0
h	13	1	-0.8	0.0
g	13	2	0.3	0.0
h	13	2	0.3	0.0
g	13	3	0.4	0.0
h	13	3	1.7	0.0
g	13	4	-0.4	0.0
h	13	4	-0.6	0.0
g	13	5	1.1	0.0
h	13	5	-1.2	0.0
g	13	6	-0.3	0.0
h	13	6	-0.1	0.0
g	13	7	0.8	0.0
h	13	7	0.5	0.0
g	13	8	-0.2	0.0
h	13	8	0.1	0.0
g	13	9	0.4	0.0
h	13	9	0.5	0.0
g	13	10	0.0	0.0
h	13	10	0.4	0.0
g	13	11	0.4	0.0
h	13	11	-0.2	0.0
g	13	12	-0.3	0.0
h	13	12	-0.5	0.0
g	13	13	-0.3	0.0
h	13	13	-0.8	0.0

2.2.4.2 Magnetic and Electric Field Effects

A major radiation environment of concern is that associated with the trapped radiation belts around the planets. To understand the trapped radiation environment, one must first understand how charged particles move in the Earth's magnetic field. This section provides a very brief overview of the fundamentals of charged particle motion so that the concepts used in modeling the radiation belts can be comprehended. The reader is referred to many excellent texts in this area such as the classic book by Roederer [2] or, more recently, Walt [28].

2.2.4.2.1 Basic Particle Motion

To understand how charged particles become "trapped", it is necessary to review the forces that act on those particles. Except near the upper fringes of the Earth's atmosphere (<100-150 km), collisional and frictional forces on charged particles can, in general, be ignored. The two main forces (F_E and F_M) are then (units of cm-g-s or CGS are used unless otherwise noted) the electrostatic force:

$$F_E = qE \tag{18}$$

and the magnetic (Lorentz) force:

$$F_M = \frac{q}{c} V \times B \tag{19}$$

where q is the particle charge (including sign), c is the speed of light, V the velocity vector of the particle, B the magnetic field vector in space, and E the electric field vector in space.

Consider the actual motion of a particle subject to equations (18) and (19). Setting the electric field to zero and using the definition of the cross product, equation (19) implies that the force on a charged particle is always perpendicular to both the particle's instantaneous velocity vector and the magnetic field vector. This means that a particle must, in the absence of another force and in the presence of a uniform magnetic field, move in a circle in the plane perpendicular to the magnetic field vector. It may additionally move freely (without any acceleration) along the magnetic field, mapping out a helix around its "center of motion" (Figs. 21, 22, and 23). The radius R_c (called the cyclotron or gyro radius) of this circle is found by equating the centripetal force, mV^2/R, to the Lorentz force. In this expression m is the particle mass and $V_\perp$ is the component of the velocity perpendicular to B. The expression is:

$$R_c = \frac{mV_\perp c}{qB} \tag{20}$$

The frequency with which the charged particle gyrates, the cyclotron frequency, ω_c, is given by:

$$\omega_c = \frac{qB}{mc} \tag{21}$$

where ω_c is in radians per second.

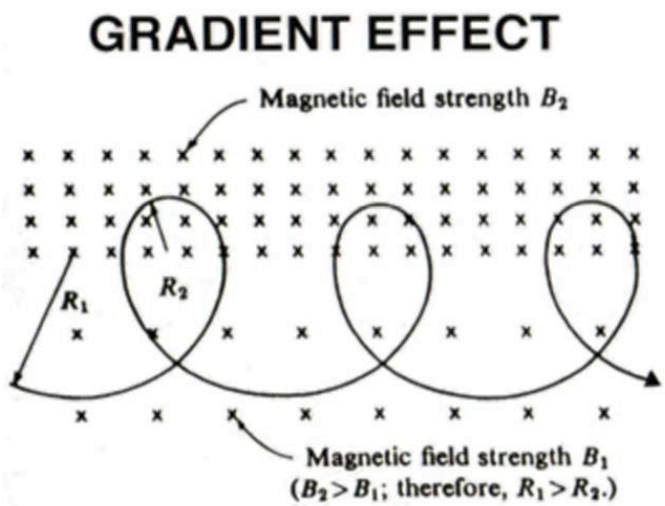

Figure 21. Motion of a charged particle (positive in this case) in a magnetic field in the absence of an electric field. The magnetic field is constant in the lower half of the figure and equal to B_1. It is constant and equal to B_2 in the upper part of the figure. The figure illustrates the effects of a gradient in a direction perpendicular to the direction of the magnetic field.

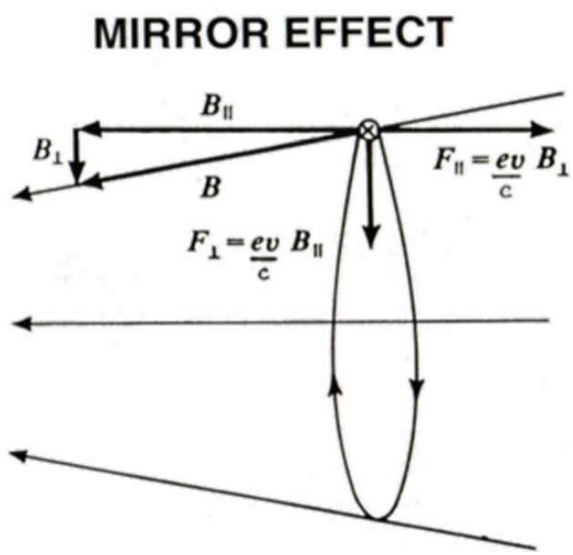

Figure 22. Motion of a charged particle in a converging magnetic field in the absence of an electric field. $F_{\perp}$ is the force along the magnetic field that results from the field convergence (or divergence) and is responsible for the mirroring effect (see text).

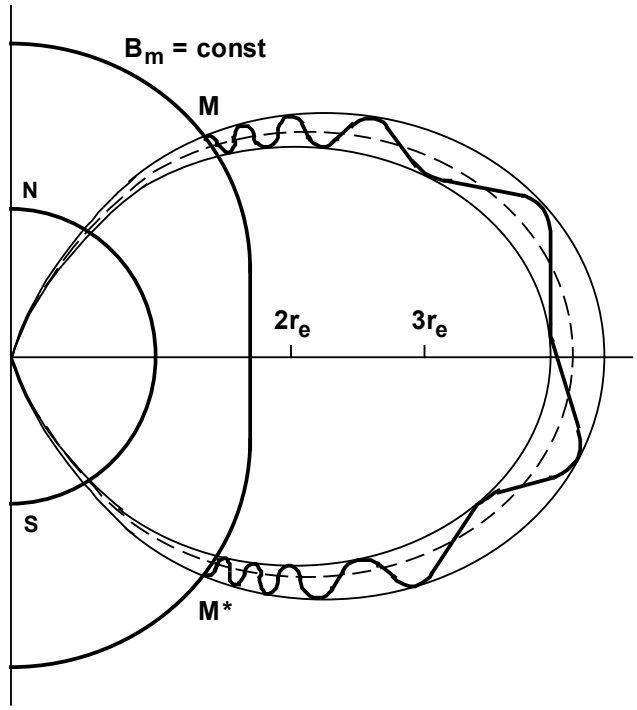

Figure 23. Motion of a Charged Particle in a Dipole Magnetic Field.

According to equation (19), any particle motion parallel to B is unaffected by B. The particle's motion can be described in terms of a velocity parallel to the field, $V_{||}$, or perpendicular to the field, $V_{\perp}$, and a quantity called the particle pitch angle, "α", the angle the particle motion makes relative to the B direction:

$$\alpha = \sin^{-1}(V_{\perp}/V) \tag{22}$$

$$\alpha = \cos^{-1}(V_{\parallel}/V)$$

The motion of the particle can be pictured as spiraling along the magnetic field direction, executing cyclotron motion around the field while moving along the field (Fig. 23). A charged particle will deviate from these simple motions if there is an electric field or if the magnetic field has temporal changes. As an example, consider the case where the magnetic field increases with distance in a direction perpendicular to the direction of B. In this case as the particle moves from the region of low field strength to high field strength and back again, R_c decreases and increases correspondingly, and the particle traces out a cycloid configuration (Fig. 21). Under the combined influence of both the Earth's electric field (this field is radially directed close to the Earth and points from dawn to dusk at greater distances) and the radial gradient of its magnetic field, charged particles will slowly trace a similar cycloid around the Earth (electrons drifting towards the east and high energy ions towards the west). Although such motion is quite

complex, if the magnetic field gradient or E are sufficiently weak, the motion of the particle can be described in terms of its cyclotron motion and a constant "drift velocity".

The final type of motion of interest here results from gradients along the magnetic field and is responsible for the "trapping" of radiation particles in the magnetic field. If the magnetic field converges, then the particle will feel a small force along the direction of the field line. This will cause the particle to decelerate (accelerate) as it moves into the converging (diverging) region (Fig. 22). Eventually (unless the particle has collisions with atmospheric particles–i.e., the mirror point is below some critical altitude which we will define by the magnetic field strength at that position, B_c), the particle will have its motion parallel to the field stopped. However, due to the particle's circular motion (perpendicular to the field), it still experiences the decelerating force which reflects the particle back along the field line. This occurs at the "mirror" point, as determined by the strength of the magnetic field. This point is designated by "B_m" (Fig. 23). As will become evident, B_m and B_c are critical in determining charged particle motions.

2.2.4.2.2 Invariants of the Particle Motion

The many different types of motion of a particle in combined E and B fields initially appear to be very difficult to handle. In fact, if the E and B fields are changing rapidly in time and space in comparison to the characteristic motions of the particle, then careful, single particle trajectories must be calculated for each and every particle. Fortunately, the Earth's E and B field generally change very slowly in time and space compared to the characteristic motions of radiation particles. We can then describe the particles' group motions in terms of so-called characteristic invariants of the motion (realizing that they do indeed change slightly) rather than having to calculate each particle trajectory. The adiabatic invariants help determine the scale over which the approximations hold. This section will describe those characteristic constants. First, consider the cyclotron motion of a particle. The motion of a particle in a slowly varying B and E field can be described as a cyclotron motion superimposed on a slow drift of the particle's guiding center, the center of the cyclotron gyration. The energy and angular momentum of a charged particle will remain constant during this motion if the adiabatic invariants are conserved. A particle which mirrors at a field strength of B_m has a pitch angle at an arbitrary B ($B_m \geq B$) given by:

$$\sin^2(\alpha) = \frac{B}{B_m} \tag{23}$$

This may also be expressed in the form of the first adiabatic invariant:

$$\mu = \frac{m V_{\perp}^{2}}{2B} = \text{constant} \tag{24}$$

μ is also called the magnetic moment invariant because it is the magnetic moment of the charged particle (μ = IA, where I is the current and A is the area of the "loop"). If the magnetic field changes slowly, the magnetic moment is conserved and the ratio of the particle energy perpendicular to the field will stay constant relative to the magnetic field strength.

The second invariant is called the longitudinal invariant. Before discussing it, consider the dipole magnetic field of the Earth. This field can be crudely represented by a tilted dipole with components:

$$B(r) = \frac{-2M \sin(\lambda)}{r^3} \tag{25}$$

$$B(\lambda) = \frac{M \cos(\lambda)}{r^3} \tag{26}$$

$$B(\phi) = 0 \tag{27}$$

where M = 0.311 G-R_e^3, R_e is the Earth's radius (1 R_e = 6371 km), and r is the radial distance from the center of the Earth; B(r), B(λ), and B(ϕ) are the field components in polar coordinates. For reference, a field line for this dipole field is defined by:

$$r = r_o \cos^2 \lambda \tag{28}$$

$$\varphi = \varphi_o = \text{constant}$$

where r_o is the radial distance at which the field line crosses the magnetic equator and a field line is the line that would be traced by always moving in the direction of the B vector.

The dimensionless quantity L can be defined where:

$$L = \frac{r_o}{R_e} \tag{29}$$

The value of L is, by the definition of r_o, the equatorial crossing point of a magnetic field line in terms of R_e. Referring back to the discussion of the effects of a converging magnetic field, if the cyclotron radius is sufficiently smaller than the curvature of the Earth's magnetic field lines, then, to a good approximation, the case of a particle moving back and forth between two magnetic mirrors is as illustrated in Fig. 23. The particle does not move along a surface of constant B, but moves on a surface of constant L between B_m (B_m is constant by virtue of the first invariant) in the northern hemisphere and in the southern hemisphere. In fact, the second invariant Φ defined by:

$$\Phi = \int V_{\parallel} dl \tag{30}$$

is a constant of the particle motion (dl is a unit of length along the particle trajectory). Constant Φ means that as a radiation particle drifts, it traces out a cycloid around the Earth's equator and follows a well defined surface. This surface is defined by the "L shell" of the particle and the two mirror points. This fact has given rise to the use of the McIlwain B-L coordinate system in which a particle population is completely described in terms of the particle flux as a function of B and L values–this is the fundamental underpinning of most existing trapped radiation models in use today.

Particles which have B_m values that fall below about 100 km are generally lost to the atmosphere by collisions with neutral particles so that frequently when plotting particle distributions as a function of α, a gap in the flux is found near 0° and 180° (this is not always true, however; see later). This is called the particle loss-cone angle for obvious reasons.

Combining equations 25-27, it can be shown that:

$$B(\lambda)/B_o = \frac{\left(4 - 3\cos^2(\lambda)\right)^{1/2}}{\cos^6(\lambda)} \tag{31}$$

The magnetic latitude that a particle with pitch angle α_o at the magnetic equator will mirror can be determined by combining Eq. 31 with Eq. 23 to get:

$$\sin(\alpha_c) = \frac{\cos^3(\lambda)}{\left(4 - 3\cos^2(\lambda)\right)^{1/4}} \tag{32}$$

This expression can be used to determine the maximum pitch angle that a spacecraft can see at a given latitude in space. That is, if the spacecraft passes through the magnetic field line at a magnetic latitude of λ, it can only detect particles that have equatorial pitch angles of α_o or less (for 0° to 90°). All particles with initial pitch angles greater than α_o at the equator will have mirror points which lie between the spacecraft latitude and the magnetic equator and, therefore, will not be detected by the spacecraft detectors.

The third invariant of the motion, Q, is the flux invariant. This is simply the net magnetic flux inside the longitudinal-invariant surface defined by:

$$Q = \int \overline{B} \cdot d\overline{s} \tag{33}$$

where ds is an element of area. This invariant implies that the guiding center of the particle follows slow changes in the Earth's magnetic field.

The three invariants together allow the development of simple time-averaged models of the radiation particle fluxes. It should be remembered, however, that perturbing electric and magnetic fields do occasionally modify the particle motion so that the three invariants are violated. There are perturbations in the magnetosphere which occur on time scales of the cyclotron, the bounce, and the drift periods which violate the three invariants and alter the particle motion. Such variations lead to the diffusion of the particle populations (primarily the electrons) in pitch angle so that the loss cone can sometimes be filled with particles.

2.2.4.3 Electron and Proton Belts

There are potentially many different ways to model the Earth's radiation environment. Fortunately, the use of adiabatic invariants and the introduction of the McIlwain B-L coordinates have lead to a standardized means of representing the time-averaged features of the trapped radiation environment. Aside from the CRRES models (see [29]) for a comparison of the models with CRRES data), the AE/AP radiation models developed by Vette and his colleagues at NASA Goddard have been the principle source of a uniform set of practical models of the Earth's trapped radiation environment [30, 31] for decades. Here, although the soon to be released AE9/AP9 models will ultimately change the details, the major characteristics of the Earth's trapped radiation environment will be summarized in terms of these AE8/AP8 models with emphasis on the critical environmental variables. The AP8/AE8 models are based on compiled data from many different satellites [30-32]. The P and E in the model names AP8 and AE8 refer to "Proton" and "Electron" and 8 is the version number of the models. For a given set of McIlwain B-L coordinates in the range from low Earth orbit to somewhat beyond

geosynchronous, AP8 and AE8 provide estimates of the omnidirectional fluxes of protons in the energy range of ~50 keV to 500 MeV and electrons in the energy range of ~50 keV to ~7 MeV. Time-dependent variations of the radiation fluxes such as those due to geomagnetic storms or short term solar modulations are not included in AP8/AE8. However, the models do differentiate between solar cycle maximum and minimum conditions. For protons, a larger flux is predicted at solar cycle minimum than solar cycle maximum. The situation is reversed for electrons with higher fluxes at solar maximum.

It is common in modeling the radiation environment to assume an omnidirectional flux of particles, integrated over an energy interval, and given as a function of B and L coordinates. By definition, omnidirectional means that the particle flux has been averaged over all pitch angles. As discussed earlier, units are typically "particles per square centimeter per second" with the integrated energy channel being from a lower energy to the highest energies capable of being measured by space detectors. Although there are specific cases such as in shielding design for sensitive particle or light detector systems where pitch angle is important, in practice the design community that uses these codes only requires the omnidirectional flux. In principle, it is possible to construct this type of simple model by one measurement of the fluxes at all pitch angles as a satellite moves away from the Earth in the magnetic equatorial plane. The major difficulty in developing such a model of the Earth's radiation belts is that both space and time must be factored into the model. Although the use of the adiabatic invariants and B-L coordinates are very useful in simplifying this task, in reality asymmetries in the Earth's magnetic and electric fields and their time variations introduce significant complications into the modeling process. In particular, "shell-splitting" (particles of the same energy but different pitch angles tend to follow slightly different drift paths around the Earth so that particles observed together at the equator on one side of the Earth are separated in radial distance on the other side), distortions in the Earth's magnetosphere, and similar effects force the inclusion of temporal and local-time (or, less precisely, longitudinal) variables. The AE8/AP8 model fluxes, for example, are parametrically represented by:

$$I(>E,B,L,t,T) = N(>E,L)\Phi(>E,L,t)G(B,L) \tag{34}$$

Where I is the integral omnidirectional flux, >E means for all energies above E, t is the local time, and T is the epoch (or date) of the model. No one spacecraft can collect sufficient data over a long enough time interval or in enough locations to adequately define Eq. 34. Rather data from many different satellites are averaged in discrete B and L bins to determine the B-L variation G; in energy, L, and local time to determine the local time variation Φ (note: B variations were ignored because there was often too little data to allow simultaneous binning in terms of B also); and in energy and L bins to determine the energy variations N. As many

different satellites were used, it was important to know the efficiency and geometric factor for the different detectors. As discussed by Vette and his collaborators, there are many regions of spotty spatial coverage [31]. Likewise, short term temporal variations are not well represented.

Fig. 16 for 1 MeV electrons and 10 MeV protons illustrates the basic structure of the radiation belts as predicted by the AE8 and AP8 models. In particular, the electron contours show a dual peak (the protons have a similar structure but the division between the peaks is less obvious). Typically, therefore, the radiation belts, according to these models, are divided into "inner-zone" and "outer-zone" populations. This division also roughly corresponds, for the electrons, to an inner belt which is weakly affected by geomagnetic storms and an outer belt which is greatly affected by storms. The L-shell region up to L~2.5 is termed the inner-zone while the region beyond L~3 is considered to be the outer-zone with a "slot" region of reduced density in between. The inner-zone electrons peak around L = 1.45 to 1.5. Little variation with geomagnetic activity is seen below L~1.6. The inner-zone protons are very stable, varying inversely with atmospheric density (the fluxes are lower at solar maximum when the atmospheric density is highest). The proton flux peaks near L = 1.45. In the outer zone, the peak L shell varies with energy for the electrons and flux increases can be as great as 10^5 in less than a day during a geomagnetic storm. The outer-zone protons, in contrast, do not show as strong a division into an outer belt as the electrons nor as much variation with geomagnetic activity. Protons with $E \geq 1$ MeV peak at about L = 3 while protons with $E \geq 10$ MeV peak at about L = 2.5. (Note: all numbers are adapted from Vampola [33].) To summarize, the AP8/AE8 models describe the following populations:

a) The slowly varying, stably trapped high energy protons and the inner zone electrons ($\leq 3\ R_e$). (Note: the AP8MAX and AP8MIN differ only for altitudes less than about 1000 km.)

b) The trapped but highly variable outer zone electrons ($\geq 3\ R_e$)

Basic uncertainty factors have been defined for these models. These are (for 5 to 10 year averages):

AP8:	(min. and max.):	a factor of 2
AE8:	(min. and max.):	a factor of 2

Below 1000 km, the main trapped radiation environment consists of 2 components: the low altitude extension of the radiation belts (or "horns") at high latitudes and the low latitude South Atlantic (Magnetic) Anomaly. Figures 24 and 25 illustrate these regions for protons and electrons [34]. The units are particles/cm^2-s for E>30 MeV and E>0.5 MeV respectively. The lines represent isoflux contours at 296 km (Fig. 24) and 400 km (Fig. 25). It is interesting to note that the South Atlantic Anomaly, which is the result of low magnetic field intensities in the South Atlantic near Brazil (Fig. 20), is slowly drifting westward with a period of about 1200

years. High energy, trapped particles mirror at a characteristic constant magnetic field strength--thus particles that typically would mirror at higher altitudes above the atmosphere find themselves mirroring at much lower altitudes in this region thereby enhancing the background fluxes.

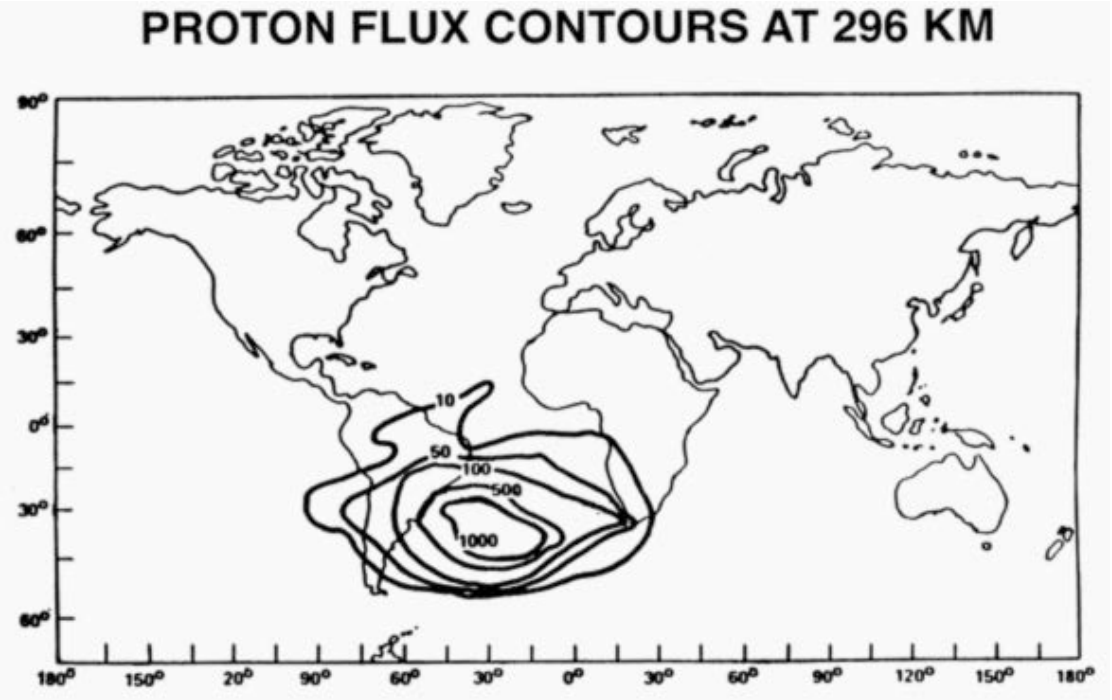

Figure 24. Proton Flux Densities at 296 km Altitude [34].

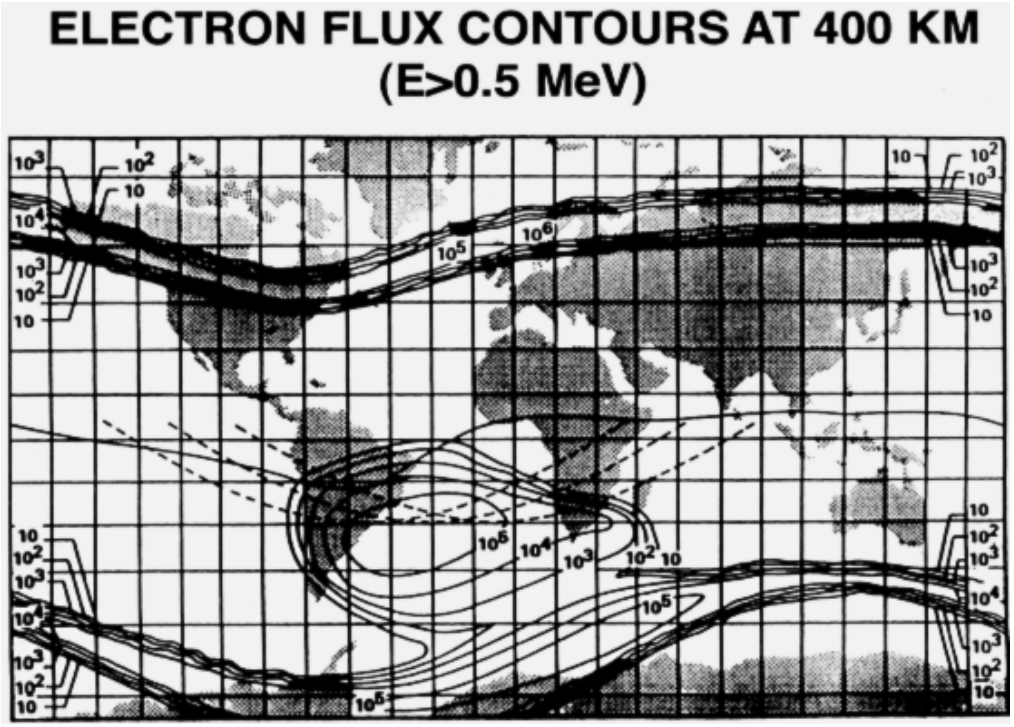

Figure 25. Electron Constant Flux Contours at 400 km Altitude. (E>0.5 MeV) [34].

2.2.4.4 Long-Term and Short-Term Variations

Here the concepts developed in the previous sections will be used to interpret the difficulties that arise in estimating the trapped radiation environment. Of principle interest will be the complications introduced by time variations in the plasma environment over the solar cycle, effects of the decay of the Starfish and Argus nuclear tests, and short term geomagnetic storm effects. These effects currently all complicate attempts to accurately characterize the radiation particle population in an "average sense".

2.2.4.5 Examples: Solar Cycle Effects, Storms, Substorms

Figure 26 illustrates approximately one year's worth of hourly averages of the 1.9 MeV omnidirectional electron flux measured at midnight by the geosynchronous satellite ATS 1 [35]. The daily sum of the geomagnetic index K_p (at the bottom of the figure) and the value predicted by the AE model (the horizontal line) are also plotted for comparison. This figure demonstrates two important points. First, the electron radiation flux at L=6.6 is highly variable on a daily time scale--some variations being on the order of 10 to 100. Secondly, the AE model is biased toward the few major geomagnetic storms. This biasing is to be expected as the model is derived by averaging the fluxes. Figure 27 demonstrates electron variations over a slightly longer time period for different L values. The data are 10 day averages of the electrons with energy greater than 0.28 MeV, taken on the 1963 38C spacecraft [36]. Inside of L=1.8 (generally referred to as the inner electron zone) the time variations are quite small, demonstrating the usefulness of an average model in this region. The steady decay of flux levels in the figure is due to the decay of the residue from the artificial Starfish injection event of July 1962. In contrast, outside L=1.8, the fluxes at L=2.2 vary greatly with time due to geomagnetic activity.

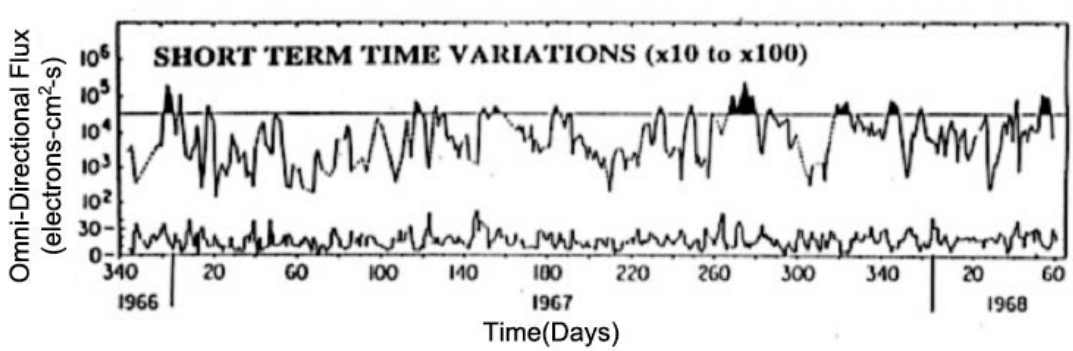

Figure 26. Hourly averages of ATS1 1.9 MeV omnidirectional electron flux at local midnight [36]. Daily sum of K_p is plotted at the bottom of the figure. The horizontal line is the AEI-7 model equatorial flux at L = 6.6 and local midnight.

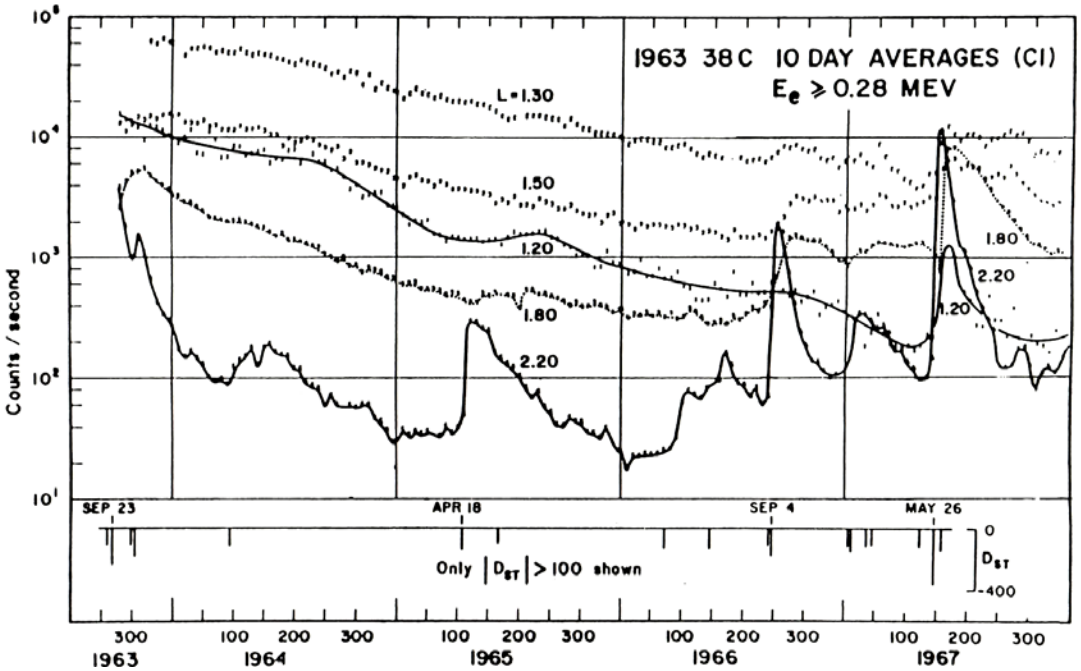

Figure 27. 10 day averages of the inner zone electron fluxes greater than 0.28 MeV (in units of count rate) measured by the satellite 1963-38C. The effects of the decay of the Starfish nuclear debris and of the 4 major geomagnetic perturbations are evident [36].

2.2.4.6 AE8/AP8 Comparisons With The Crres Models

2.2.4.6.1 Coverage Limitations

Although a given AE/AP model may be accurate for the period of time for which the measurements were taken, it does not necessarily follow that it is accurate for another epoch. That is, there are long term variations such as the decay of the Starfish nuclear explosion radiation that change over much longer time scales than data exists. The solar cycle, for example, follows an irregular 11 year pattern and the level of geomagnetic activity at one solar minimum may differ substantially from that of the next. Thus, for a model to be appropriate for a given time interval, it should ideally include observations from that interval. At the least, the data base used should be as close in time as possible if accurate predictions are to be expected. The observations for the AE8/AP8 models (and these are principally from one satellite) are over 30 years old! The CRRES spacecraft was launched in 1989 to update the models, remap the radiation belts, and to study radiation effects on microelectronics. The results of the 1 year mission of the CRRES clearly revealed problems with the AE8/AP8 models, in particular, a highly variable third belt was discovered between the main two [29]. This is illustrated in Figs. 28 and 29. Fig. 28 is a comparison of a) the AP8 and CRRES models for E>20 MeV and b) the AE8 and CRRES models for electrons with E>2.5 MeV (and protons with protons with E>135

MeV). The regions of greatest differences are indicated by the boxes. Note that the AE8/AP8 models are roughly comparable to the CRRES "active" models except for the trough region which disappears in the CRRES data. This behavior is even more apparent in Fig. 29. These are meridional plots of CRRES data for a) protons with E>35 MeV and b) electrons with E> 1 MeV. The upper plots are for "quiet" conditions and the lower for "active" conditions for electrons with E>1 MeV. This third belt represents an important variable feature that needs to be modeled.

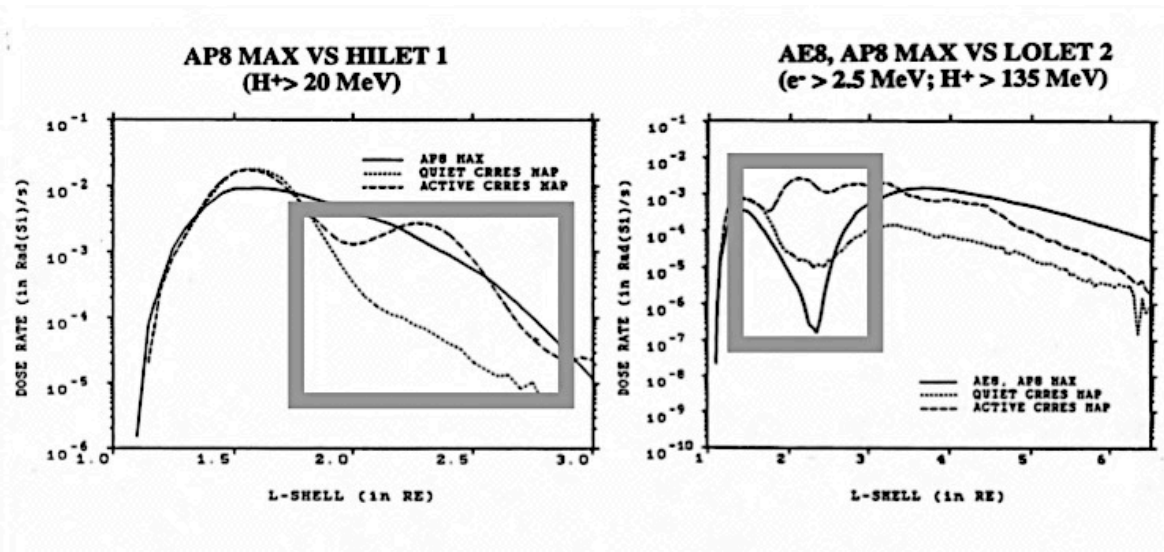

(A) (B)

Figure 28. Comparisons of A) the AP8 and CRRES models for E>20 MeV and B) the AE8 and CRRES models for electrons with E>2.5 MeV (and protons with E>135 MeV). The regions of greatest differences are indicated [29].

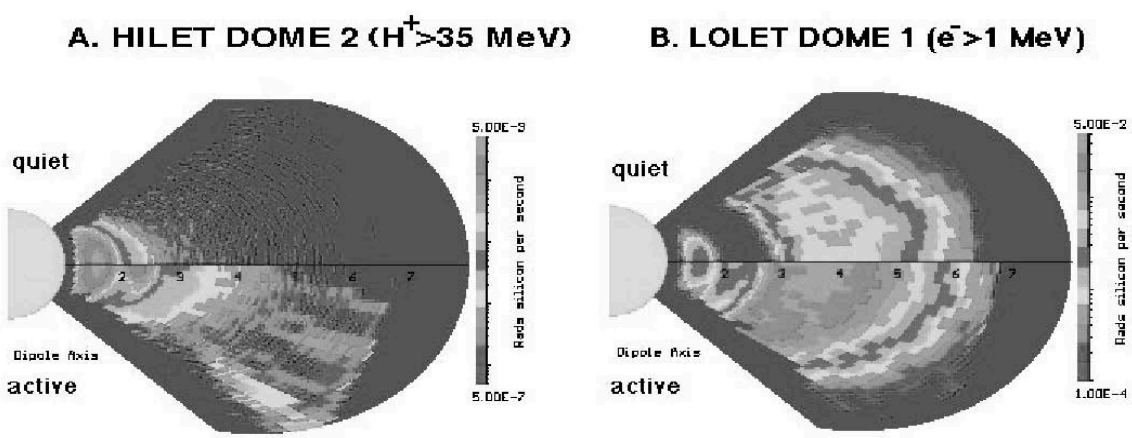

(A) (B)

Figure 29. Meridional plots of CRRES data for A) protons with E>35 MeV and B) electrons with E> 1 MeV. The upper plots are for "quiet" conditions and the lower for "active" conditions [29].

2.2.4.6.2 Magnetospheric Heavy Ions

There is currently only limited information available on heavy ions in the Earth's magnetosphere. O^+ and He^{++} are typically observed. The sources of these particles are not clear, however. The helium nuclei (mostly alpha particles) are likely from the solar wind [37], while the O^+ may be primarily of ionospheric origin. In the case of the solar wind, particles probably enter the magnetosphere and are accelerated by radial diffusion. This process, described by Cornwall [38], adequately describes the magnetospheric helium ion population [39, 40]. The bulk of the helium nuclei are, however, at energies too low to penetrate the walls of a spacecraft. C, N, and O ions have all been observed though it was not clear whether the particles were trapped in the magnetosphere (recent evidence supports the claim that the bulk of the O^+ is of ionospheric origin). Models by Adams and his colleagues [9] assume that there is a small flux of helium nuclei and a smaller flux of heavier nuclei in the magnetosphere above 10 MeV/nucleon. There are also reports of long-lasting enhancements of the low energy heavy ion fluxes after large solar flares, perhaps associated with the Galactic Cosmic Ray (GCR) anomalous component (see later). Blake and Friesen [37] suggested that the anomalous component particles, which may be only singly ionized initially, become more highly ionized near their geomagnetic cutoff and are subsequently trapped. This leads to a special trapped population of oxygen, nitrogen, neon, and other elements which may comprise the heavy ion component (see Table 2). As yet, these ions are included in radiation dosage calculations in only very specialized applications although they are of concern for SEU effects.

2.2.4.7 AP-9/AE-9: New Radiation Belt Model (Version Beta)

Fortunately, new models are on the way. Ginet, O'Brien, and their colleagues [41] are in the process of completing the AE-9/AP-9 trapped radiation models to improve the AE-8/AP-8 models. The new versions provide significantly more coverage in energy, time, and location for trapped energetic particles and plasma. The new models include estimates of instrument error and space weather statistical fluctuations. The Beta.3 version is now available (intended for test purposes only and is not to be used for satellite design or other applications!). It can be run in command line and GUI modes. The particles species, as in the AE8/AP8 models, cover the electrons and protons for the energies greater than 1 MeV and provide median, 50th, and 95th confidence levels of flux and fluence for arbitrary orbits. Dose calculations employ the ShieldDose program. In addition, the package includes the older AP8/AE8 and CRRES trapped models and CAMMICE/MICS plasma model with uncertainties added.

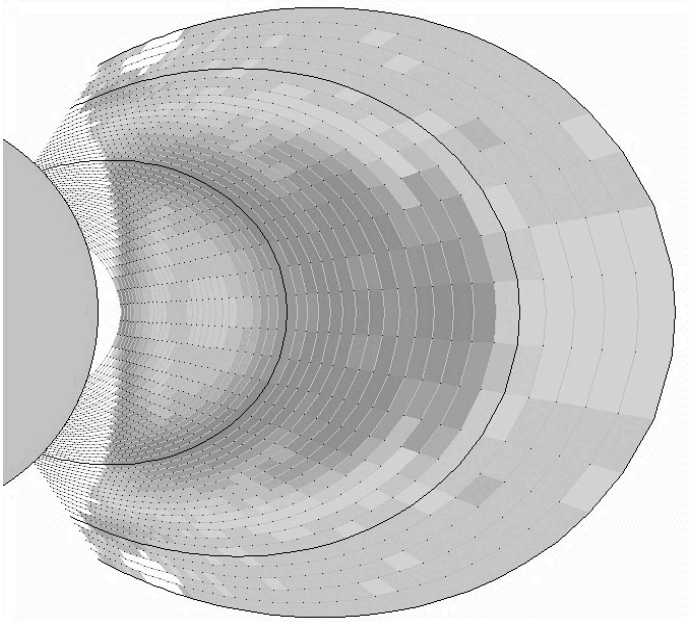

Figure 30. Example of a particle flux map provided by AE-9/AP-9. The fluxes are derived from empirical data for median and 95th% of distribution functions providing nominal and extreme environments [41].

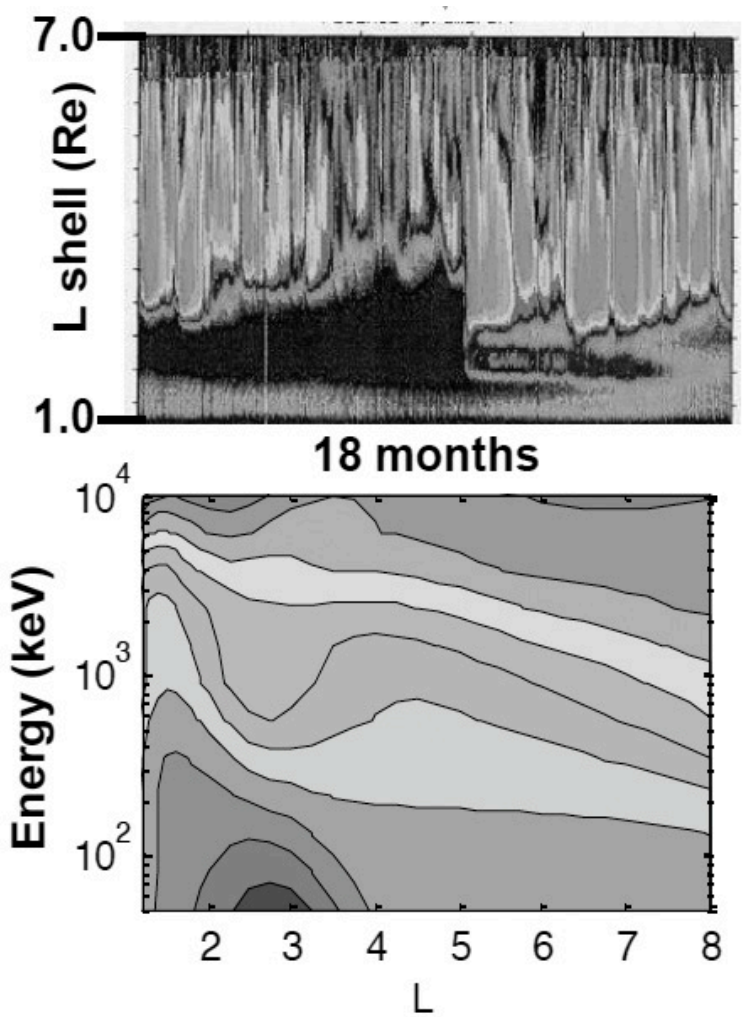

Figure 31. For AE-9/AP-9, in-situ observations (upper panel) are used to generate a statistical data base along with spatiotemporal covariance matrices. These are inverted (e.g., Monte Carlo techniques) to provide flux estimates in energy and position (lower panel) and to simulate time variations [41].

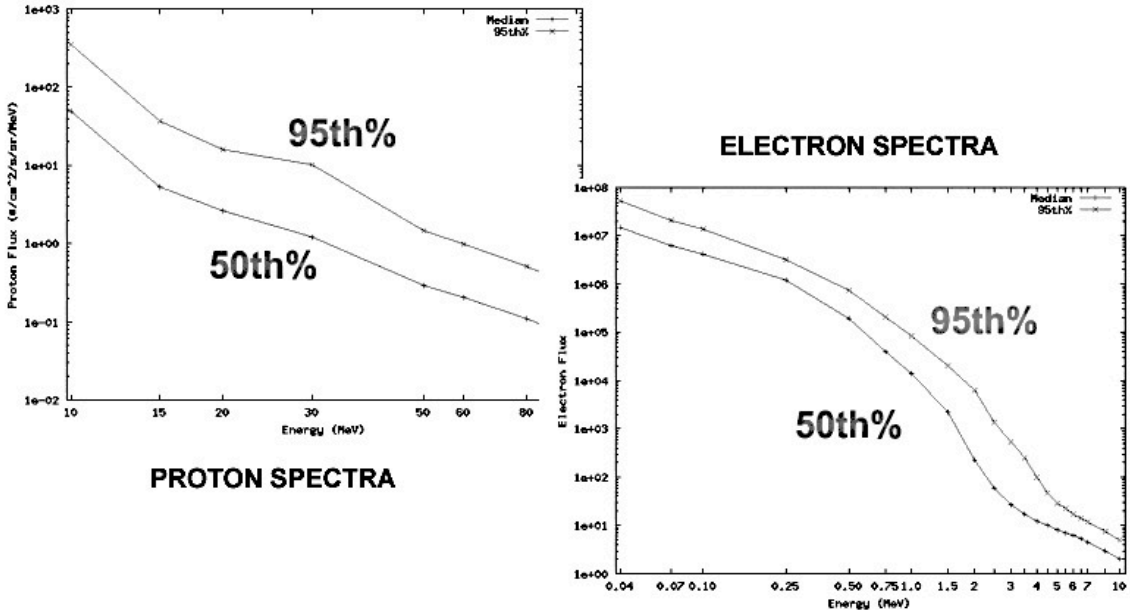

Figure 32. Sample AE-9/AP-9 50th and 95th percentile fluxes for the inner radiation zone (protons) and outer radiation zone (electrons) [41].

Version 1.0 is due in the third quarter of FY11. The new model employs a detailed LEO coordinate system to resolve loss cones and atmospheric density effects. Spectra were fit to ICO, HEO, TSX-5, and GPS electron data sets and the spectra inverted to obtain particle distributions. The data sets are being expanded to include POES, SAMPEX, and DSP-21/CEASE. The next planned version, Version 2.0 (to be issued 2 years after the RBSP launch), will include even more data sets:

- The NASA Radiation Belt Storm Probes instruments will give complete coverage (launch ~2012)
- DSX instruments will cover the slot region (to be launched ~2012)
- Due two years after RBSP launch

Table 4 lists the data sets currently used for the AE-9/AP-9 models and those planned to be incorporated in the future.

Fig. 30 is an example of a particle flux map provided by AE-9/AP-9. The fluxes can be derived from empirical data for different distribution functions (e.g., median and 95th%) providing nominal to extreme environments. Fig. 31 illustrates the process of employing in-situ observations (upper panel) to generate a statistical data base along with spatiotemporal covariance matrices which can be inverted (through Monte Carlo and other methods) to provide flux estimates in energy and position and to simulate time variations and space weather dynamics. The new models can even generate flux maps perturbed with error estimates to

simulate instrument uncertainties. Users will be able to run a statistical model N times with different random seeds to get N flux profiles that can then be aggregated to get profiles for median, 75th, 90th confidence levels of flux/fluences (Fig. 32). These can then be converted into dose rate, dose, or other quantities derivable from flux (Fig. 33).

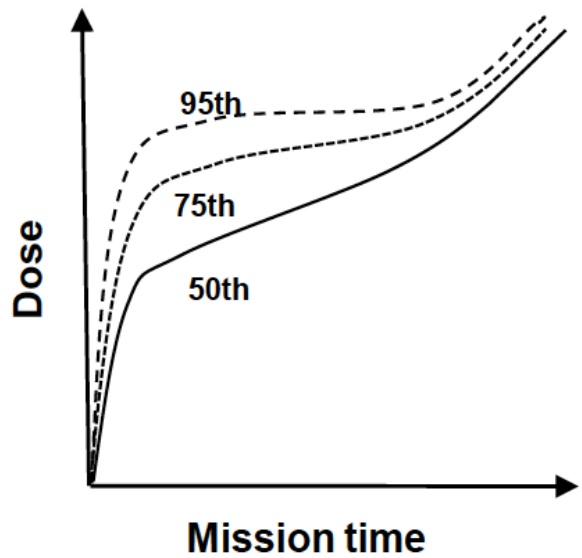

Figure 33. Examples of dose versus mission time computed for 50th, 75th, and 90th confidence levels of the flux and fluence such as given in Fig. 32 [41].

Table 4. Data sets included in the various versions of the AE-9/AP-9 models [41].

Data Set	Orbit/Duration	Measurements
HEO-1	Molniya, L>2, little coverage L<4, 1994 onward	Dosimeter, p+: >80, >160, >320 keV, >20, >40, >55, >66 MeV e- : >130, >230 keV, >1.5, >4, >6.5, >8.5 MeV
HEO-3	Molniya, L>2, 1997 onward	Dosimeter, p+: >80, >160, >320 keV, >5, 16-40, 27-45 MeV e- : >130, >230, >450, >630 keV, >1.5, >3.0 MeV
ICO	45°, 10000 km circular, MEO L>2.5, 2001 onward	Dosimeter, p+: >15, >24, >33, >44, >54 MeV e- : >1.2, >2.2, >4, >6, >8 MeV
TSX-5	67° LEO, 400 x 1700 km, June 2000- Jul 2006	CEASE (dosimeter & telescope), p+: 20 – 100 MeV, 4 int. channels; e- : 0.06 – 4 MeV, 5 int. chanels
CRRES	GTO, L>1.1, contamination issues in inner zone, Jul 1990 – Oct 1991	PROTEL, p+: 1 – 100 MeV, 22 channels HEEF, e-: 0.6 – 6 Mev, 10 channels; MEA(e-): 0.1 – 1.0 MeV LEPA, p+ & e-: 100 ev – 50 KeV
S3-3	97.5° MEO, 236 x 8048 km, 1976-1979	p+: 80 keV – 15.5 MeV (5 ch), > 60 MeV (no GF) e- : 12 keV – 1.6 MeV (12 ch)
GPS	54°, 20000 km, MEO L>4.2, Jan 1990 onwards	BDD/CXD, p+: 5/9 – 60 MeV e- : 0.1/0.2 – 10 MeV
Polar	90°, 1.8 x 9.0 Re, Feb 1996 – Apr 2008	CAMMICE/MICS, p+, O+: 1-200 keV/e HYDRA, p+, e-: 2 eV – 35 keV IES/HISTe, e-: 30 keV – 10 MeV
SCATHA	Near-GEO, 5.5 < L < 7.5, 1979 - 1989	SC3, e-: 0.05 – 4.6 MeV, 11 differential channels
MDS-1	GTO, L>1.1,2002-2003	Electron channels: ~0.5, ~1, ~2 MeV
AZUR	103°, 387 x 3150 km, 1969-1970	12 proton channels, 0.25- 100 MeV
GOES 7,8 & 11	GEO 1986 onwards	SEM, p+: 0.8 – 700 MeV, 10 differential channels >1, >5, >10, >30, >50, > 100 MeV integral channels
SAMPEX	LEO (500 km) 1992.5 onward	PET, p+: up to 400 MeV e- : >0.5, >1, 1-6, 3-16, 10-20 MeV
LANL - GEO	GEO 1985 onwards	MPA/CPA/ESP/SOPA, p+: 0.1 keV – 200 Mev e- : 0.1 keV - > 10 MeV
DSP-21	GEO Aug 2001 onward	CEASE (dosimeter & telescope) p+: 20 – 100 MeV, 4 integral channel e- : 0.06 – 4 MeV, 5 integral channels
TWINS F1	HEO 2006 onwards	Dosimeter, p+: > 8.5, > 16, > 27 MeV; e-: > 0.63, > 1.5, > 3 MeV

Version Beta

Version 1.0

Version 1.+

Validation Only

2.2.4.8 Conclusions

Modeling of the Earth's radiation environment is a complex process at best. For the purpose of studying radiation effects on long duration space missions, the AE8/AP8 models have proven to be very useful. There are, however, limitations to these models such as effects due to large, but short term temporal variations. Important, but less serious, are the effects that inadequate data coverage and the lack of recent data have on their accuracy. A new set of radiation models, AE-9/AP-9, address many of these limitations and will shortly be available for general use. The improvements in sizing satellite shielding to be expected with better models can not be underestimated. As a practical example, improvements in the knowledge of just the slope of the electron spectrum for energies greater than 2 MeV might mean perhaps as much as an order of magnitude reduction in the required shielding on a typical spacecraft (though factors of 2 are more likely) if it were demonstrated that the softer spectra were more appropriate for long mission.

2.2.5 Extraterrestrial Trapped Radiation

As in the case of the Earth, many of the other planets in the solar system have been observed to have trapped radiation belts. The species, abundances, energies, and time variations

of particles that are trapped in these radiation belts vary greatly depending upon the planet and its magnetic field. Planetary magnetic fields influence the particle spectrum that is observed near a planet in two ways--first, the magnetic field of the planet shields the planet from solar flare particles and from the GCR and, second, it allows particles to be trapped near the planet in radiation belts. Table 5 compares properties of the Earth, Jupiter, and Saturn. The Earth, for its size, has proportionally one of the most intense magnetic fields in the solar system. Jupiter and Saturn are roughly 10 times the size of the Earth while their magnetic moments are $\sim 2 \times 10^4$ and $\sim 10^3$ larger. This implies that as the magnetic field at the equator is proportional to the magnetic moment divided by the cube of the radial distance, Saturn's magnetic field/magnetosphere is proportional to Earth's while Jupiter's magnetic field/magnetosphere is 20 times larger than the Earth's. As the maximum energy and flux levels of trapped particles in a magnetosphere are proportional to the magnetic field strength, the Jovian system can maintain much higher particle energies than those at Saturn and the Earth or in interplanetary space. Subsequent flybys of Jupiter and Saturn have indeed born this out with Jupiter having much more intense radiation belts whereas Saturn's are roughly equal to Earth's.

Table 5. Comparison of the terrestrial, jovian, and saturnian properties.

	Earth	Jupiter	Saturn
Equatorial Radius (Km)	**6.38×10^3**	**7.14×10^4**	**6.00×10^4**
Magnetic Moment (G-cm^3)	**8.10×10^{25}**	**1.59×10^{30}**	**4.30×10^{28}**
Rotation Period (hrs)	**24**	**9.925**	**10.23**
Aphelion/Perihelion (AU)	**1.01/0.98**	**5.45/4.95**	**10.06/9.01**

Another key feature is that Jupiter and Saturn rotate extremely rapidly (10 hours versus 24 hours). At Jupiter, because of the very dense plasma torus associated with volcanic Io, the magnetic field of Jupiter is dragged out into a pronounced disk beyond L~16 (at Saturn, Titan generates a plasma disk but it is much farther out and much lower density then the jovian plasma sheet)—see Fig. 34. This outer radiation region is marked by significantly lower radiation levels and, as will be discussed later, is dependent on radius R and distance Z (normal to the plasma sheet) rather than B and L. The observed radiation rapidly varies sinusoidally as the magnetic field is tilted relative to the spin axis. As a result, a more complex magnetic field model is required and the spatial dependence of the radiation is similarly more difficult to model. Saturn, in contrast, has the peculiarity that its magnetic field is precisely aligned with its spin axis so that its radiation does not vary with spin.

Here, the discussion will concentrate on the inner Jovian radiation belts which, after the Earth's, are the best known and are by far the most intense in the solar system. A brief

discussion of the Saturnian belts will also be presented (the Uranian and Neptunian belts are also of interest but are not as yet well modeled; Mercury, Mars, and Venus have very weak magnetic fields and therefore no radiation belts). This model, based on Pioneer and Voyager data, will be subject to changes based as our understanding of the Saturn environment is currently greatly expanding based on Cassini observations and new models will be coming shortly.

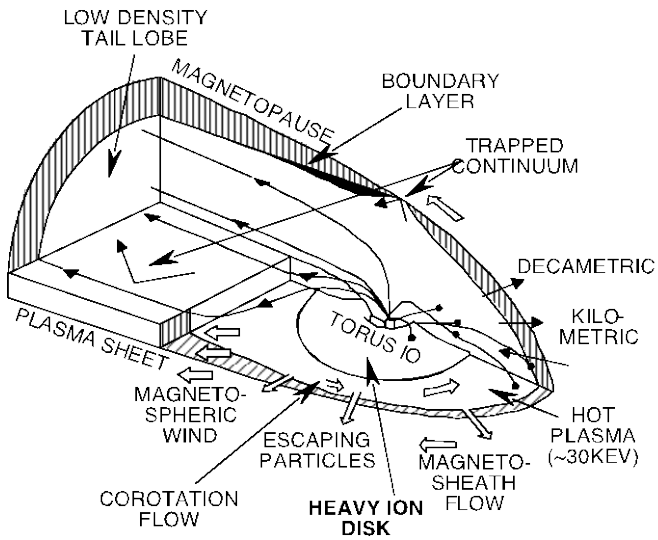

Figure 34. Schematic representation of Jupiter's magnetosphere illustrating the various plasma regions and particle flows [42].

2.2.5.1 Jupiter

The strongest magnetic field in the solar system is that of Jupiter. Since the ability to trap particles magnetically is a function of the magnetic strength, it is little wonder then that it has the most intense radiation belts yet observed. These belts are so intense in fact that they rival the man-made saturated nuclear environment at the Earth–-the most intense environment space systems will likely have to fly in. To date (the existing jovian radiation models are all currently undergoing revision as the Galileo data are being incorporated), the principle engineering models of these radiation belts are the Divine family of models [43, 44] and the European Salambo and Jose models [45, 46] listed in Table 6. The trapped versions of these models have many of the characteristics of the AE8/AP8 radiation models and thus can be reviewed in the same manner as the Earth's trapped radiation belts in terms of B and L.

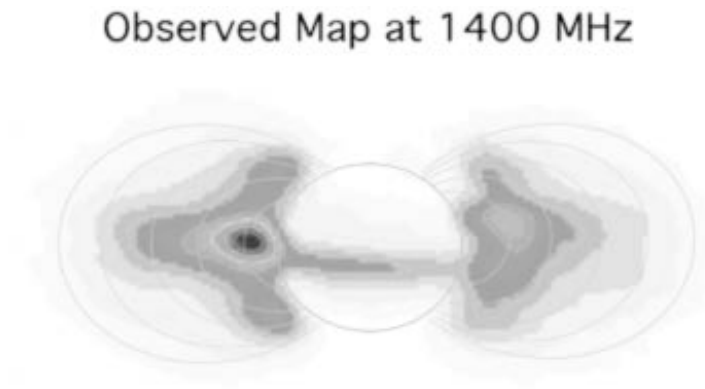

(A)

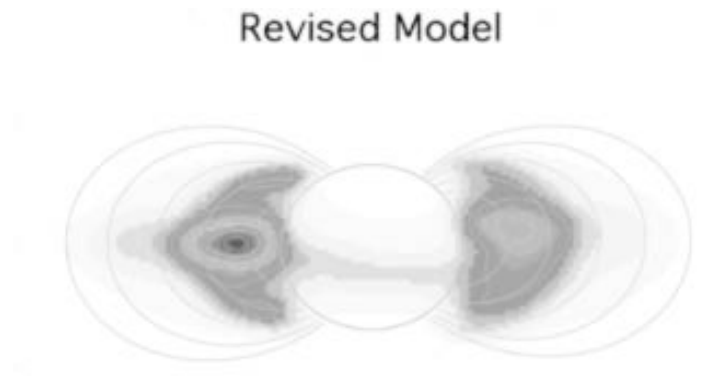

(B)

Figure 35. A) Earth-based observations of jovian synchrotron radiation at 1400 Mhz [47]. B) Simulated jovian synchrotron radiation at 1400 Mhz using the Divine family of jovian electron radiation models [47].

2.2.5.1.1 Introduction

Jupiter has been known to have a magnetosphere since about 1960 when, in analogy with early spacecraft observations of the Earth's radiation belts, it was realized that the Jovian UHF radio emissions could be interpreted in terms of trapped energetic electrons [48]. Fig. 35A shows ground based measurements of this jovian synchrotron radiation at 1400 Mhz. Early speculation by Brice [49, 50] and others attempted to draw parallels between this hypothesized Jovian magnetosphere and the then current ideas of the Earth's magnetosphere. In order to assess the potential hazard to the Pioneer 10 and 11 spacecraft, crude numerical models of the energetic electrons and protons were developed based on these speculations and the early radio observations. The successful encounters of the Pioneer spacecraft with the Jovian magnetosphere gave rise to a number of quantitative models describing various aspects of the Jovian magnetosphere [51, 52]. In particular, magnetic field models by Smith et al. [53] and Acuna and Ness [54, 55] began to delineate the substantial differences that exist between the Jovian and

terrestrial magnetospheres. Pronounced wave-like variations in the high energy particle fluxes led to the proposal that the Jovian magnetosphere was distorted into a thin disc--the so-called magnetodisc theory (Fig. 34 [56])—and that this thin disc was populated by a cold plasma consisting of heavy ions originating from Io. The passage of the Voyager 1 and 2 spacecraft, while failing to distinguish between the magnetic-anomaly and magnetodisc models, further refined the particle and field observations. Subsequently, theoretical models have further helped to interpret the observations and have led to the development of Jovian magnetospheric models capable of making practical predictions about the environment around Jupiter (see [51, 52]). Two families of jovian radiation models, one associated with Divine and his colleagues at JPL and the others based in Europe have been developed from these early flybys and the subsequent Galileo mission which completed 35 orbits of Jupiter between 1995 and 2003. Table 6 lists these models and their references. Here, the Divine models will be described as they have been the standard design tool for the Jupiter Europa Orbiter mission.

Table 6. Current jovian radiation belt models and references:

Divine Family of Electron and Proton Models:

Divine

- Divine, N. T., Garrett, H. B., "Charged Particle Distributions in Jupiter's Magnetosphere", J. Geophys. Res., 88, 6889-6903, 1983

Galileo Interim Radiation Electron Model

- Garrett, H. B., I. Jun, J. M. Ratliff, R. W. Evans, G. A. Clough, and R.W. McEntire, "Galileo Interim Radiation Electron Model", JPL Publication 03-006, 72 pages, The Jet Propulsion Laboratory, California Institute of Technology, Pasadena, CA, 2003.
- http://www.openchannelfoundation.org/projects/GIRE/

European Jovian Models:

Salammbô

- Sicard-Piet, A., and S. Bourdarie, "Physical Electron Belt Model from Jupiter's surface to the orbit of Europa" J. Geophys. Res., 109, A02216, doi:10.1029/2003JA010203, 2004.

JOSE

- Sicard-Piet, A., and S. Bourdarie, "JOSE (JOvian Specification Environment)", TN-CCN/13279 DESP, ONERA-DESP, The French Aerospace Lab, pp. 134, February 2010.

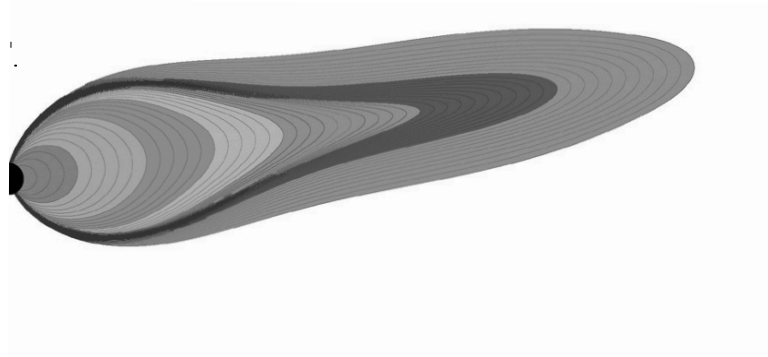

Figure 36. Magnetic field lines at Jupiter for the VIP4 magnetic field model [57, 58] showing the 11° tilt of the dipole moment and the extended magnetic field resulting from the Io plasma dragging out the field beyond L~16.

2.2.5.1.2 Jovian Coordinate System

As for the Earth, the independent variables used to define position for the magnetic field and charged particles are jovicentric distance r (commonly in m or R_J), latitude λ (deg or rad), longitude l (deg in System III (1965) [59]), distance z=r sin λ from the rotational equatorial plane, and distance R=r cos λ from the rotation axis. The value of the Jovian equatorial radius is assumed to be 1 R_J=7.14 x 10^7 m. The common angular speed of rotation of Jupiter's internal magnetic field and of a meridian of constant longitude l in System III (1965) coordinates is assumed to be ω=870.536 deg/day≈12.6 km/s R_J. In this system, l, the longitude, increases westward (opposite to the azimuthal angle in a system of spherical coordinates). Conversions to inertial and other coordinate systems may be derived from Seidelmann and Divine [59].

2.2.5.1.3 Magnetic Field Model

There are several detailed magnetic field models of Jupiter. An example of the inner dipole structure of the trapped magnetic field is the VIP4 [57, 58]. This model accounts for the pronounced jovian plasma sheet and its distortion of the magnetic field beyond ~16 L (Fig. 36). Outside of ~16 L, a more recent Khurana magnetic field model [60] has been developed to model the effects of outer, plasma sheet magnetic field. To first order, however, a simple offset tilted dipole model (e.g., the D4 derived from the Pioneer helium vector magnetometer data; [53] can be used to illustrate the shape of the inner radiation belts [43]. This inner dipole is offset about 0.1 R_J and tilted about 10.77° (note: the magnetic field of Jupiter and Saturn are both oriented 180° to that of the Earth's). The vector components of this tilted magnetic field may then be derived from the D4 model using standard dipole relations [53]. The magnetic field strength is given by

$$B = (M / r^3)(1 + 3(\sin\lambda)^2)^{1/2} \tag{35}$$

and the shape of a field line, along which the magnetic shell parameter L is constant, is given by

$$L = (r / R_J)(\cos\lambda)^{-2} \tag{36}$$

The dipole moment has the value M =1.538x10^{27} m^2 A = 4.225 G-R$_J^3$ and the tilt colatitude of 10.77° equals the inclination between the rotational and magnetic equatorial planes.

2.2.5.1.4 Radiation Belt e$^-$ and H$^+$

The principle radiation belt populations included in the jovian models are, as in the case of the Earth, electrons (E>0.06 MeV) and protons (E>0.6 MeV). For the Divine/GIRE models, the range of applicability of the energetic electron model extends to the Jovian magnetopause while that of the protons are currently limited to L=12. The Divine and GIRE electron models currently include a pitch angle dependency within L=16 but are considered isotropic beyond that point. The proton model includes a pitch angle dependency within L=12. For the inner electron and proton models, the independent variables magnetic L shell, local field strength B, pitch angle α with respect to the field line, and particle kinetic energy E were utilized (B and L are of course functions of r, λ, and *l*). The model populations are assumed independent of time, longitude, and direction azimuth about the field line, as appropriate for stably trapped populations.

At each value of L, analytic expressions have been developed (these values are tabulated in Divine and Garrett [43]), based on fits to the spacecraft and radio data, that allow evaluation of the particle integral and differential intensities I and i in terms of α, B, and E. That is, I has been fit to an analytic expression in α, *B*, and *E* at discrete values of L such that:

$$I_L = A_L(\alpha, B, E) \tag{37}$$

Variations at other values of L are derived by interpolating between the relevant values. The corresponding differential intensity (in units of cm^{-2} s^{-1} sr^{-1} MeV^{-1}) is then given by:

$$i = -\frac{dI}{dE} \tag{38}$$

Electron and proton omnidirectional fluxes are obtained by integration

$$J = 4\pi \int_0^{\pi/2} I(\sin\alpha) d\alpha \tag{39}$$

Improvements inside L=~5 were recently derived by matching the model predictions to UHF radio observations from Earth (Garrett et al., 2005) (see Fig. 35B).

In the middle and outer Jovian magnetosphere (i.e., beyond L=16), the energetic particle fluxes are extremely time-dependent and are, as a result, difficult to model. Currently, to estimate radiation effects in the outer jovian radiation belts, simple, omnidirectional models for the energetic electron fluxes, based on Pioneer, Voyager, and Galileo observations, varying in R and Z_K. The European JOSE model and a forthcoming update to the GIRE model assume that the peak equatorial fluxes can be described by a function of the form for R>16-20 Rj to 50 Rj:

$$J(E, R, Z_K, t) \approx J_0(E) e^{\left(\frac{Z_K - Z_0}{H_Z}\right)} G(R) \tag{40}$$

Where

J =Omni-directional electron flux; Function of E, R, t, and Z_K

E =Energy

R=Radial distance from Jupiter

G=Functional variation of flux with radius R (e.g., $G(R) \sim e^{-A_0 R}$)

Z_0, H_Z, A_0=Constants

J_0=Functional variation of Flux with energy E

Z_K=Distance normal to the plasma sheet magnetic plane; currently estimated using the Khurana magnetic field model which is dependent on the date and time given by t

t=Date/time of observation

Here the electron kinetic energy E has units MeV, R has units R_J, and the omnidirectional integral flux J has units of $cm^{-2} s^{-1}$.

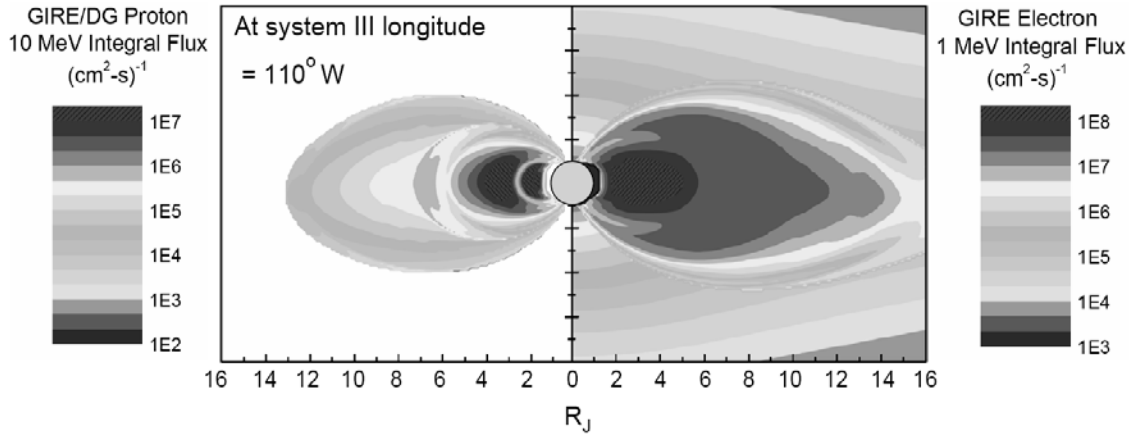

Figure 37. Contours for electron fluxes above 1 MeV and protons above 10 MeV at Jupiter [43, 44].

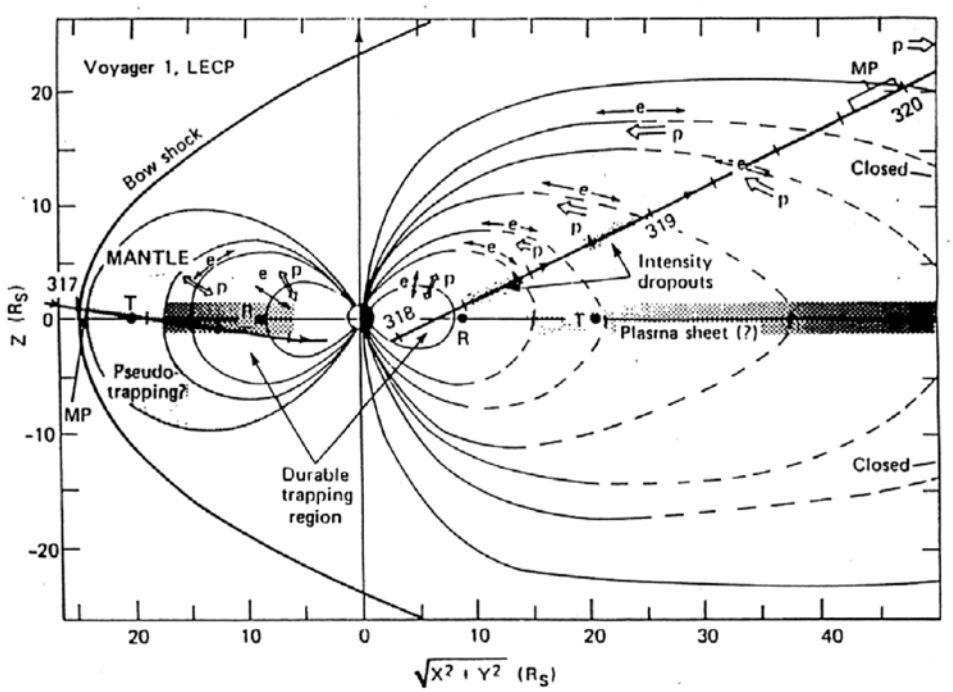

Figure 38. A schematic representation of Saturn's magnetosphere in the r-z (trajectory) plane as revealed by the LECP data [61]. Tick marks on the trajectory are at 6-hour intervals from day 318 to 320. Note the Titan-associated mantle region outside ~ 17 R_S, and the presence of closed field lines in the tail lobe region. The phase of the second-order anisotropies relative to the magnetic field (B) is shown for both electron (e) and protons (p). R, Rhea: T, Titan: MP, magnetopause.

2.2.5.2 Saturn

Fig. 38 [61] is a schematic illustration of the Saturn magnetosphere. As in the case of Jupiter, Divine [62, 63] developed a first order radiation model for Saturn similar to that for Jupiter (this model, called SATRAD, is available through Open Channel—see references). Based on high energy data from Pioneer 11, Voyager 1, and Voyager 2, the model covers the distance from 2.3 to 13 R_S. It describes the electron distribution at energies between 0.04 and 10 MeV and the proton distribution between 0.14 and 80 MeV. As in the Jupiter model, the first step in the model is to specify the Saturnian magnetic field. Estimates for this field and other relevant quantities are listed in Table 7. Next, the integral and differential intensities for the electrons and protons, as functions of the magnetic field and L, are specified by algorithms very similar to the Jupiter model. The integral omnidirectional flux J is then calculated as before by Eq. 39. The output of the SATRAD model is presented in Fig. 39. The integral omnidirectional flux for the Saturn model at 1 MeV (electrons) and 10 MeV (protons) are shown. The dropouts are typically associated with the orbits of the Saturnian moons or rings.

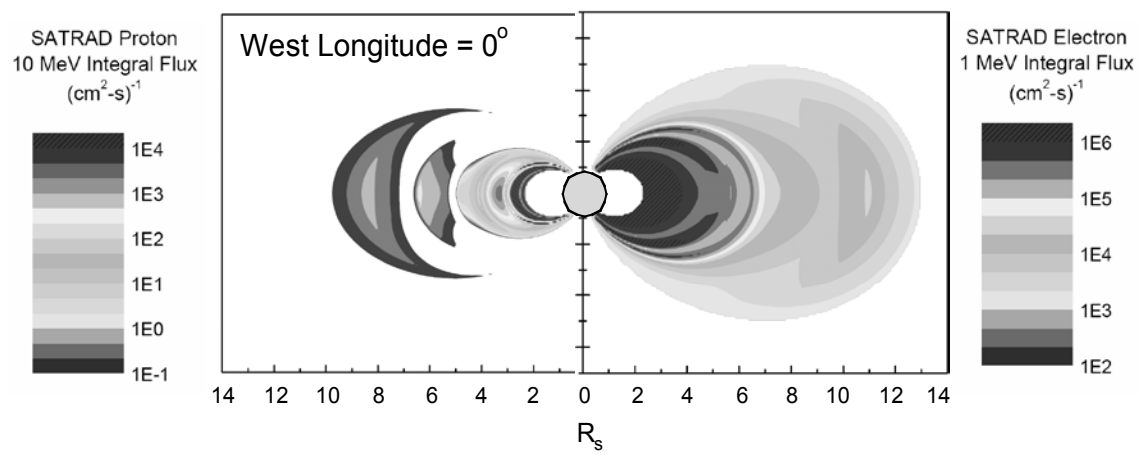

Figure 39. Sample output for the SATRAD model: The integral omnidirectional flux for electrons at 1 MeV (right) and protons at 10 MeV (left) are shown. The dropouts are typically associated with the orbits of the Saturnian moons or rings [62, 63].

Table 7. Parameter values for Saturn used in model calculations [58].

QUANTITY	VALUE
Radius	R_S=6.033×10^7 m
Gravitation	GM_S=3.794×10^{16} m^3/s^2
Rotation	ω=810.76 deg/day
Magnetic field coefficients	g_1^0=0.21535 G
	g_2^0=0.01642 G
	g_3^0=0.02743 G
	G_1^0=-0.0001 G
	G_1^1=-0.00001 G

2.2.6 Galactic Cosmic Rays (GRC)

2.2.6.1 Overview

The third source of background radiation is the Galactic Cosmic Rays or GCRs. Galactic Cosmic Rays are primarily interplanetary protons, electrons, and ionized heavy nuclei with energies ranging from ~1 MeV/nucleon to over ~10^{10} eV/nucleon. The existence of the particles was originally detected by sensors on the Earth—when these high energy particles strike the upper atmosphere they can generate a shower of secondary particles. A schematic drawing of such a cosmic ray shower is illustrated in Fig. 40. The shower consists of high energy neutrons and protons, their disintegration products, pions, mesons, electrons, and gamma rays are created from one incident GCR particle. Fig. 41 compares GCR proton and electron spectra while Fig. 42 displays the observed cosmic ray abundance distribution of the chemical elements in the energy range from ~100 MeV/nucleon to ~1 GeV/nucleon for hydrogen to the iron group [64]. For comparison, solar system abundances are also shown in the figure. Note that the two abundance distributions are strikingly similar. The major components are hydrogen (93.6 percent) and helium (6.3 percent). The remaining 0.14 percent includes all the rest of the elements. Observations indicate that outside the Earth's magnetosphere, the cosmic ray fluxes are isotropic to within about 10% over their entire energy range, suggesting that they are of galactic and/or extragalactic origin. Within the magnetosphere, however, they are not isotropic. That is, for the low Earth orbit environment, the geomagnetic field provides shielding against incident GCRs (and solar flare particles) as it can effectively deflect through the Lorentz force the lower energy particles. Because of the approximate dipole nature of the geomagnetic field, vertical particle velocities in the polar regions are essentially parallel to the magnetic field resulting in almost no Lorentz force so that the particles can gain direct access. At low inclinations, only particles with sufficiently high energy, or "rigidity", can penetrate through the

magnetic shielding as the charge particles are forced into gyro loops by the magnetic field as they approach the Earth. This effect, illustrated schematically in Fig. 43 [6], is discussed in more detail in the next subsection.

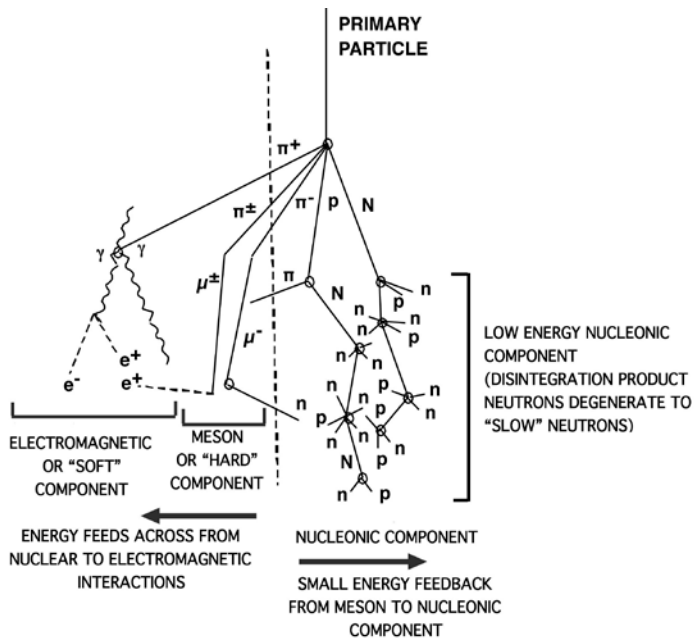

Figure 40. Schematic drawing of a cosmic ray shower. N and P are high energy neutrons and protons while the lower case n and p are used to denote disintegration product neutrons and protons. Pions, mesons, electrons, and gamma rays are indicated by conventional symbols [6].

2.2.6.2 Magnetic Shielding

Earth's magnetic field serves as an extremely effective shield for low to medium energy cosmic rays. Very succinctly, as in the case of a trapped charged particle, a cosmic ray penetrating the Earth's magnetic field begins to execute a circular motion around the magnetic field. Dependent on its energy, mass, and charge, the gyro-radius or penetration distance of the particle may or may not reach to the inner magnetosphere or surface of the Earth. This ability to penetrate the magnetic field, proportional to the gyro-radius of the particle, is determined uniquely by the cosmic ray's momentum divided by its charge and is called the particle's rigidity:

$$P = \frac{pc}{q} \tag{41}$$

where:

P = rigidity

p = momentum of particle

c = speed of light

q = charge of particle

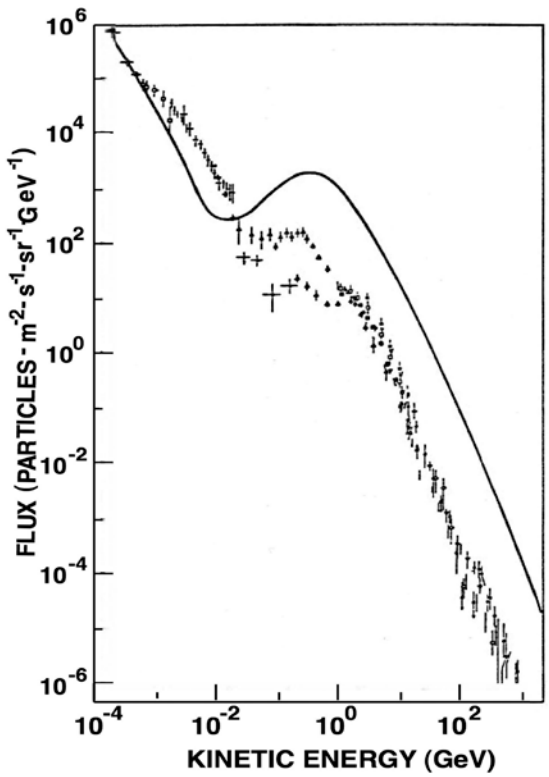

Figure 41. The energy spectra of cosmic-ray protons (line) and electrons (points) as measured near Earth [64]. Below a few GeV, interstellar spectra are strongly influenced by the Sun.

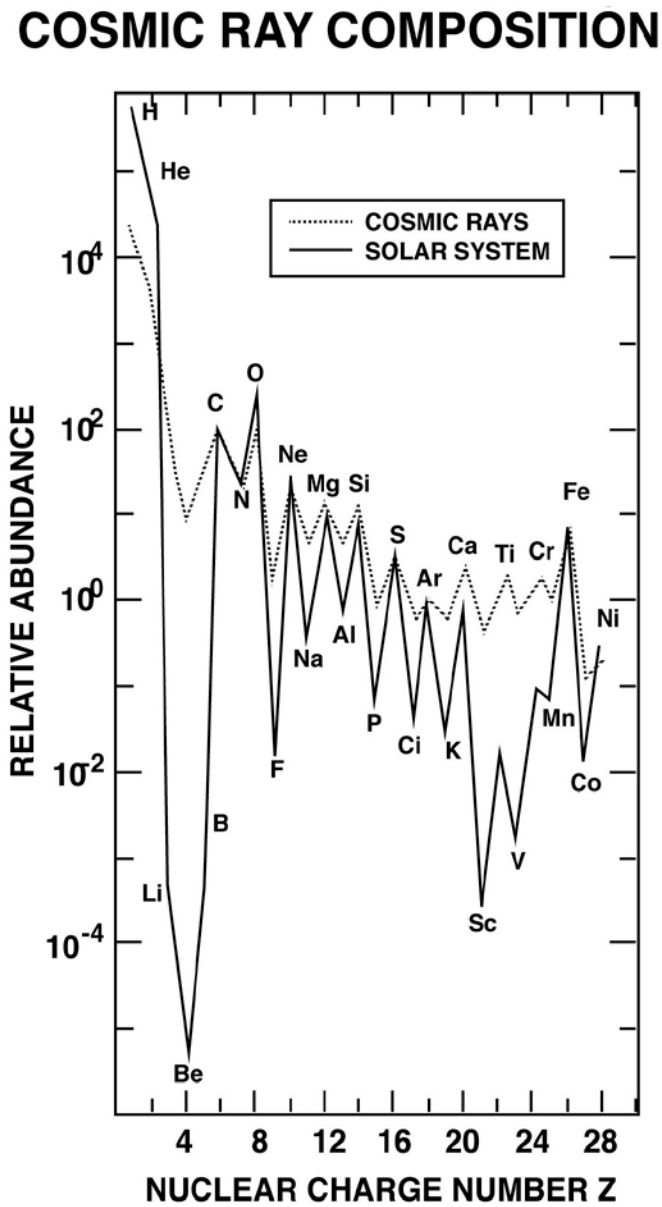

Figure 42. Relative abundance of the elements from hydrogen to the iron group, normalized to that of carbon (C=100) [64]. The solid line represents the cosmic-ray abundances measured near Earth. The dots represent the elemental abundances in the solar system of the GCR.

If pc is in eV, then q is the number of charge units and P is in volts. Typical units are MV or GV. There is a minimum magnetic rigidity a cosmic ray must possess to arrive from a given direction at a given point in the magnetosphere. Regions in the outer magnetosphere and near the poles can be reached by much lower magnetic rigidities than near the Earth's equator. In general, for each point in the magnetosphere and for each direction at that point, there exists a rigidity below which cosmic rays cannot arrive. This value is called the geomagnetic cutoff. For rigidities above this value, cosmic rays can arrive freely, almost as if no magnetic field were

present. Fig. 43 illustrates how the rigidity is convolved with the GCR spectrum outside the Earth to obtain the spectrum for a given orbit [65].

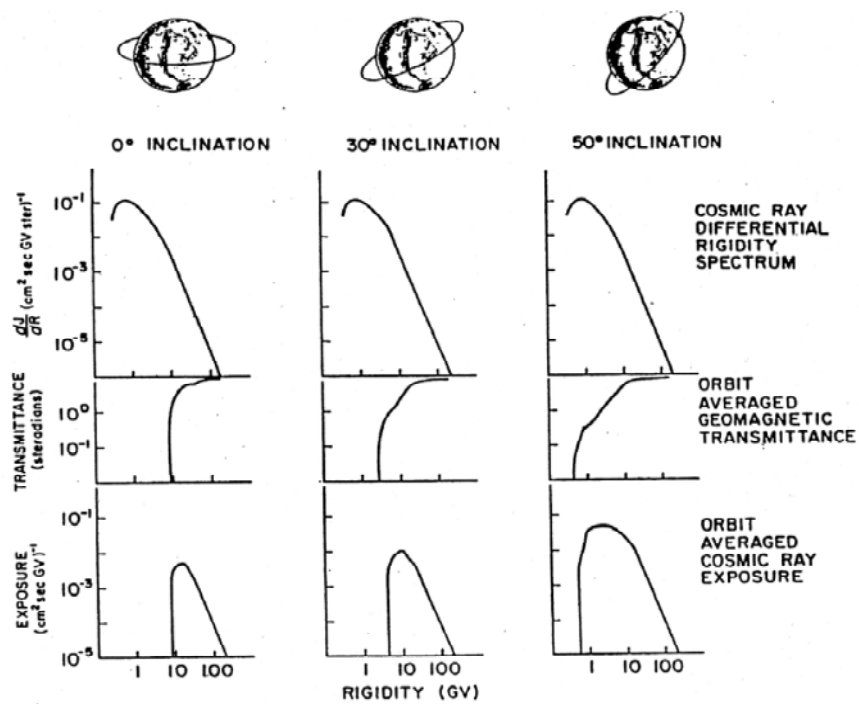

Figure 43. Schematic representations [65] of the effects of the Earth's magnetic field on the Cosmic Ray environment as functions of particle rigidity and orbital inclination. The top 3 spectra represent the Cosmic Ray spectrum outside the Earth's field. The second set of figures represents an orbit average geomagnetic transmittance factor which is a function of rigidity and orbital inclination. The third plot is the result of convolving the 2 upper sets of curves and is the orbit average Cosmic Ray exposure as a function of rigidity for 0°, 30°, and 50° inclination orbits.

2.2.6.3 GCR Ion Spectra

The most abundant element in cosmic rays is hydrogen. Fig. 44 [64] compares the differential energy spectrum of GCR hydrogen (primarily H^+) for solar maximum and solar minimum conditions with other GCR ion spectra. At very high energies, a power law with a spectral index of 2.75 is a good fit. The deviation below about 5 GeV/amu is thought to be due to solar modulation. As the amount of solar modulation depends on the general level of solar activity, there is a variation from solar minimum to solar maximum. Hydrogen, helium, carbon, oxygen, neon, magnesium, silicon, sulfur, calcium, and iron are assumed to be primarily primordial (that is, the hydrogen flux consists of the originally created ions and has not been created by transmutation during transit across the galaxy). These heavier ions are thus believed to have similar energy spectra.

Adams and colleagues [9] created a family of GCR heavy ion model spectra corresponding to the curves shown in Fig. 44. The models provide fits to the hydrogen, helium, and iron spectra along with a formula for scaling other elements to these 3 basic spectra. As lithium, beryllium, and boron are assumed to be entirely composed of secondaries and nitrogen is assumed to be a mixture of primary and secondary particles, they have energy dependencies different from these 3 base species. The NRL models take these variations into account by modifying the ratio to either helium or iron as a function of energy. The differential energy spectra of hydrogen (f_1), helium (f_2), and iron (f_{26}) nuclei are estimated for energies above 10 MeV/amu by:

$$f(E,t) = A(E) \sin\{ \omega(t - t_O) \} + B(E) \tag{42}$$

where:

ω = 0.576 radians per year

t_O =1950.6 AD

t =date (in years)

E =particle energy in MeV/nucleon

$A(E)=0.5\ (F_{max} - F_{min})$

$B(E)=0.5\ (F_{min} + F_{max})$

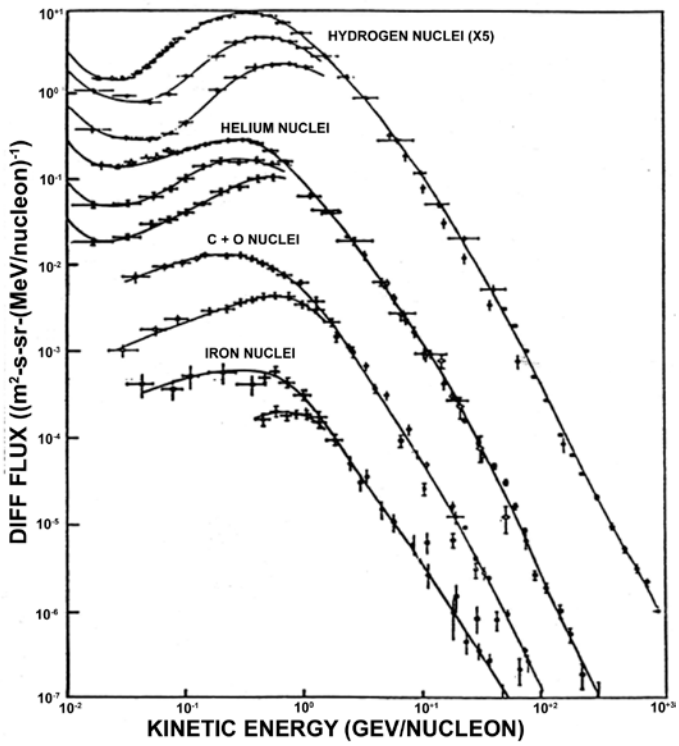

Figure 44. Cosmic-ray energy spectra [64] of the more abundant nuclear species as measured near Earth. Below a few GeV/nucleon, these spectra are strongly influenced by modulation within the solar system. The different curves for the same species represent measurements at various levels of general solar activity, the lowest intensity being observed at the highest activity level.

The units of f are particles/m^2-ster-s-MeV/μ. The functions F_{min} and F_{max} refer to solar minimum and solar maximum conditions for the following equation and differ by constants:

$$F = 10^{m}\left(\frac{E}{E_o}\right)^{a} \tag{43}$$

where:

$$m = C_1 e^{-X_2[\log_{10} E]^2} - C_2 \tag{44}$$

The exponent of the energy ratio changes from solar minimum to solar maximum. It is given by:

$$a = a_o\left\{1 - e^{-X_1(\log_{10} E)^b}\right\} \tag{45}$$

The fitted parameters for hydrogen, helium, and iron are given in Table 8 [3]. Using these three spectral shapes, the rest of the elements are then modeled using the ratios in Tables 9a and 9b.

Table 8. Parameters for the Adams' Model for Hydrogen (f_1), Helium (f_2), and Iron (f_{26}) GCR Spectra [3].

Parameter	Hydrogen	Helium	Iron
α_0	-2.20	-2.35	-2.14
E_0	1.1775E5	8.27E4	1.175E5
b	2.685	2.070	2.64
X_1 for Fmin	0.117	0.241	0.140
X_1 for Fmax	0.079	0.180	0.102
X_2	0.80	0.83	0.65
C_1	6.52	4.75	6.63
C_2	4.0	5.10	7.69

The preceding illustrate the basics of a GCR model. This model and other radiation models have been collected together on-line as part of the CRÈME web tools. Up until recently, the CRÈME96 was the primary model. The GCR CREME96 model was developed for the solar-minimum GCR environment and corresponds with the GCR maximum observed in 1986-87 (see below). The model [66] includes anomalous cosmic ray fluxes (visible for He, N, O and Ne around 10 MeV/nucleon) derived from SAMPEX results. This year CREME96 is being replaced by the most current version of the tool, CRÈME-MC, which was developed by NASA Marshall, Vanderbilt University, and the University of Huntsville [67] and can be found at:

https://creme.isde.vanderbilt.edu/CREME-MC/help/flux-space-ionizing-radiation-environment-model

Table 9a. Hydrogen to Nickel differential energy spectra parameters for Galactic Cosmic Rays [3].

Element (Z):	Ratio:	Energy dependence:
H (1)	-	f_1
He (2)	-	f_2
Li (3)	0.330	f_2 G(E)
Be (4)	0.176	f_2 G(E)
B (5)	0.480	f_2 G(E)
C (6)	3.04 E-2	f_2
N (7)	-	f_2 W(E)
O (8)	2.84 E-2	f_2
F (9)	6.06 E-4	f_2
Ne (10)	4.63 E-3	f_2
Na (11)	1.02 E-3	f_2
Mg (12)	6.02 E-3	f_2 S(E)
Al (13)	1.07 E-3	f_2
Si (14)	4.63 E-3	f_2 S(E)
P (15)	2.34 E-4	f_2
S (16)	9.30 E-4	f_2 S(E)
Cl (17)	0.070	f_{26} Q(E)
Ar (18)	0.130	f_{26} Q(E)
K (19)	0.090	f_{26} Q(E)
Ca (20)	2.1 E-1	f_{26}
Sc (21)	0.042	f_{26} Q(E)
Ti (22)	0.147	f_{26} Q(E)
V (23)	0.070	f_{26} Q(E)
Cr (24)	0.140	f_{26} Q(E)
Mn (25)	0.100	f_{26} Q(E)
Fe (26)	-	f_{26}
Co (27)	3.40 E-3	f_{26}
Ni (28)	5.00 E-2	f_{26}

where:

f_1, f_2, f_{26} = Spectra for H, He, and Fe (given by Eq. 42)

G(E)= $0.021\ f_2$ for $E < 3000$ MeV/υ

$0.729\ E^{-0.443}\ f_2$ for $E > 3000$ MeV/υ

W(E)= $\{8.70E\text{-}3 \exp(-0.4(\log_{10}E-3.15)^2) + 7.6E\text{-}3 \exp(-0.9(\log_{10}E-0.8)^2)\}$

S(E) = 1.0 for $E < 2200$ MeV/μ

$1.0 + 1.56\times10^{-5}\ (E-2200)$ for $E > 2200$ MeV/μ

Q(E) = $16\ \{1 - \exp(-0.075\ E^{0.4})\}E^{-0.33}$

Table 9b. Ratios for Copper to Uranium abundances relative to Iron for the Galactic Cosmic Ray models [3].

Z	Element	Ratio to Iron	Z	Element	Ratio to Iron
29	Cu	6.8 E-4	61	Pm	1.9 E-7
30	Zn	8.8 E-4	62	Sm	8.7 E-7
31	Ga	6.5 E-5	63	Eu	1.5 E-7
32	Ge	1.4 E-4	64	Gd	7.0 E-7
33	As	9.9 E-6	65	Tb	1.7 E-7
34	Se	5.8 E-5	66	Dy	7.0 E-7
35	Br	8.3 E-6	67	Ho	2.6 E-7
36	Kr	2.3 E-5	68	Er	4.3 E-7
37	Rb	1.1 E-5	69	Tm	8.9 E-8
38	Sr	3.6 E-5	70	Yb	4.4 E-7
39	Y	6.8 E-6	71	Lu	6.4 E-8
40	Zr	0.7 E-5	72	Hf	4.0 E-7
41	Nb	2.6 E-6	73	Ta	3.6 E-8
42	Mo	7.1 E-6	74	W	3.8 E-7
43	Tc	1.6 E-6	75	Re	1.3 E-7
44	Ru	5.3 E-6	76	Os	5.6 E-7
45	Rh	1.5 E-6	77	Ir	3.7 E-7
46	Pd	4.5 E-6	78	Pt	7.2 E-7
47	Ag	1.3 E-6	79	Au	1.3 E-7
48	Cd	3.6 E-6	80	Hg	2.3 E-7
49	In	1.4 E-6	81	Tl	1.8 E-7
50	Sn	7.5 E-6	82	Pb	1.7 E-6
51	Sb	9.9 E-7	83	Bi	9.0 E-8
52	Te	5.7 E-6	84	Po	0
53	I	1.5 E-6	85	At	0
54	Xe	3.5 E-6	86	Rn	0
55	Cs	5.8 E-	87	Fr	0
56	Ba	6.0 E-	88	Ra	0
57	La	5.3 E-	89	Ac	0
58	Ce	1.6 E-	90	Th	9.0 E-8
59	Pr	3.0 E-	91	Pa	0
60	Nd	1.1 E-	92	U	5.4 E-8

In the new CRÈME-MC, the GCR model has been replaced with a semi-empirical Moscow State University (MSU) model (International Standard ISO Draft 15390 [68]). This new tool will provide descriptions of reference space radiation environments for peak fluxes, event-integrated and mission-integrated fluences, elemental energy spectra for protons, helium, and heavier ions. The geomagnetic cutoff model for the GCRs, currently the Shea and Smart 2006 GCR tracing model, is being updated and will include the Tsyganenko magnetospheric field model and the International Geomagnetic Reference Field.

2.2.6.4 GCR Variations

The flux of GCR increases radial with distance from the Sun. The magnitude of the radial gradient varies with both ion species and energy. For relativistic GCRs the radial gradient is <4%/AU while for GCR particles below 100 MeV/μ the gradient is <10%/AU. The latitudinal gradient is small, under 1% per degree and may change sign each half solar cycle. The solar wind further modulates the GCR inversely with the 11 year cycle of solar activity. At the maximum of solar activity, GCR intensity is at a minimum and vice versa. The GCR intensity, at moderate energies, varies by a factor of 4 to 8 depending on the energy and ion [9]. The reason for the modulation of the GCR is apparently the solar wind magnetic field. As the GCR propagation is controlled by this field, any turbulence in the field (such as that associated with solar maximum) makes propagation of the GCR into the inner solar system more difficult–the particles are scattered more effectively. As the solar wind field relaxes during solar minimum, the GCR can more easily reach the inner solar system. The last 2-3 years were exceptionally devoid of solar activity. As a result, the level of GCR reached an unusually high level compared to previous solar cycles during the space age. To account for such solar-cycle variations in the GCR intensities, 12 month averages of the Wolf sunspot number are used in the latest models. The variations in the large-scale heliospheric magnetic field are assumed to be proportional to the variations of the Sun's polar magnetic field whose intensity and polarity are taken to be dependent on solar activity and on whether a given solar cycle is even or odd. The time lag of GCR flux variations relative to solar activity variations is taken to depend on magnetic rigidity of particles, on whether a solar cycle is odd or even, and on solar cycle phase.

In addition to the temporal and spatial variations in the GCR, there is an occasional systematic change in the energy spectra for some ions. This so-called anomalous component appears as a flattening in the differential energy spectra of ions like helium, oxygen, nitrogen, and neon. The anomalous component may be singly ionized particles with an energy in the range from 1 to 200 MeV/μ--a component which is not always present near the Earth [9]. The anomalous component varies by a factor of 100 to 1000 over the 11 year solar cycle–it appeared between 1971 and 1972 and disappeared again during the solar maximum of 1978. Jokipii et al. [69] predicted that the anomalous component appears near the Earth only once every other solar minimum. The anomalous component seems to be more intense at greater distances from the Sun. Since the composition of the anomalous component suggests that it is interstellar gas accelerated by the solar wind, Fisk et al. [70] have predicted that only atoms with a first ionization potential higher than hydrogen will display anomalous spectra and that the ions will be singly ionized. If the anomalous component is singly ionized, it can penetrate much more deeply into the Earth's magnetic field and may account for some of the measurements of heavy ions in the inner magnetosphere as mentioned earlier.

2.2.6.5 GCR Electrons

Although Galactic Cosmic Rays are primarily interplanetary protons and ionized heavy nuclei, electrons are also a component of GCR. Their measured intensities at energies above ~100 MeV, however, are at least 1 order of magnitude smaller than that of the protons (Fig. 41). The model for GCR electrons presented here is taken from NASA SP-8118 [20]. The integral intensity for galactic cosmic ray electrons, in units of ($m^{-2} - s^{-1} - sr^{-1}$), is given by:

$$I_{mean} = \frac{2000}{(\alpha E^6 + \beta E^3 + E^2 + \gamma)^{1/4}} + \frac{400}{E^{3/2}} \tag{33}$$

where:

$\alpha = 10^{-12}$

$\beta = 10^{-3}$

$\gamma = 6x10^4$

fluence = $\iint I \; d\Omega \; dt$

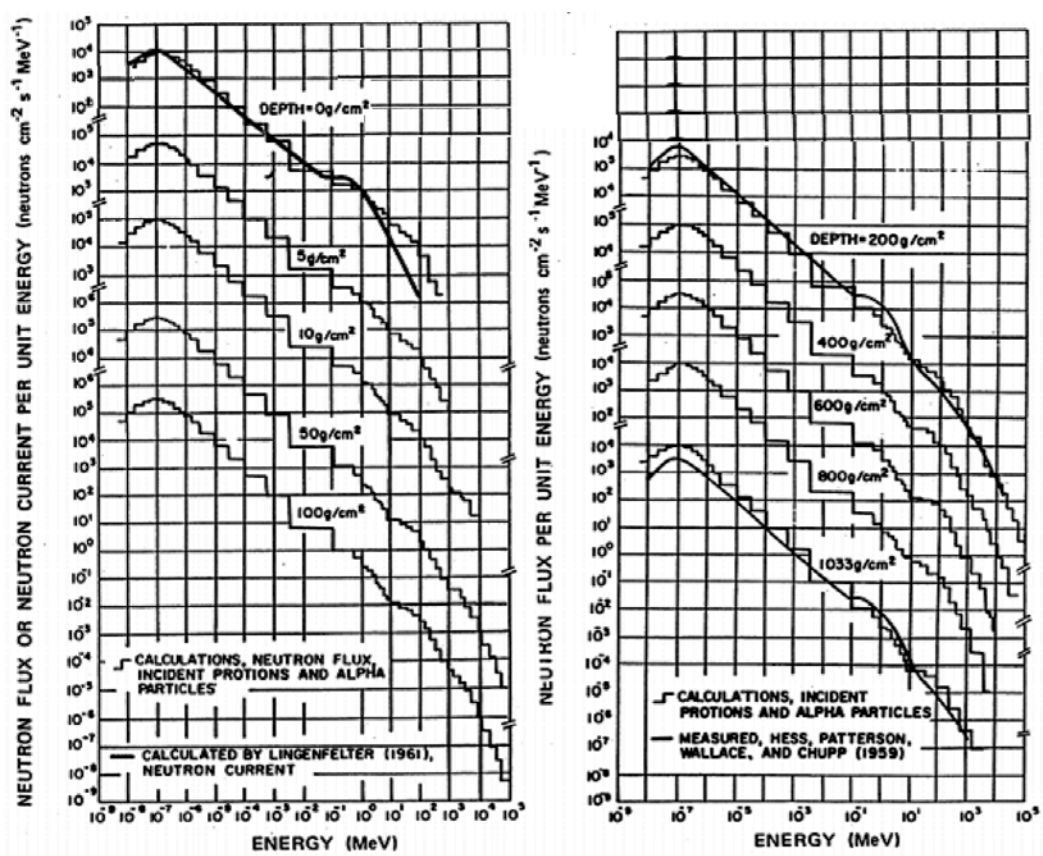

Figure 45. Neutron spectra at various depths from top of the atmosphere. The data are adjusted to solar minimum conditions at the midlatitude geomagnetic latitude of ~42° (equivalent to a vertical cutoff rigidity of 4.5 GV) [6].

2.2.7 Neutral Particle Radiation

Neutrons (at rest) typically have a half-life of 11.7 minutes before they decay into an electron, proton, and anti-neutrino. As a result, all but the most energetic solar flare neutrons (and therefore extremely small fluences) will have decayed before they can reach the Earth's orbit. Likewise, there is no primary neutron component to the intergalactic cosmic rays. The observed neutron component is, instead, associated with a secondary cosmic ray (both solar flare and intergalactic) processes. The neutrons produced by these processes are discussed below [6].

A primary Galactic Cosmic Ray (Fig. 40) incident on the Earth's atmosphere will interact with air nuclei to produce a multitude of high energy secondary cosmic rays. These in turn will interact to produce additional particles in a "nuclear cascade". The production of these secondary particles becomes significant around 55 km reaching a maximum value at ~20 km (called the Pfotzer maximum). The intensity falls off below this altitude. At high energies, the so-called "knock-on" process dominates neutron production while at lower energies, "neutron evaporation" dominates. These neutrons interact with the atmosphere to produce various radioactive isotopes such as ^{14}C. Representative differential energy spectra for neutrons at various depths in the atmosphere are presented in Fig. 45.

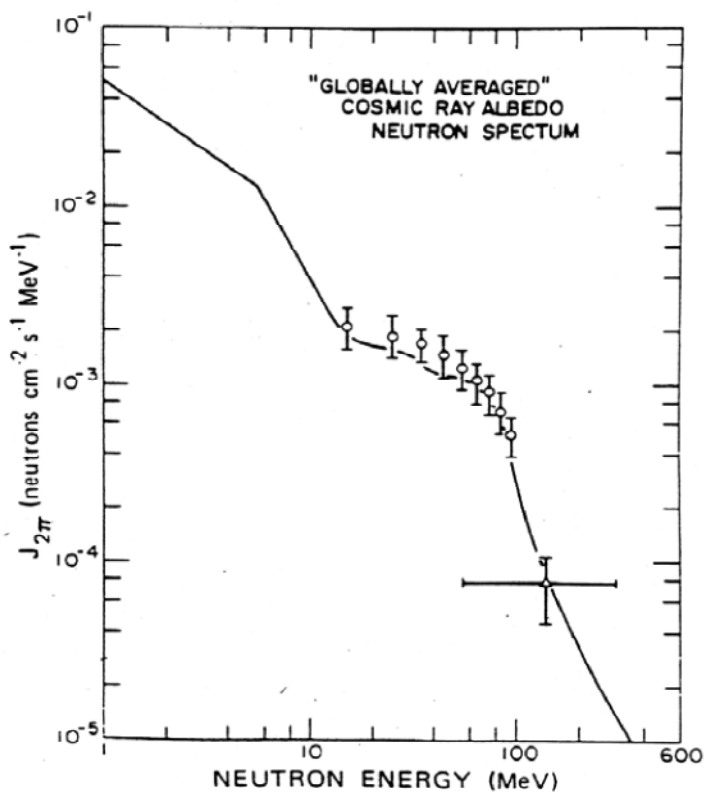

Figure 46. A model "global averaged" albedo neutron spectrum [71].

About 10% of the secondary cosmic ray neutrons escape into space. Most of these neutrons (which are not controlled by the Earth's magnetic field) will decay into electrons and protons which will be trapped in the Earth's radiation belts (these "cosmic ray albedo neutrons"-CRAN-are a major source of the high energy protons in the belts). A globally averaged albedo neutron spectrum is presented in Fig. 46. Near the Earth, there is an approximate 1:7 ratio of albedo neutrons from the equatorial atmosphere as compared with the polar atmosphere. Significant ground level neutron events are relatively rare and are normally observed in conjunction with major solar flares.

2.2.8 Nuclear Power Sources

2.2.8.1 Radioisotope Thermoelectric Generators (RTGs)

Interplanetary missions beyond the orbit of Mars typically can not efficiently utilize solar arrays—the solar energy density is too low. Rather it has become common practice for missions like Voyager, Galileo, Ulysses, and Cassini to employ RTGs. Here, as an example of the induced radiation environment typical of these systems, the Galileo RTGs will be characterized. It should be remembered, however, that this environment is very device-dependent and will need to be specified for each particular design.

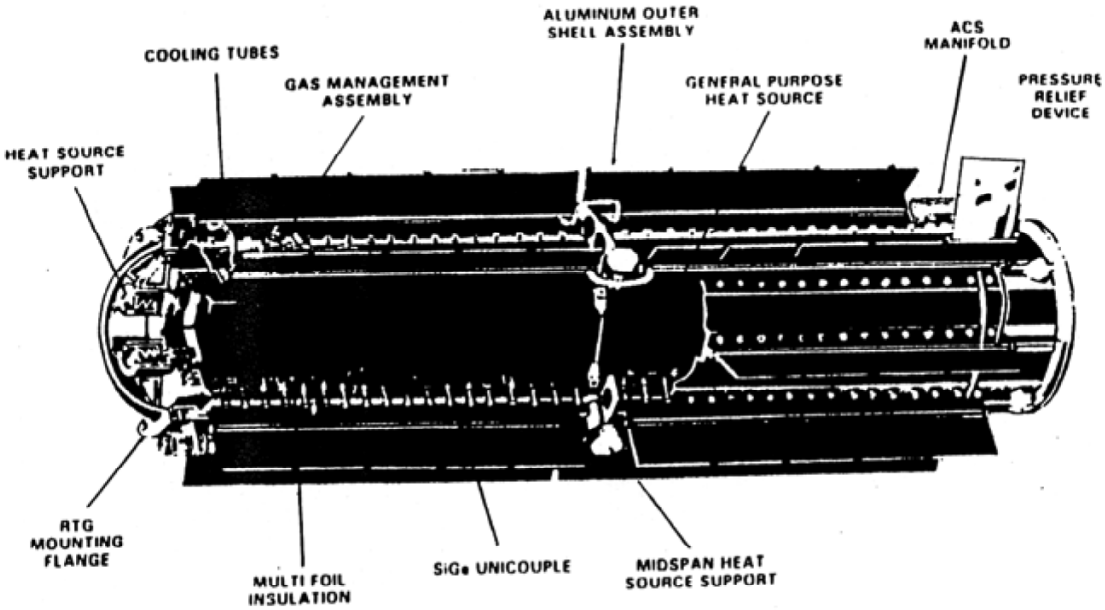

Figure 47. Illustration of the construction of a Galileo General Purpose Heat Source (GPHS) Radioisotope Thermoelectric Generator (RTG) [72, 73].

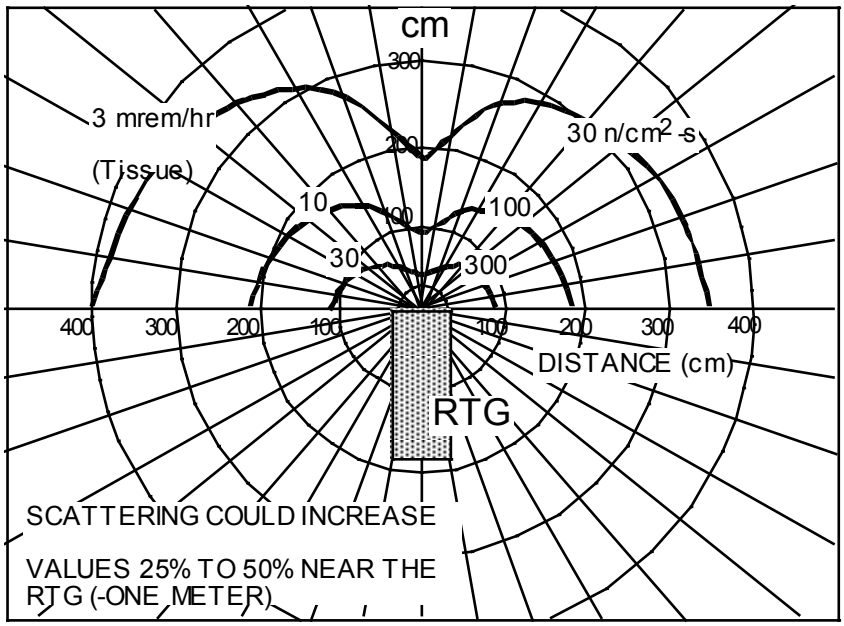

Figure 48. Neutron isodose isoflux plots for a single 4500 Watts(th) GPHS RTG (point kernel calculation) [74].

Table 10. Isotopic Composition of the Production Grade $^{238}_{94}Pu$ used in the Galileo GPHS-RTGs [72].

Plutonium Isotope	Weight Percent	Half-Life Years	Radioactivity Curies/gram Pu_xO_2
236	0.00012	2.8	476
238	81.0	87.8	15.4
239	15.2	24,000	0.054
240	2.9	6,600	0.195
241	0.8	13.0	100.4
242	0.1	370,000	0.0034

Galileo had 2 RTGs (Fig. 47). These RTGs, called General Purpose Heat Source (GPHS) RTGs, are basically large cylinders containing golf-ball sized pellets of plutonium 238 (^{238}Pu) [72-74]. The ^{238}Pu produces heat by emitting alpha particles—the heat is converted directly into electricity by electric thermocouples. Each RTG contains ~11 kg of plutonium or about 137,000 curies (1 curie represents 3.7×10^{10} radioactive disintegrations per second)--this gives an intensity of about 7,000 n/s-g at the fuel cylinder level. The fuel is in the form of pure plutonium oxide (PuO_2) with 0.7 ppm ^{236}Pu and less than 0.5% ^{232}U and ^{228}Th (Table 10 [72]). The primary radiation environments of concern are neutrons and γ-rays. Table 11 [74] tabulates the

normalized differential flux as a function of energy for both RTGs and RHUs. These normalized values must be multiplied by an absolute value that is a function of both distance and angle relative to the RTG. The absolute values, in terms of isodose-isoflux for neutrons and γ-rays, are plotted in Figs. 48 and 49 for a single GPHS RTG with 5 year old fuel (corresponding roughly to the Galileo RTGs at launch) and give absolute flux at a particular distance and angle. The radiation characteristics of the RTG plutonium fuel, because of its short half-life, change rapidly in time. This is reflected in the γ-ray values which need to be corrected for this time factor. In addition, a factor of 2 is recommended as a "worst case" design margin.

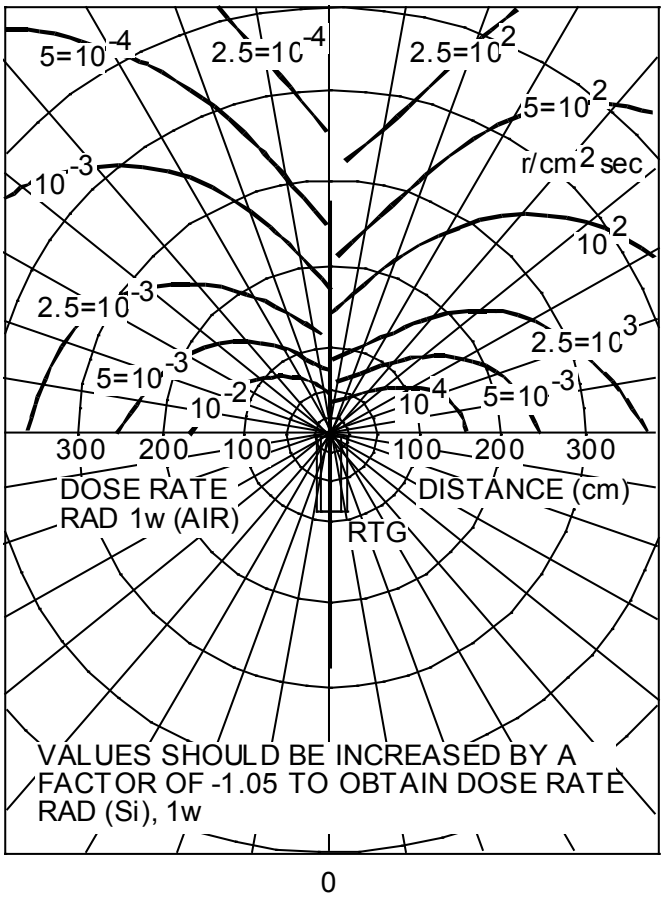

Figure 49. Gamma isodose-isoflux contours for a single 4500 Watt(th) GPHS RTG (5-year-old fuel) [74]. Values should be increased by a factor of 2.0 for the worst case. The flux will change with fuel age and should be corrected using Table 10.

2.2.8.2 Radioisotope Heater Unit (RHU)

RHUs are intended to provide localized heating within a spacecraft and minimize the use of electrical power. The Galileo design is based on a 1 W unit with approximately 34 curies (2.6 g) of plutonium fuel per unit. Each unit was ~5 years old at launch. Fig. 50 is a cutaway of a typical Galileo RHU. The PuO_2 fuel pellet is encapsulated within a clad of platinum-rhodium

alloy for fuel containment. Like the RTGs, it is assumed that the plutonium is basically pure ^{238}Pu with less that 1.2 ppm of ^{236}Pu and less than 0.5% ^{232}U and ^{228}Th. The normalized fluxes in Table 11 [74] are to be multiplied by the values in Table 12 [74] to give absolute values. These are given in terms of distance from the RHU in cm. As for the RTGs, the γ-ray values must be corrected by a time factor [74]. Again, a factor of 2 radiation design margin is recommended for a "worst case".

Table 11. Normalized Differential γ and Neutron Fluxes for the Galileo RTGs and RHUs [74]. The data are based on 1.2 ppm ^{236}Pu and a fuel age of 5 yrs. The flux will change with fuel age and should be corrected using Table 10.

Gammas		Neutrons	
Energy Width (MeV)	Normalized Number Flux in Group (/cm^2-s)	Energy Width (MeV)	Normalized Number Flux in Group (n/cm^2-s)
7.0 - 6.0	1.09 (-5)	10.0 - 8.55	9.64 (-4)
6.0 - 5.0	3.29 (-5)	8.55 - 6.66	4.59 (-3)
5.0 - 4.0	9.72 (-5)	6.66 - 5.18	9.93 (-3)
4.0 - 3.0	2.96 (-4)	5.12 - 4.46	9.66 (-3)
3.0 - 2.616	2.65 (-4)	4.46 - 4.04	1.34 (-2)
2.616 - 2.614	1.56 (-1)	4.04 - 3.14	8.73 (-2)
2.614 - 2.0	1.54 (-2)	3.14 - 2.45	1.76 (-1)
2.0 - 1.75	2.79 (-3)	2.45 - 1.91	1.57 (-1)
1.75 - 1.5	3.89 (-2)	1.91 - 1.49	1.46 (-1)
1.5 - 1.25	1.75 (-2)	1.49 - 1.16	9.76 (-2)
1.25 - 1.0	2.21 (-2)	1.16 - 0.9	7.60 (-2)
1.0 - 0.75	1.18 (-1)	0.9 - 0.702	5.87 (-2)
0.75 - 0.585	9.96 (-2)	0.702 - 0.546	4.35 (-2)
0.585 - 0.584	2.59 (-2)	0.546 - 0.331	5.45 (-2)
0.584 - 0.50	6.05 (-2)	0.331 - 0.201	2.98 (-2)
0.50 - 0.40	9.17 (-2)	0.201 - 0.122	1.66 (-2)
0.40 - 0.35	4.60 (-2)	0.122 - 4.49 (-2)	1.48 (-2)
0.35 - 0.30	4.56 (-2)	4.49 (-2) - 1.7 (-2)	3.07 (-3)
0.30 - 0.275	1.92 (-2)	1.7 (-2) - 5.55 (-4)	7.77 (-4)
0.275 - 0.239	2.41 (-2)	5.55 (-4) - 3.0 (-5)	1.17 (-6)
0.239 - 0.238	3.91 (-3)	3.0 (-5) - 3.0 (-6)	1.62 (-9)
0.238 - 0.200	3.49 (-2)	3.0 (-6) - 1.1 (-7)	4.65 (-11)
0.200 - 0.175	2.51 (-2)	1.1 (-7) - 2.5 (-8)	1.74 (-12)
0.175 - 0.153	1.70 (-2)		
0.153 - 0.152	2.86 (-2)	Integral Total	1.000
0.152 - 0.125	9.19 (-2)		
0.125 - 0.1213	9.82 (-4)		
0.1213 - 0.1211	9.41 (-6)		
0.1211 - 0.1000	1.58 (-2)		
0.1000 - 0.0099	1.18 (-3)		
0.0099 - 0.0080	2.24 (-2)		
Integral Total	1.000		

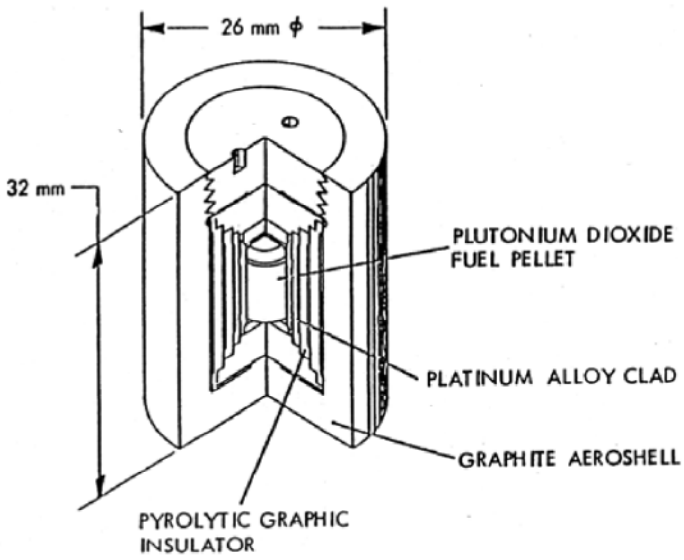

Figure 50. Schematic of a Galileo Lightweight Radioisotope Heater Unit (LHRHU) [72].

Table 12. Galileo RHU neutron and γ radiation distance variation factors to be used in conjunction with Table 11 to give absolute values of the flux, fluence, and dose as a function of distance from the RHU [74]. The γ-ray flux and dose are based on a ~5 year old fuel at launch and must be corrected by the decay rates presented in Table 10.

	Neutron		Gamma	
Distance From RHU (cm)	Peak Flux (cm^{-2} s^{-1})	Fluence (cm^{-2})	Peak Flux* (cm^{-2} s^{-1})	Dose** rad(Si)
0	6.1×10^{2}	1.6×10^{11}	4.7×10^{4}	5.3×10^{3}
2	9.5×10^{1}	2.4×10^{10}	7.3×10^{3}	8.3×10^{2}
4	4.0×10^{1}	1.0×10^{10}	2.5×10^{3}	2.9×10^{2}
6	2.4×10^{1}	6.0×10^{9}	1.5×10^{3}	1.7×10^{2}
8	1.2×10^{1}	3.0×10^{9}	1.0×10^{3}	1.1×10^{2}
10	8.1×10^{0}	2.0×10^{9}	6.4×10^{2}	7.2×10^{1}
15	3.9×10^{0}	9.8×10^{8}	3.0×10^{2}	3.4×10^{1}
20	2.3×10^{0}	5.8×10^{8}	1.8×10^{2}	2.0×10^{1}
50	3.9×10^{-1}	9.8×10^{7}	3.0×10^{1}	3.4×10^{0}

3 Shielding Effects and Interactions with Matter

From the standpoint of radiation interactions with matter, 3 "particle" families need to be considered:

1) photons primarily EUV, X-ray, and γ-rays

2) charged particles protons, electrons, and heavy ions

3) neutrons

While numerous, more exotic particles such as positrons, muons, mesons, etc. exist, these 3 families account for the vast majority of interactions of concern to the spacecraft engineer. In addition, for the impacting particles, mass, charge, and kinetic energy are the principle physical characteristics of interest whereas mass and density are the key characteristics for the target material. Here the various types of interactions will be discussed in terms of these 3 particle families. The effects of the shielding on these particles will be manifested in terms of energy deposited in a volume (dose) or the energy deposited per unit length in the target material (LET)

after traversing a specified thickness of shielding. The radiation shielding calculation necessary to determine the environment inside a spacecraft thus breaks down into a 3 step process for each particle:

1) Definition of the ambient environment.
2) Propagation of that environment through the shield and calculation of the subsequent changes in the spectrum up to the target.
3) Estimation of the total energy and/or the energy deposition rate at the target.

The first part of this course detailed the ambient environment. In this section, following an example of how radiation particles can lead to serious spacecraft anomalies, the latter two issues will be addressed. An important factor that should kept in mind when considering these issues is the importance of the cascade process to the final result. In this process, one incident particle produces many secondary particles that may be very different from the incident particle (for example, electrons may generate photons or vice versa). These secondaries in turn generate their own secondaries leading to a complex mix of many different photons and particles. This process repeats until the point of interest is reached or until all the initial particle energy is absorbed. Rather than address this process in its entirety, it will first be broken down into the individual, distinct single particle interactions. The final part of this section will describe how, given the characteristics of these individual interactions, Monte Carlo techniques can then be used to estimate the gross effects of the cascade process. In the simplest models, analytic expressions are fit to these results or to actual measurements to give estimates of the end products produced by the cascade as a function of depth in the shielding material. The reality is that the cascade process is basically probabilistic and too random to be precisely modeled analytically. However, given that the analytic fits typically give very adequate results in most cases of interest to the engineer, models based on their use will be addressed here for practical radiation shielding calculations.

3.1 Radiation-Induced Anomalies: IESD

Spacecraft currently appear to operate so reliably that radiation damage seems unlikely. Actually, there have been numerous problems in the past that range from degraded performance, repeated cycles of upset/recovery, and complete failures. The effects are generally called anomalies. With a few exceptions, spacecraft anomalies and failures have not been recorded systematically. In some cases multiple anomalies of the same type have been grouped together. Often the space environment at the time of the effect was not measured. Consequently, it is difficult or impossible to assemble a data base of the numbers of individual anomalies that have

resulted from various causes. An exception is [75] which compiled available anomaly data in a systematic way. They reported data by the number of Impact Forms, where a single form is prepared for one class of anomalies on a single spacecraft. Thus a single form may represent one or many anomalies of the same type on the spacecraft. Table 13 from their study shows that internal electrostatic discharge, surface charging, dosage, and SEUs are the principle causes of anomalies. The first of these, internal electrostatic discharge (IESD), is caused by the build-up of high energy electrons, which can easily penetrate spacecraft shielding and deposit in dielectrics or on isolated conductors. When the electric field resulting from the build-up of charge exceeds the breakdown strength of the dielectric (typically $\sim 10^5$ V/cm) or the particular geometric configuration, a potentially damaging discharge can occur.

Table 13. Distribution (number of forms) of reported anomalies by diagnosis [75].

Diagnosis	**Number of Forms**
ESD - Internal Charging	74
ESD - Surface Charging	59
ESD - Uncategorized	28
Surface Charging	1
Total ESD & Charging	**162**
SEU - Cosmic Ray	15
SEU - Solar Particle Event	9
SEU - South Atlantic Anomaly	20
SEU - Uncategorized	41
Total SEU	**85**
Solar Array - Solar Proton Event	9
Total Radiation Dose	3
Materials Damage	3
South Atlantic Anomaly	1
Total Radiation Damage	**16**
Micrometeorid/Debris Impact	10
Solar Proton Event - Uncategorized	9
Magnetic Field Variability	5
Plasma Effects	4
Atomic Oxygen Erosion	1
Atmospheric Drag	1
Sunlight	1
IR background	1
Ionospheric Scintillation	1
Energetic Electrons	1
Other	2
Total Miscellaneous	**36**

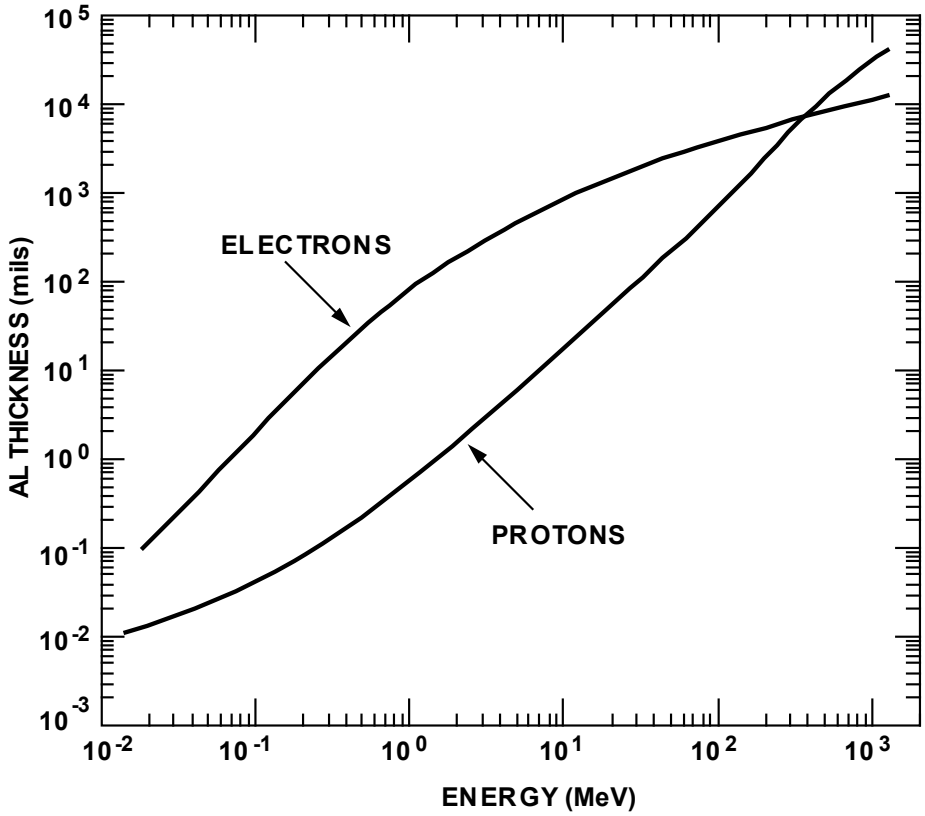

Figure 51. Mean penetration range of electrons and protons into Aluminum versus energy. Note that an ~1-2 MeV electron penetrates ~100 mils while it takes a 30-40 MeV proton to penetrate a similar depth.

Fig. 51, which plots the mean penetration range into aluminum for electrons and protons, illustrates the basic physical process that lead to IESD—1-2 MeV electrons can easily penetrate a 100 mils of aluminum shielding (a typical spacecraft radiation shielding thickness). In contrast, it takes a 20-30 MeV proton to penetrate the same thickness of shielding. As the flux of electrons with energies of 1-2 MeV exceeds the proton flux above 20-30 MeV, the electron environment can rapidly build-up charge. Fig. 52 plots the occurrences of 6 upsets on a star scanner for a spacecraft at geosynchronous orbit. Subsequent analysis of the >3 MeV electron fluxes as measured by the GOES spacecraft also at geosynchronous orbit shows that every one of these upsets was associated with an enhanced flux of these particles. The upsets are thus believed to be caused by IESD.

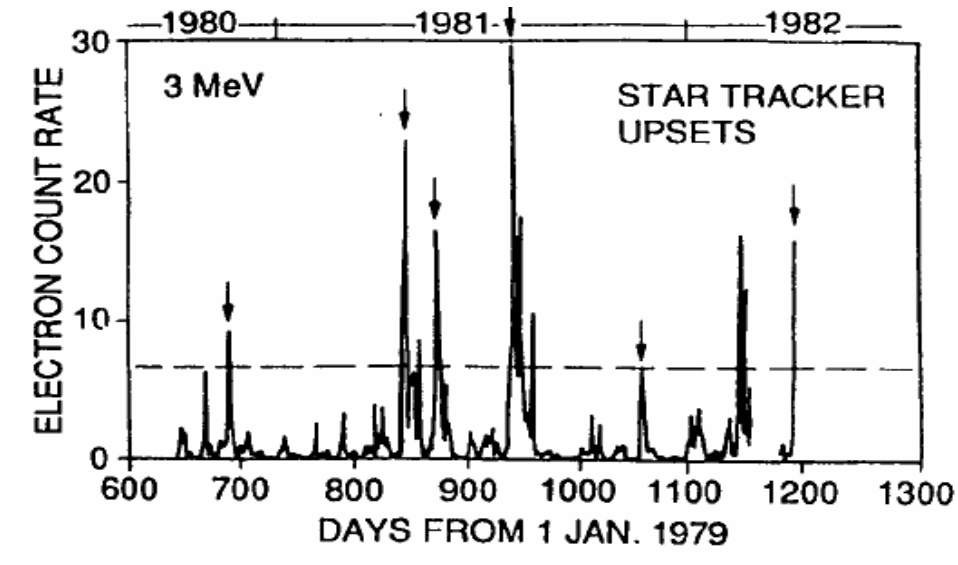

Figure 52. 3 MeV electron count rates at geosynchronous orbit versus day of year. Also shown are start tracker upsets for another geosynchronous spacecraft versus day of year. Note the correlation between upsets and high energy electron fluxes.

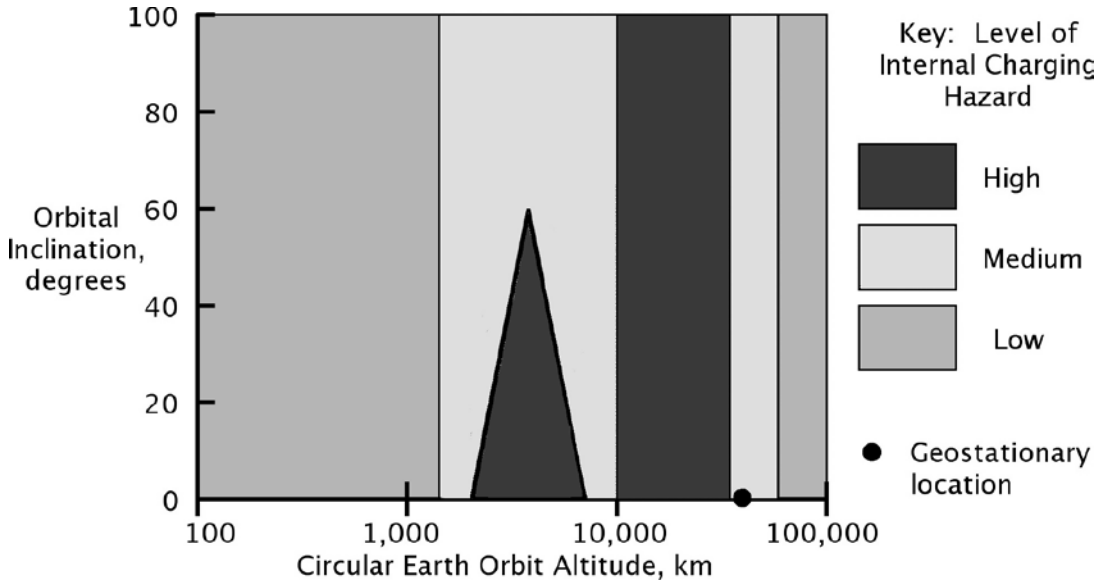

Figure 53. Earth regimes of concern for on-orbit internal electrostatic charging/discharging hazards for spacecraft with circular orbits.

Fig. 53 provides a schematic map by orbit (as defined for a circular orbit altitude and inclination) of the regions of concern for IESD. In particular, the inner and outer electron belts are of special concern. As a rule of thumb, a fluence of 10^{10} electrons/cm^2 or greater in a 10 hour period or less appears to be a critical level for IESD [76].

3.2 Single Particle Interactions

As illustrated in the previous example for electrons, high energy particle interactions with matter can lead to serious spacecraft damage. The study of the interactions of a single high energy particle such as a photon, neutron, or charged particle with matter forms a major sub-division of the physical sciences. Rather than present a detailed quantitative review of each of these interactions, a qualitative description will presented for each of the main interactions. The reader is referred to detailed quantitative reviews of each of the processes such as may be found in Refs. [1] and [77]. In most practical cases, however, the results presented here should suffice for actual computations as the complex equations modeling the processes are normally pre-coded in the computers codes available for carrying out shielding calculations.

3.2.1 Photon Interactions

Photons, which propagate at the speed of light and have no charge or rest mass, interact primarily through the photoelectric effect, Compton scattering, and pair production. These interactions all generate free electrons. Consider first the photoelectron process, the probability of which decreases with increasing photon energy and increases with Z. In the photoelectron process, the photon is completely absorbed by the emitted (typically) outer shell electron. In one case, however, subsequent interactions are possible—that is, if the photon is energetic enough to emit K-shell electrons (inner shell electrons), then this process will dominate ~80% of the time over the emission of outer shell electrons. When an L-shell (or outer shell) electron subsequently drops down to fill the K-shell vacancy, it can emit either an additional X-ray or a low energy Auger electron from the L-shell (dependent on the Z of the material). In Compton scattering, the incident photon is not completely absorbed as the photon is of much greater energy than the atomic electron binding energy. Part of the photon energy goes to scattering the atomic electron (called a Compton electron) and the rest into a scattered, lower energy photon. Pair production takes place for photons at energies of 1.02 MeV or higher. A photon of this energy will be completely absorbed by a high-Z material. A positron-electron pair will then be formed. Figure 54 [78] compares the ranges over which each of the three interactions dominate as functions of Z and energy. For reference, in silicon, the photoelectron effect dominates at energies <50 keV, pair production for energies >20 MeV, and Compton scattering at intermediate energies. The products of these interactions (electrons, photons, and positrons) can of course further interact with the target material producing a complex cascade of electrons and photons.

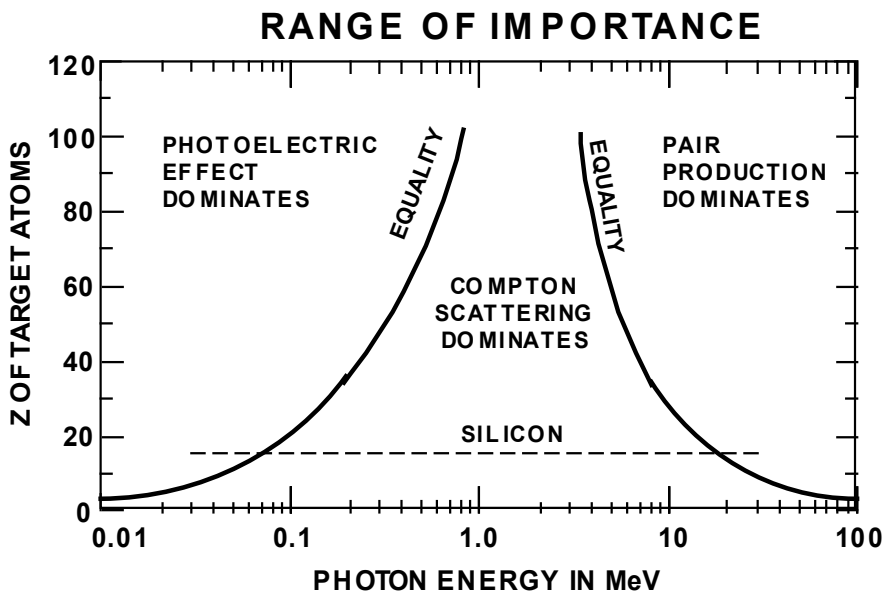

Figure 54. Illustration of the relative importance of the three photon interactions as a function of Z and photon energy. The solid lines correspond to equal interaction cross sections for the neighboring effects. The dashed line illustrates the situation for photon interactions with silicon [78].

3.2.2 Charged Particle Interactions

Charged particles interact with matter primarily in two ways: Rutherford scattering and nuclear interactions. Rutherford (or Coulomb) scattering, in which the charged particle interacts with the electric field of the target atom, typically dominates. It results in both excitation and ionization of atomic electrons and can, for sufficiently energetic impacts, transfer enough energy to displace atoms within the lattice structure. As an example, for electrons, a minimum energy of ~150 KeV is required to cause displacement in silicon while only 100 eV is required for protons. Nuclear interactions, where the impacting particle actually interacts with the atomic nucleus, can result in elastic or inelastic scattering and transmutation (through fusion or fission). As an example, a nucleus can absorb a proton and emit an alpha particle. This process, also called spallation, and the recoil atoms that result from displacement can transform a relatively benign proton environment into a SEU-causing heavy ion environment as the heavy ions have much larger LETs compared with the protons. Also, long term exposure to the space radiation environment can, through transmutation, lead to making the spacecraft material itself radioactive.

One quantitative measure of the interaction of a high energy particle with matter is stopping power or energy loss per unit length in a given material. As an example, low energy electrons (~10 KeV) primarily cause ionization. The amount of energy deposited by the latter and protons in producing ionization can be determined from stopping power tables (electrons: Berger and Seltzer [79]; protons: Janni [80, 81]). Stopping power is essential in calculating the

Heinrich flux necessary for most SEU calculations (see later). Stopping power (or LET) in terms of MeV-cm^2/g was given in Fig. 4 for electrons, protons, and various heavy ions in silicon [3].

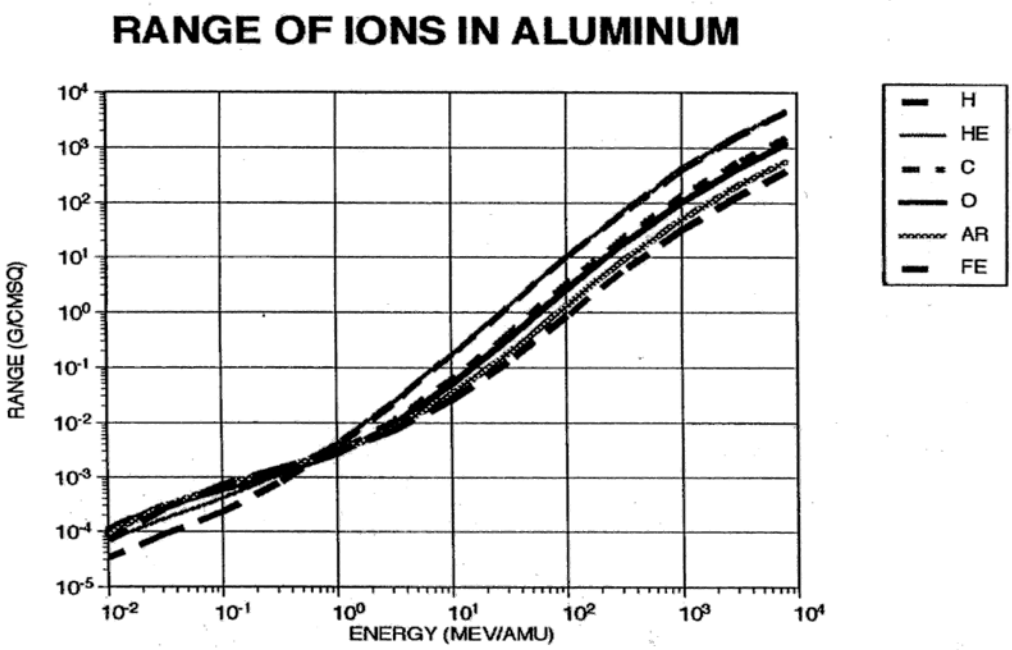

Figure 55. Ion range versus energy in [8] for H, He, C, O, Ar, Fe, and electrons. The range is in units of g-cm^2 and the energy in MeV/AMU.

A second quantitative measure of high energy particle interactions closely related to stopping power is the mean penetration depth/range a particle of a given energy can penetrate. This depth can be used to roughly estimate the minimum cut-off energy for a given thickness of spacecraft shielding and hence its effectiveness. Fig. 51 compares the mean penetration depth of electrons and protons in aluminum for different energies (the range of heavier ions in Al are presented in Fig. 55). As discussed earlier for IESD, an electron at 1 MeV penetrates over 100 times more shielding (~0.2 cm) than a 1 MeV proton (~0.0015 cm). Similarly, it takes a ~20 MeV proton to penetrate the same depth as a 1 MeV electron. As ~0.1-0.2 cm (40–80 mils) is a typical shielding level, it is common to compare the integral dose for E $\geq$ 1 MeV electrons with E $\geq$ 10-20 MeV protons as these are the primary contributors to the radiation environment behind the spacecraft shield.

3.2.3 Neutron Interactions

Neutron interactions with matter can result in elastic scattering, inelastic scattering, and nuclear transmutation. In elastic scattering, the neutron is not captured but transfers some of its energy to the target atom which can be displaced from its lattice position. It occurs only if the incident neutron has more energy than required for displacement—typically >25 eV. The target

atom, referred to as a primary recoil or knock-on, can in turn cause ionization or further displacement damage. In inelastic scattering, the neutron is captured by the nucleus followed by emission of a lower energy neutron. The kinetic energy lost in the process can result in displacement or can excite the atomic nucleus which returns to ground state by emitting a γ-ray. In transmutation, the capture of the neutron can change the atomic isotope, cause fission, or cause the emission of another particle such as a proton or alpha particle. For silicon, the dominate process is displacement and ionization for neutrons with energy ~1 MeV or higher (see Figure 3 which plots relative neutron displacement damage versus energy). The effects of neutron dose are typically not considered in radiation calculations except for the prompt nuclear environment or for evaluating the results of ground testing.

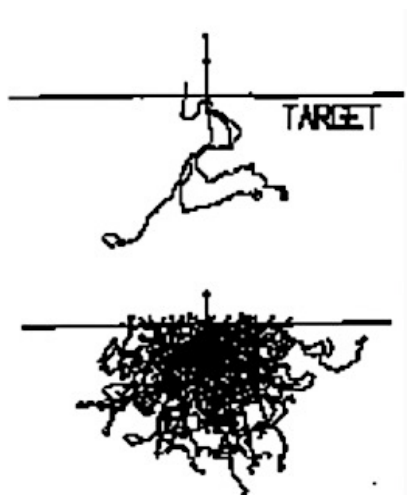

Figure 56. (Top) Computer plot showing five electron trajectories in a Cu target with a 20 keV incident beam normal to the surface [82, 83]. (Bottom) Monte Carlo results for 100 electron trajectories in a Cu an infinitely thick target with 20 keV incident electron energy [82, 83].

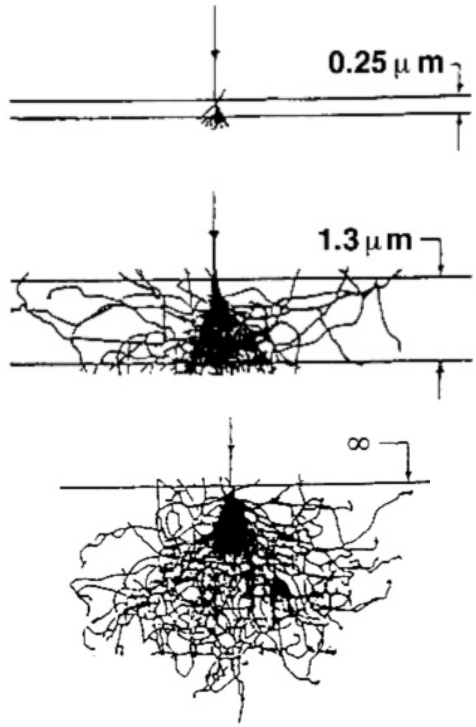

Figure 57. Effect of varying target thickness; electron trajectories in an Al targets of thickness 0.25 μm (top), 1.3 μm (center), and infinity (bottom), for an incident electron energy of 20 keV [82, 83].

3.3 Modeling The Effects Of Shielding

The preceding section has briefly described the basic interactions between single particles and matter. If the detailed evolution of a particle passing through matter is followed, the interaction of the particle with shielding becomes increasingly complex as each interaction gives rise to a cascade of by-products. Fortunately, as each interaction disperses the energy into more by-products, a point is reached where the by-products and the original incident particle (if it still exists) no longer have sufficient energy to excite further interactions—the process has a finite conclusion. Although it is common practice using Monte Carlo techniques to model the detailed passage of a particle through shielding, the computer codes that accomplish this can require super computers or take many hours to carry out the calculations. As a consequence, it is common to run the detailed codes only for a range of variables and then use this information to derive analytic fits to the end products of the multiple particle interactions that are created following a single particle impact. The effects of these by-products are then approximated roughly in terms of displacement damage, energy deposition, or ionization (or electron-hole creation). It is normally these algorithms, not the detailed computations, that are used to actually model radiation effects.

As a specific example of the Monte Carlo results, consider electrons. Electrons are particularly easily scattered in a material. Rather than passing through the material, they and the secondary electrons they generate are scattered into the material. This behavior is illustrated in Fig. 56 which is a computer simulation (Monte Carlo) of the trajectories of electrons impacting on an "infinitely thick" copper target [82, 83]—note that many of the electrons are actually scattered back out of the surface of the material. This behavior becomes ever more complex as the thickness of the shield decreases as illustrated in Fig. 57 [82, 83]. It is readily apparent in these Monte Carlo simulations that the dose is very dependent on the shape (or thickness) of the shield. This scattering of the electrons and their by-products by the shielding means that the details of geometry of the shielding must be considered in any radiation calculations.

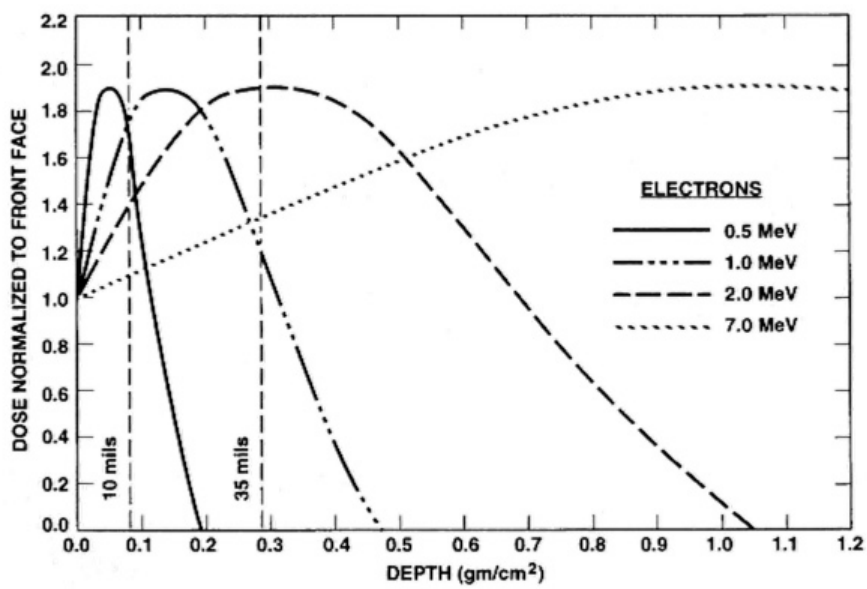

Figure 58. Electron dose as a function of depth for CaFMn TLDs [84]. The dosage is normalized to 1 at the front face.

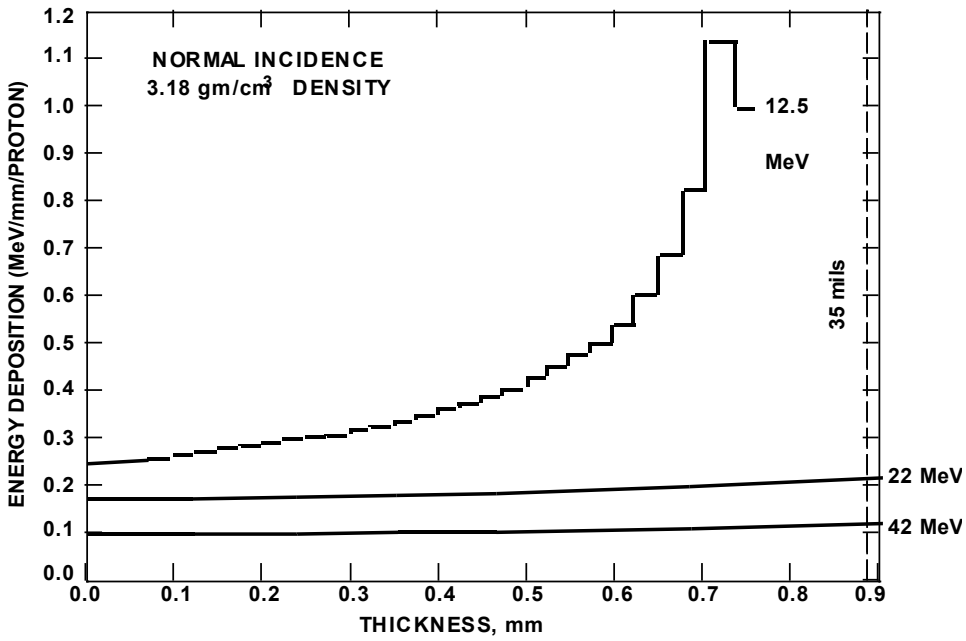

Figure 59. Proton energy deposition (MeV/mm-proton) as a function of depth for CaF_2 (density of 3.18 g/cm^3) [85].

Analytic expressions (as an example of this for electrons, see Jordon [86]) have been fit to the results of Monte Carlo calculations (Figs. 56 and 57) and to actual measurements for electrons, protons, heavy ions, neutrons, and photons. Specific characteristics, such as energy deposition, ionization, flux (both forward and back-scattered), dose, etc., can then be predicted as functions of shielding thickness or material. Fig. 58 [84] illustrates this effect for one characteristic—the electron dose versus distance into the shielding material as the incident electron energy is increased. Here the region over which the electron deposits it energy is smeared out along track. Contrast this with Fig. 59 [85] for a proton—a high energy ion deposits its energy primarily near the end of its track. This difference in energy deposition with shielding thickness is often used in designing solid state particle detectors capable of discriminating between high energy electrons and protons. It also must be kept in mind when designing shielding as too much shielding can actually cause cosmic rays of a particular energy to deposit most of that energy at a specific point in a device rather than passing through it. Families of similar parametric curves have been developed that allow rapid calculations of the effects of shielding (the lengthy Monte Carlo calculations are, however, often retained in detailed shielding studies).

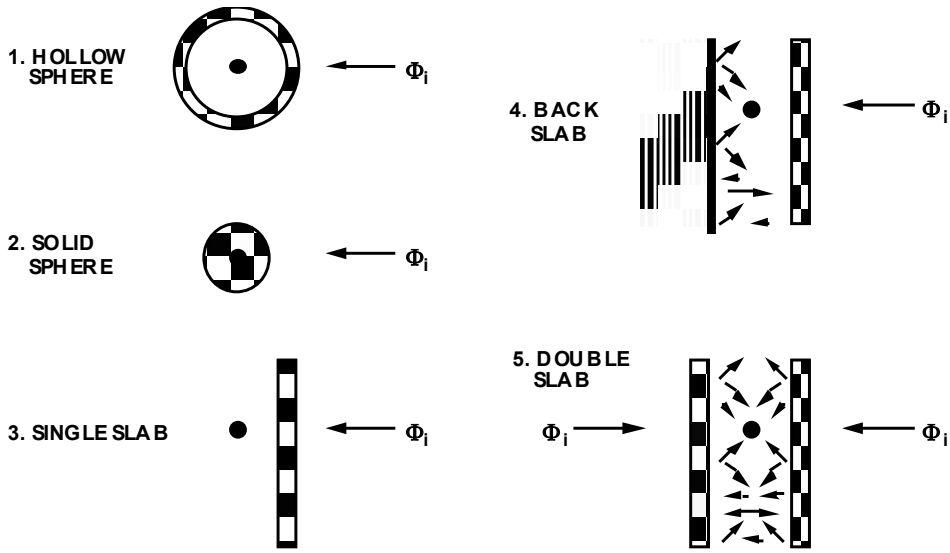

Figure 60. 5 shielding configurations considered in the NOVICE code [87] for calculating dosage. Note that examples 3 and 4 are doubled by the code.

Referring back to the method for computing dose described in Section 1, that procedure repeated for many different angles and particles gives the total dose inside a 3-dimensional volume. The final dose is basically independent of the shape or size of the test point and is only a function of the density of the material. In actual dosage calculations, however, because of the various effects of shielding on the energy deposition, 5 shielding geometries are typically considered. These 5 geometries, as adapted from the descriptions provided by T. Jordan for his "NOVICE" shielding code [87] and illustrated in Fig. 60, are:

1.) Spherical Shell: As the name implies, this configuration represents a hollow sphere of equal thickness in every direction from the dose site which is at the center of the sphere (note: the radius of the sphere void can be shown to be unimportant for large distances). The dosage tends to be lower than for a solid sphere of the same shield thickness. This case resembles a point inside a typical hollow spacecraft.

2.) Sphere: The shield is assumed to be uniformly distributed around the dose site with no gap between the shielding material and the dose site (i.e., a point at the center of a solid metal sphere). As scattering takes place relatively close to the dose site, little scattered flux is lost. This case resembles a "spot shield" configuration.

3.) Slab (or 2*Slab): A single slab is assumed to be an infinite 2-dimensional surface. Ideally, particles enter from one side and irradiate the dose site. That is the basic "Single Slab" configuration which assumes no back scattering of electrons and no flux from behind (i.e., infinite back shield)—this approximates the actual case for high energy protons and heavy ions. To estimate the omnidirectional flux for a part between 2 shield planes without back scattering from a second surface, this value is typically doubled (in the NOVICE code [87], this is called the 2*Slab case; see Double Slab case also).

4.) Back Slab: This configuration is similar to the Slab in that the dose site is again assumed to be backed up by an infinite slab. As before, the flux only comes in from one side but now particles can be reflected or scattered back. This often nearly doubles the incident flux for electrons.

5.) Double Slab: Here there are 2 identical thin shields-one on each side. In this configuration, the flux is assumed to come from both sides and back scattering from each is included. This geometry would resemble the case of a flat solar array panel extending out from the spacecraft in a wing configuration.

Which configuration to use depends greatly on the geometry of the spacecraft component being modeled. The spherical shell is often used as the baseline representation as it more closely resembles the shielding around typical circuit boards in the spacecraft interior.

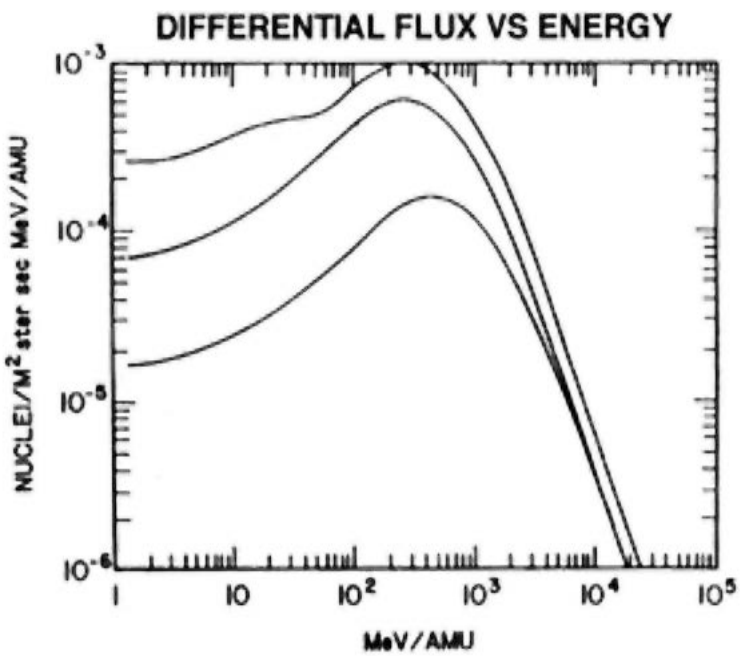

Figure 61. Shielding attenuated cosmic ray differential iron spectra for 3 cases: 90% worst case (upper), solar minimum (middle), and solar maximum (lower) [3]. These spectra are for 1 AU (no magnetospheric shielding) and behind 25 mils of aluminum shielding.

Consider next the detailed steps involved in determining the other radiation quantity of interest, the Heinrich curve for a heavy ion. As outlined in Adams [3] for the CREME code, the steps are:

1) The first step is to define the particle spectrum of interest at the surface of the critical volume. In this example, consider the ambient environment for GCR iron at the surface of a

spacecraft. Three interplanetary iron spectra (90% worst case—highest, solar minimum—middle, and solar maximum—lower) are plotted in Fig. 2 [3]. Call this the differential spectrum $f(E)$.

2) The attenuation of a high energy ion by shielding can be approximated by:

$$f'(E') = f(E)\left[\frac{S(E)}{S(E')}\right]e^{-\sigma\tau} \tag{34}$$

where:

$$\sigma = \frac{5x10^{-26}\eta\left(A^{1/3} + 27^{1/3} - 0.4\right)^2}{27} \tag{35}$$

f'=Differential spectrum inside shielding

τ =thickness of shielding

E'=Energy inside spacecraft (=$R^{-1}\{R(E)-\tau\}$)

R=Range through shield of ion of energy E (See Fig. 55 for Fe in Al)

R^{-1} =Inverse function of R(E)

S=Stopping power of ion in target material (See Figure 4 for Fe in Si)

A=Atomic mass of ion

η=Avogadro's number

Figure 61 shows the results of this calculation for iron behind 25 mils of aluminum shielding [3] for the three spectra in Fig. 2.

3) Next, the energy loss versus distance (dE/dx) curve for the incident particle species in the material of interest is determined. The -dE/dx curve for Fe in Si is plotted in Fig. 4. Define this curve as h(L) where L is the LET of the particle.

4) The incident (internal) differential particle spectrum f'(E') is converted to the differential Heinrich spectrum h(L) by:

$$h(L) = f'(E')\left[\frac{dE'}{dL}\right] \tag{36}$$

This result for Fe impacting Si is presented in Fig. 62 (the spikes at the ends of the curve are numeric and result from dL/dE going to 0 which implies that dE/dL goes to ∞–a careful analytic evaluation would give a finite value).

5) Eq. 36 is integrated over L to give the integral Heinrich LET curve, F_H (note: this is equivalent to Eq. 12):

$$F_H(L) = \int_L^{\infty} h(L)dL \tag{37}$$

The final results are plotted in Fig. 63. These curves, called Heinrich curves, are the type of information normally required for SEU calculations. In the case of GCR, this curve would be calculated for all the GCR and summed to give a final result (see next section for an example).

The radiation dose or flux/fluence that reaches a specified point can be computed by several different methods. The first uses the dose depth curves like those of Figs. 64 and 65 and simple ray tracing models to estimate the total mass as a function of direction. The dose corresponding to each mass/direction is then weighted by the solid angle to give the weighted dose at the location. Examples of these codes are: FASTRAD (http://trad.fr/), MEVDP (http://www-rsicc.ornl.gov/), and "SIGMA" (an option in Novice: tj@empc.com). These programs allow rapid computation of the dose while varying the mass and structural design. As a result they are very useful for trade studies.

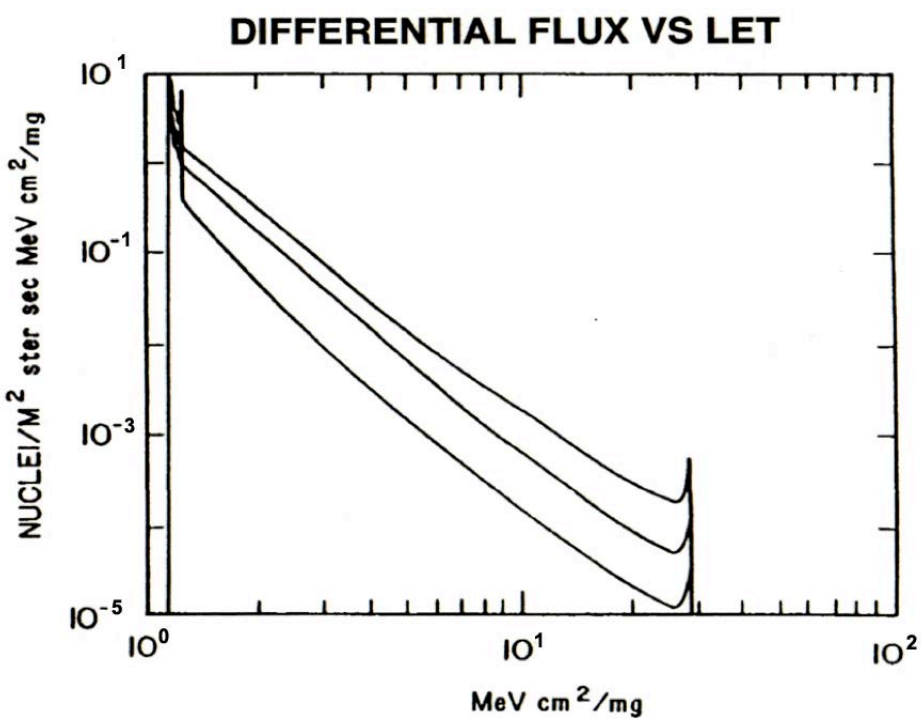

Figure 62. The same three cases as in Figs. 61, but now the spectra have been transformed into differential LET spectra [3].

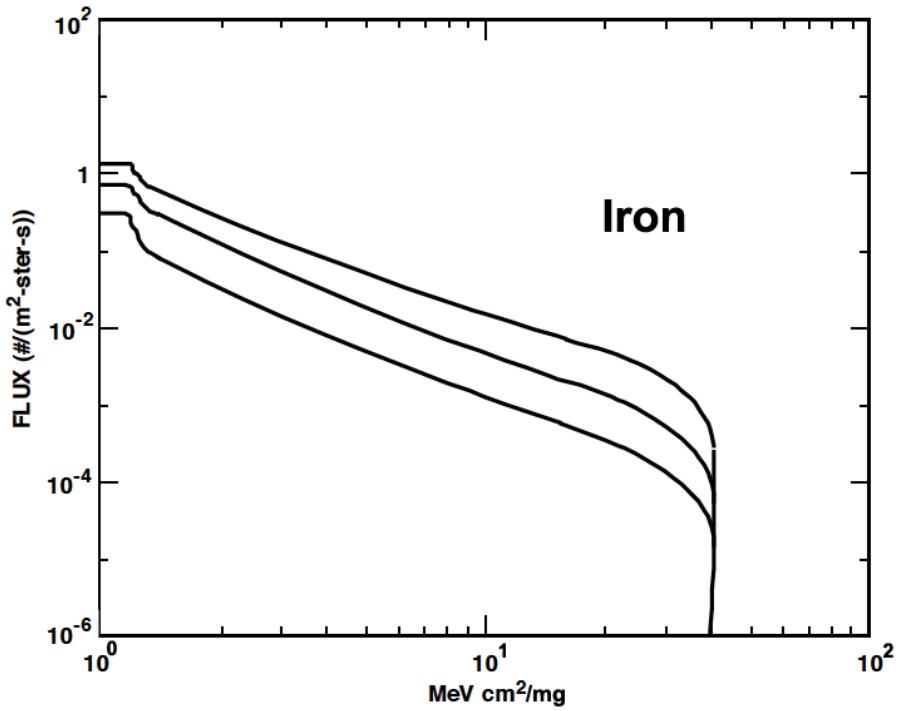

Figure 63. The same three cases as in Figs. 61 and 62, but now the spectra of Fig. 62 have been integrated to give the integral LET spectra (Heinrich curves) for Fe [3]. (Note: copy of Fig. 5.)

Ray tracing codes do not, however, explicitly include the detailed physics associated with particle transport such as all the possible secondary particles that can be scattered into the location. The other class of codes are deterministic or Monte Carlo transport codes. Especially in Monte Carlo codes, they track individual particles taking into account all the physics of the particle interactions. Typically millions of particles are tracked with those that intersect the point of interest being recorded until sufficient statistics are compiled. These codes typically include all the detailed physics but can take a long time to run for a specific point to accumulate sufficient statistics (literally millions of particles may need to be tracked). These codes can be used to evaluate: total ionizing dose, displacement damage dose, single event effects, internal charging, secondary particle environments behind shield, and carrying out particle detector simulations. Typical examples are CREME96, TRIM, ITS3.0 (TIGER), NOVICE, MCNP(X), and Geant4. These codes and their features are tabulated in Tables 14 and 15. Except for NOVICE, these codes are "outside-in". That is, they track particles forward in time to the point(s) of interest. NOVICE tracks particles "inside-out"—it follows particles backward from the point of interest to the external environment. This significantly speeds up the simulation process.

Table 14. Features of Common Radiation Transport Codes. Radiation transport codes not covered: EGS4, CEPXS, HZETRN, SpaceRad, PENELOPE, FLUKA, MARS, etc.

Code	Primary Application	Comments
CREME96	Heavy Ion LET Spectra	Limited to spherical shell aluminum shielding
TRIM	Proton or heavy ion beam simulation	1-dimensional Only Coulomb interaction
ITS3.0 (TIGER)	Electron or photon beam simulation for dose and charging rate profiles	Excellent electron/photon physics Extensively benchmarked
NOVICE	Spacecraft level shielding analysis	"Adjoint" (fast for space environment application) No secondary neutrons from photonuclear reactions
MCNP(X)	Full 3-D detector/sensor simulation Transients calculation	Good physics and extensive development history Slow for space application
Geant4	Full 3-D detector/sensor simulation Transients calculation	Good physics Many Geant4-based "tools" are available Slow for space application

To summarize, there are many different techniques for estimating the radiation environment behind a spacecraft shield. To limit the amount of computer time required, the "exact" Monte Carlo formalism is often replaced by analytic approximations (called "kernels") when performing the particle transport and shielding calculations. Specifically, tabulated attenuation data, using Monte Carlo techniques, are prepared for various shield geometries (i.e., the slab, spherical shell, and solid sphere geometries illustrated in Fig. 60). Given a 3-D model of the shielding mass and geometry (or a 1-D configuration, depending on the desired level of accuracy), the equivalent shielding at a point as a function of angle and path length is calculated. The input spectra from the environment (neutrons, γ-rays, photons, electrons, positrons, protons, heavy ions, alphas, GCR, etc.) are convolved with this equivalent shielding to calculate the dose (or Heinrich flux) as a function of energy (or LET) and angle. Secondary and Bremsstrahlung particle effects also normally need to be included, particularly for thick shielding. For a more detailed treatment of these interactions see Refs. [1], [88], [89], [77], [90], and others. Computer codes for carrying out detailed transport and shielding calculations are available from the Oak Ridge National Laboratory's Radiation Shielding Information Center (RSIC) and various commercial vendors and government laboratories. (The RSIC address is ORNL, Box X, Oak Ridge, Tenn. 37831-6362, Telephone 615-574-6176 or FTS 624-6176.)

Table 15. Characteristics of Radiation Transport Codes. Radiation transport codes not covered: EGS4, CEPXS, HZETRN, SpaceRad, PENELOPE, FLUKA, MARS, etc.

	Electron	Photon	Proton	Neutron	Heavy Ion
CREME96 creme96.nrl.navy.mil			√		√
TRIM www.srim.org			√		√
ITS3.0 www-rsicc.ornl.gov	√	√			
NOVICE tj@empc.com	√	√	√		√
MCNP(X) mcnpx.lanl.gov	√	√	√	√	√
Geant4 geant4.web.cern.ch/geant4/	√	√	√	√	√

4 Radiation Environment Estimates

In this section, we will complete the analysis of the spacecraft radiation environment by combining our knowledge of the ambient radiation environment with the transport/shielding process to examine several practical case studies. These will be, in order, a detailed analysis of the radiation dose environment to be expected for a lunar transfer mission (Clementine), a mission to Mars, an analysis of the intense radiation environment at Jupiter for the Galileo mission, and a comparison of the effects of shielding and orbit on solar flare and GCR Heinrich fluxes. Each of these case studies will illustrate the basic steps required in carrying out a thorough analysis of the radiation environment inside a spacecraft—the purpose of this section.

4.1 Example–The Clementine Program

As an illustration of the process of estimating the radiation dose environment within a satellite, consider the case of the Clementine spacecraft lunar transfer orbit sequence. Clementine was a DOD/NASA mission designed to map the Moon and an Earth orbit-crossing asteroid. It tested the effects of the radiation environment on a number of unique, advanced microelectronic systems. The Clementine also left behind its lunar transfer stage in a unique, highly elliptical orbit. This interstage and the Clementine were both been instrumented with radiation dosage and SEU detectors. In addition, each carried samples of advanced

microelectronics components for direct exposure to the radiation environment. A detailed radiation environment prediction was required to allow the identification of radiation sensitive parts and to determine appropriate replacement parts or provide enhanced protective measures. It was also desired to predict the performance of the systems and test components in the radiation environment. These are all typical requirements for a space mission and illustrate the wide range of potential applications for radiation calculations.

4.1.1 AE8/AP8 Radiation Dosage Results

As has been discussed, currently the most often used trapped radiation environment models are the AE8 (electron) and AP8 (proton) solar maximum (or active) and solar minimum (or quiet) trapped radiation models. These models give dosage results that, when averaged over mission lifetimes of the order of the solar cycle, are typically within a factor of 2 of the actual measured dosages. Unfortunately, for time periods shorter than about 5 years, the statistical variations can be great (approaching factors of $10^{\pm 1}$ to $10^{\pm 2}$ for missions of less than a year, Figure 26). Even so, they have formed the basis of almost all trapped radiation calculations since the late 60's. With a properly defined radiation design margin (RDM), their predictions are useful in evaluating a spacecraft radiation hardness design. (As discussed earlier, the AE-9/AP-9 models will shortly be issued and will supersede the AE8/AP8 models.)

As has been described, the process of calculating the dosage at the interior of a spacecraft in Earth orbit is straightforward but time consuming. First, the B and L coordinates of the spacecraft are estimated from the orbit. The particle integral flux as a function of energy is then computed in terms of B and L from the AE8/AP8 models. The resulting spectra are summed over mission time to give the total integral fluence spectrum in terms of energy and particle species. These spectra, by species, are then used as input to a transport or shielding code (T. Jordan's "NOVICE" code, a commercially available software package, was used here [87]) which computes the total energy deposited at a point as a function of shield thickness, shield composition, and geometry. Typically, for dosage calculations to be used in a first order estimate of the internal radiation environment, aluminum for the shield and silicon for the dose site are assumed for composition. Geometrical considerations become particularly important for electrons as the electrons can be easily scattered or reflected within the material. As described in earlier sections, several different geometries are usually assumed. Here, 5 geometries are considered (see Fig. 60):

1.) Spherical Shell

2.) Sphere

3.) 2*Slab

4.) Back Slab

5.) Dubl Slab (Double Slab)

In the NOVICE calculations, the single slab is assumed to be an infinite 2-dimensional surface (Fig. 60) with an infinite back shield–no radiation comes from behind the shield and none is reflected back. For comparison purposes, the code doubles this value (hence, "2*Slab") so that the results can be used to estimate the omnidirectional flux for a part between 2 slabs without scattering (see Dubl Slab case). Unless stated otherwise, the spherical shell geometry will be assumed as the baseline representation as it more closely resembles the shielding around typical circuit boards in the Clementine interior.

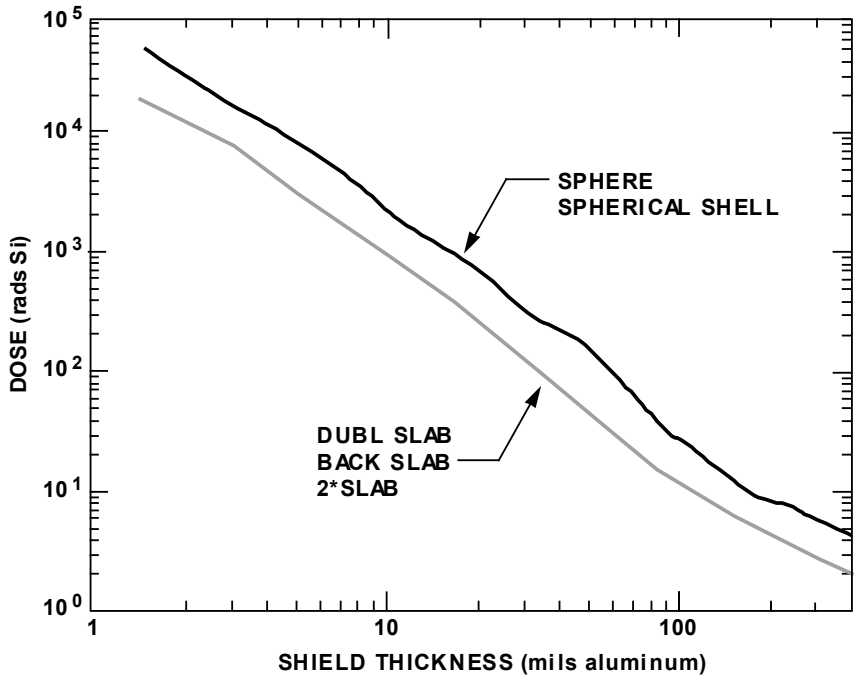

Figure 64. Radiation dosage from the trapped proton environment (AP8) for solar-quiet conditions and for the first Earth-Moon Transfer Orbit {1994/01/30(07:00)--1994/02/09(12:00)}.

A set of orbital data for the portions of the Clementine orbit within 11 Earth radii was assembled. The Clementine orbit was divided up into 6 segments. These are:

1.) 1994/01/24 (01:48) -- 1994/01/26 (01:00) Initial Parking Orbit

2.) 1994/01/26 (01:00) -- 1994/01/30 (06:44) Earth-Moon Transfer Injection

3.) 1994/01/30 (07:00) -- 1994/02/09 (12:00) Earth-Moon Transfer Orbit

4.) 1994/02/09 (12:00) -- 1994/02/21 (01:09) Earth-Moon Transfer Orbit

5.) 1994/05/03 (13:17) -- 1994/05/15 (12:00) Earth Gravity Assist Flyby

6.) 1994/05/15 (12:00) -- 1994/05/27 (18:08) Earth Gravity Assist Flyby

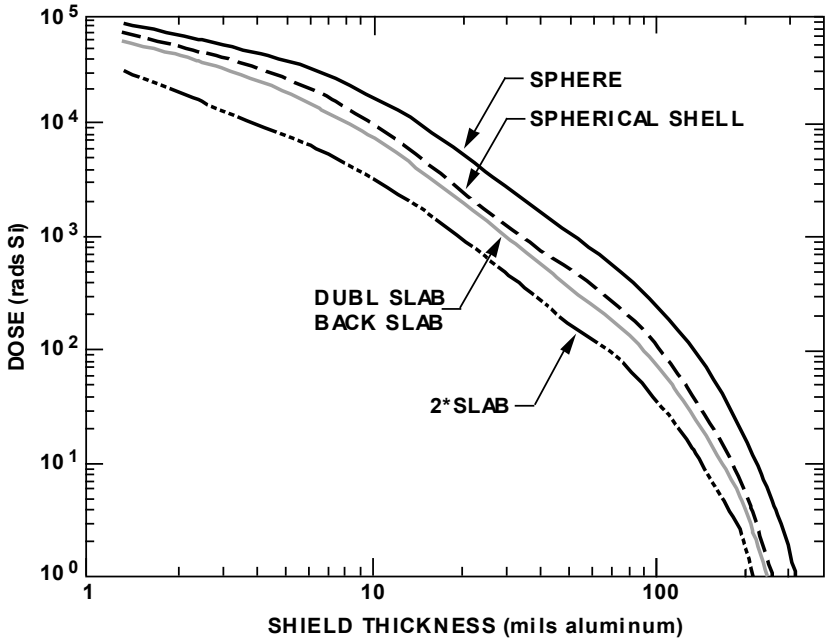

Figure 65. Radiation dosage from the trapped electron environment (AE8) for solar-active conditions and for the first Earth-Moon Transfer Orbit {1994/01/30(07:00)--1994/02/09(12:00)}.

For these orbits, the dosage for the 5 different geometric configurations, solar maximum and solar minimum environmental assumptions, and various shielding thicknesses were calculated so as to provide an estimate of the range of doses to be expected. Radiation doses for electrons, protons, and photons (secondary particles) were calculated for all segments when Clementine would be inside ~11 R_E (the AE8 models are only useful inside ~11 R_E and the AP8 models within ~6 R_E). The results in terms of dosage are presented in Figs. 64 and 65 for two worst case orbital segments–the trapped protons at solar minimum (Fig. 64) and the sum of the trapped electrons at solar maximum and the first transfer orbit (Fig. 65)–and are tabulated in Table 16 for 58 mils of aluminum shielding. Note the wide variation in results for the electrons in Fig. 65—as has been discussed, the precise geometric assumptions can make a big difference in results. The main difference between in the proton results is that between the 2-D and 3-D geometric assumptions–plane surface versus sphere. In many cases, the spherical shell geometry is the most appropriate as it resembles the structure of a spacecraft surrounding circuit boards in the interior of the spacecraft. Spherical shell results for the Clementine interstage mission are summarized in Fig. 66 (the interstage will have a perigee of ~500 km, an apogee of ~160,000 km, and an inclination of 67°). Note that the proton dose due to trapped radiation is very low in comparison to the trapped electrons for the interstage.

Table 16. Summary table for dosage behind 58 mil shielding for the trapped electron (AE8) and trapped proton (AP8) environments. Results correspond to differing levels of geomagnetic activity, geometry, and orbit. Units are rads(Si).

Active Electrons	58 Mils	DOSAGE (Rads)				
Orbit Phase	Date	SPHERE	SPH SHELL	2*SLAB	DUBL SLAB	BACK SLAB
1. Low Earth Orbit	94/01/24	.001150	.000437	.000154	.000315	.000315
2. Earth-Moon Trans	94/01/26	184.000	83.500	32.600	61.300	61.400
3. Earth-Moon Orbit	94/02/04	778.000	359.000	127.000	260.000	260.000
4. Earth-Moon Orbit	94/02/15	466.000	201.000	78.400	143.000	143.000
5. Earth Grav Assist	94/05/06	247.000	88.400	30.100	60.400	60.400
6. Earth Grav Assist	94/05/24	665.000	267.000	107.000	183.000	183.000
	TOTAL DOSE	2340.001	998.900	375.100	707.700	707.800

Active Protons	58 Mils	DOSAGE (Rads)				
Orbit Phase	Date	SPHERE	SPH SHELL	2*SLAB	DUBL SLAB	BACK SLAB
1. Low Earth Orbit	94/01/24	.001800	.001800	.001310	.001310	.001310
2. Earth-Moon Trans	94/01/26	29.000	29.000	9.780	9.780	9.780
3. Earth-Moon Orbit	94/02/04	104.000	104.000	31.900	31.900	31.900
4. Earth-Moon Orbit	94/02/15	66.800	66.800	19.400	19.400	19.400
5. Earth Grav Assist	94/05/06	0.000	0.000	0.000	0.000	0.000
6. Earth Grav Assist	94/05/24	0.000	0.000	0.000	0.000	0.000
	TOTAL DOSE	199.802	199.802	61.081	61.081	61.081

Quiet Electrons	58 Mils	DOSAGE (Rads)				
Orbit Phase	Date	SPHERE	SPH SHELL	2*SLAB	DUBL SLAB	BACK SLAB
1. Low Earth Orbit	94/01/24	.001120	.000434	.000153	.000312	.000312
2. Earth-Moon Trans	94/01/26	128.000	56.300	21.700	41.400	41.400
3. Earth-Moon Orbit	94/02/04	557.000	250.000	87.500	181.000	181.000
4. Earth-Moon Orbit	94/02/15	466.000	201.000	78.400	143.000	143.000
5. Earth Grav Assist	94/05/06	247.000	88.400	30.100	60.400	60.400
6. Earth Grav Assist	94/05/24	665.000	268.000	107.000	183.000	184.000
	TOTAL DOSE	2063.001	863.700	324.700	608.800	609.800

Quiet Protons	58 Mils	DOSAGE (Rads)				
Orbit Phase	Date	SPHERE	SPH SHELL	2*SLAB	DUBL SLAB	BACK SLAB
1. Low Earth Orbit	94/01/24	.001800	.001800	.001310	.001310	.001310
2. Earth-Moon Trans	94/01/26	29.100	29.100	9.830	9.830	9.830
3. Earth-Moon Orbit	94/02/04	104.000	104.000	32.000	32.000	32.000
4. Earth-Moon Orbit	94/02/15	66.700	66.700	19.400	19.400	19.400
5. Earth Grav Assist	94/05/06	0.000	0.000	0.000	0.000	0.000
6. Earth Grav Assist	94/05/24	0.000	0.000	0.000	0.000	0.000
	TOTAL DOSE	199.802	199.802	61.231	61.231	61.231

DOSAGE (Rads)	58 Mils	SPHERE	SPH SHELL	2*SLAB	DUBL SLAB	BACK SLAB
TOTAL ACTIVE DOSE		2539.80	1198.70	436.18	768.78	768.88
TOTAL QUIET DOSE		2262.80	1063.50	385.93	670.03	671.03

4.1.2 Solar Proton Events

The energetic solar proton environment was expected to be the most severe radiation environment for a lunar transfer orbit like that for Clementine—the spacecraft spent little time in the trapped radiation environment as this occurred near perigee—as it spent most of its time at apogee far from the Earth and more directly exposed to the solar flare environment. The maximum dosage expected, as predicted by the JPL model at 1 AU for solar protons, is presented

in Figs. 67 and 68 in terms of the probability of the plotted values not being exceeded for missions of 1 to 7 year durations during the active part of the solar cycle. The model predicts essentially ~0 dosage for the 4 years of solar minimum (roughly May 1995 to May 1999). The results are summarized in Table 17 for a 1 year mission within the current active solar cycle. (The primary Clementine mission was supposed to be from February 1994 to August 1994 while the interstage was supposed to last about 450 days. In actual fact, the interstage decayed into the atmosphere after 3 months and the Clementine itself lost attitude control and signal about 4 months after launch—the spacecraft was briefly re-acquired a little over a year later and long term radiation exposure data in the interplanetary environment were successfully downloaded.) The JPL models provide total mission dosage as a function of expectation. Specifically, they predict the likelihood (expressed as a percentage) that a specified maximum integral fluence will not be exceeded in a given time interval (or, vice versa, for a specified likelihood percentage, the corresponding maximum fluence expected). For the 1 year Clementine mission during solar maximum, the model predicted a dosage equal to or less than 40,000 rads (Si) 99% of the time behind 20 mils of shielding or less than or equal to 2,000 rads (Si) 50% of the time. This method allows a project to establish mission dose levels based on the desired probability of success. (Please refer to Section 2.1.2 for a more detailed explanation of the JPL solar flare model.) The solar proton event model provides design guidelines as to the maximum dosage that can be expected—it is not a hard and fast standard. As such, it can not be used without a properly specified RDM. The RDM is where the project management makes its input—basically the "risk" margin that the project is willing to assume for a solar flare. A typical RDM is a factor of 2 to 4 although higher values are also common.

Table 17. "Worst Case" solar proton dosage predictions for ~1 year Clementine mission scenario. A 58 mil aluminum shell is assumed.

Probability Obs Dose Does Not Exceed Predicted Dose	Predicted Dose Rad(Si)
50%	466
90%	2750
95%	4640
99%	12700

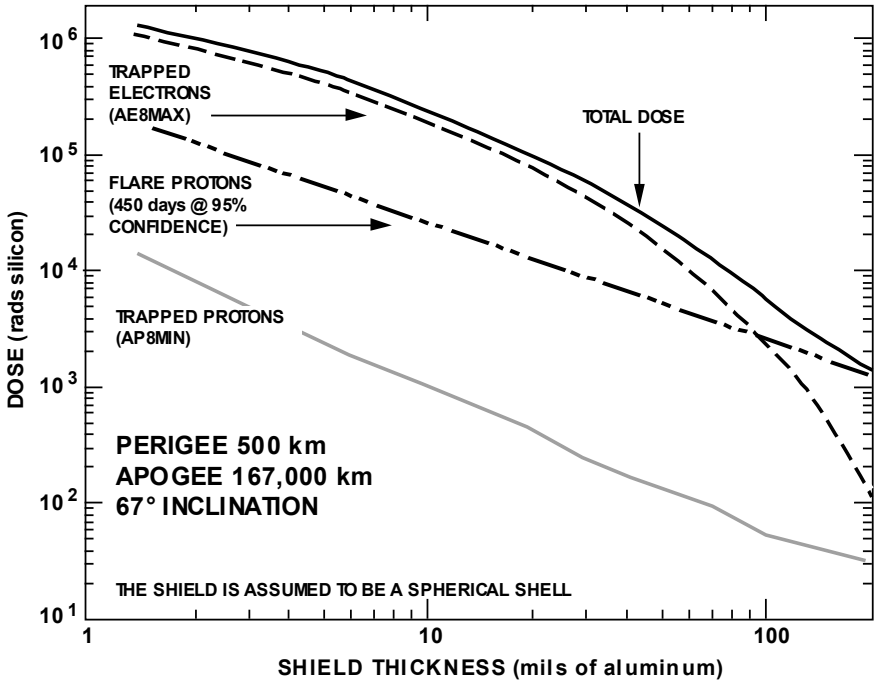

Figure 66. Mission summary plot for the total radiation dose expected for the Clementine Interstage. This assumes a 450 day mission and a 95% confidence flare environment. Dosage is plotted as a function of aluminum shield thickness for a spherical shell geometric configuration.

4.1.3 Summary of Radiation Dosage Estimates

This section has reviewed the radiation environment for a proposed mission, Clementine and its interstage. This exercise has served to demonstrate the practical steps required in carrying out an estimation of the radiation environment within a spacecraft. For this environment, each of the major contributors to radiation dosage (i.e., trapped electrons, trapped protons, and solar flare protons) has been identified. Estimates of the total dose (assuming a 58 mil aluminum shield and a spherical shell) for the trapped environment range from 900 to 1000 rad(Si) for the electrons and ~200 rad(Si) for the protons (as the mission duration is so short, however, deviations of a factor of ~10 are easily likely!). The solar flare proton dosage is, for a 90% probability that the value won't be exceeded, 4600 rad(Si). The corresponding dosages for the interstage give a total dosage of ~10,000 rad(Si) for the electrons, ~100 rad(Si) for the protons, and 4600 rad(Si) for the flare protons (95%). Whatever levels are adopted, it is always necessary to establish a project-defined radiation design margin (RDM). For an RDM of 2 times the predicted dose, this would give ~12 krad(Si) as the maximum design dose for a 58 mil aluminum shell for the Clementine and 30 krad (Si) for the interstage. As a final issue, shielding geometry is clearly a major driver in determining dose, particularly for the electrons. For particularly sensitive components, it is recommended that detailed dosage calculations always be carried out if the initial levels estimated by this process are a cause for concern. Spot shielding and clever placement of the

instruments can significantly lower the dosage that these components see without necessitating their replacement—all steps being followed on the Clementine mission.

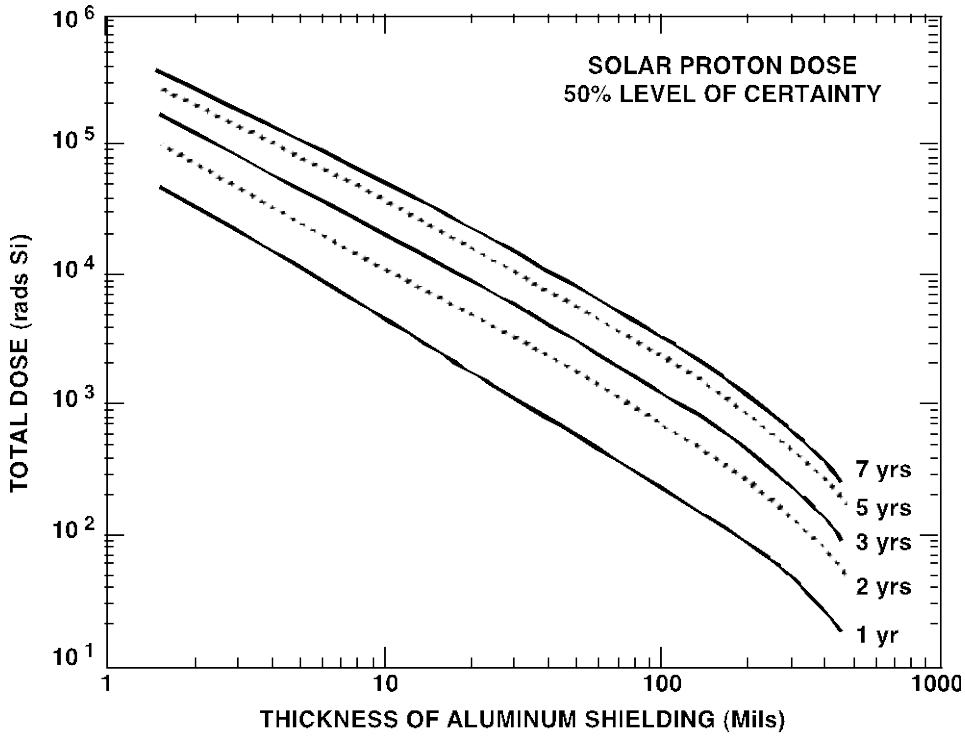

Figure 67. Solar flare proton dosage (rad(Si)) for a 50% probable maximum dose after 1,2,3,5, and 7 years into the active portion of the solar cycle beginning on May 26, 1999. Results are for 1 AU (no magnetospheric shielding).

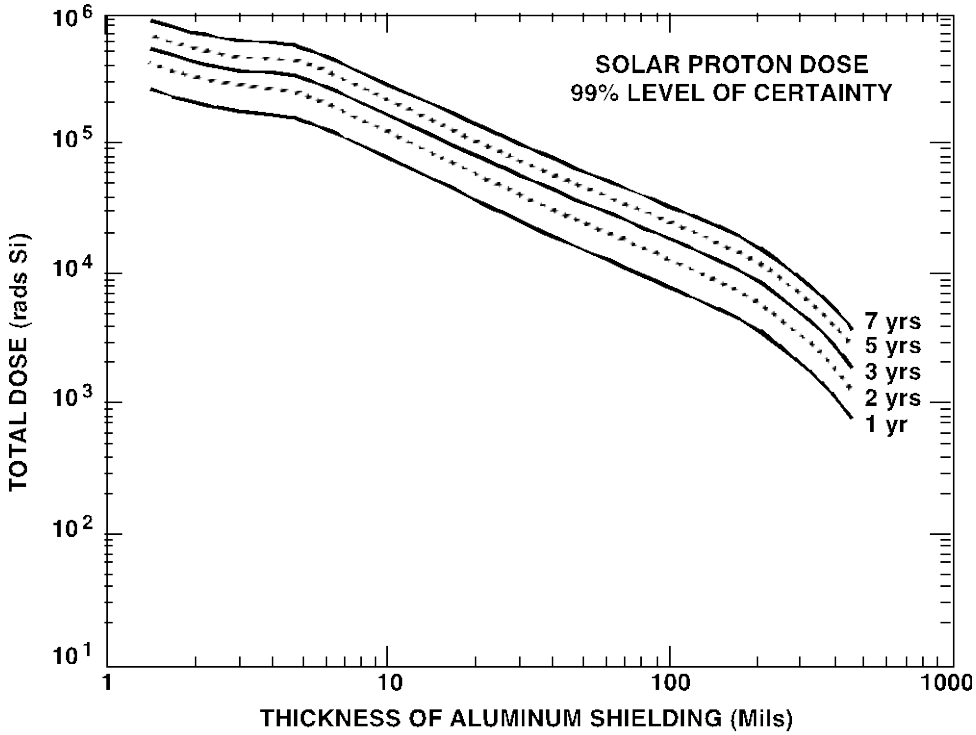

Figure 68. Solar flare proton dosage (rad(Si)) for a 99% probable maximum dose after 1,2,3,5, and 7 years into the active portion of the solar cycle beginning on May 26, 1999. Results are for 1 AU (no magnetospheric shielding).

4.2 Mars Mission

To illustrate a typical interplanetary mission, Fig. 69 shows a sample Mars mission trajectory starting on 25 January 2014 and returning to Earth on 11 July 2016. The external solar proton event mission fluences versus particle energy for the different mission segments are plotted in Fig. 70 for this mission. A 95% mission probability is assumed. The surface segment, because of its much greater duration, represents the dominate fluence source. Based on the fluences and segments in the previous figure, the mission dose versus aluminum shielding (in mils) are computed for the Mars mission. According to these estimates, 1 inch of shielding would imply ~300 rads of dose with a 95% probability—while insignificant for spacecraft systems, this would pose a serious threat for astronauts.

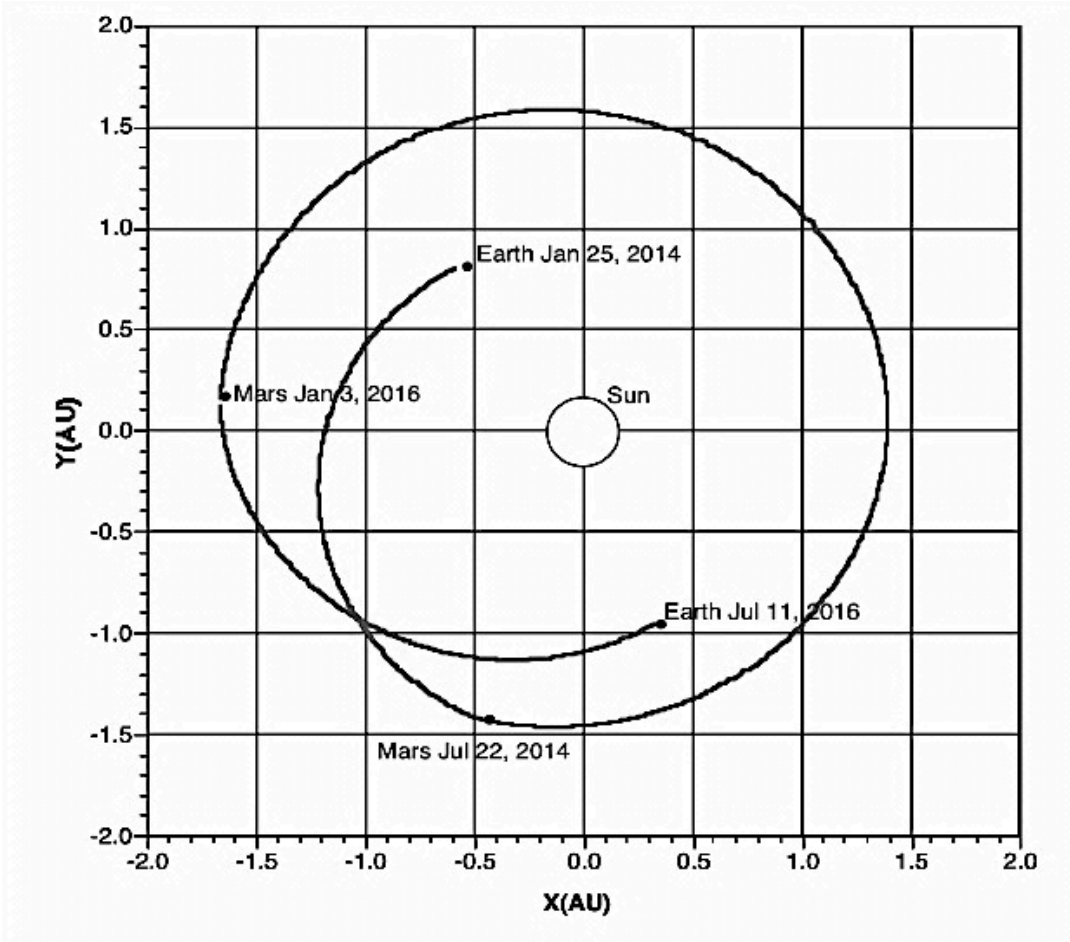

Figure 69. Sample Mars mission trajectory starting on 25 January 2014 and returning to Earth on 11 July 2016.

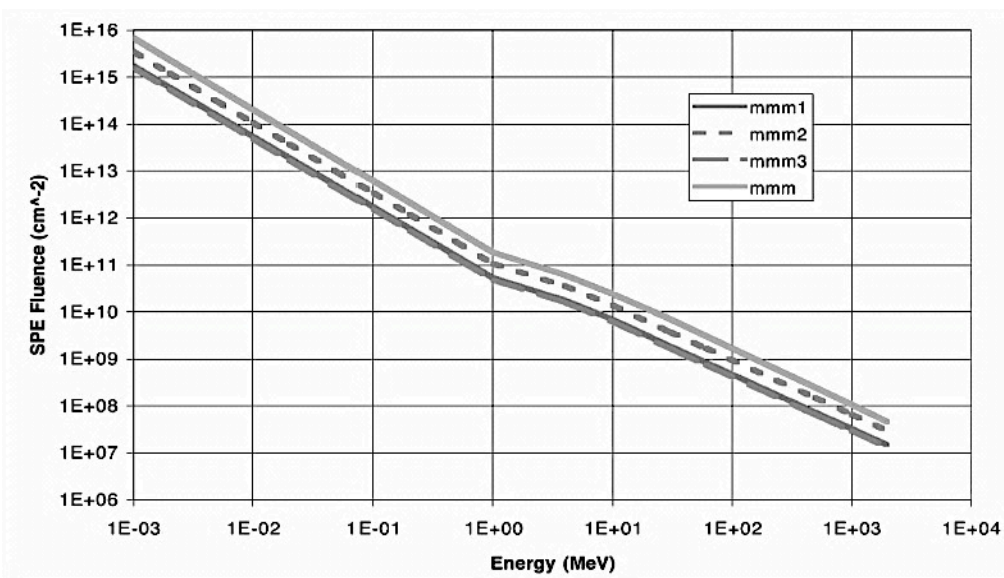

Figure 70. External solar proton event mission fluences versus particle energy for sample Mars mission. "mmm1" is for the Earth to Mars leg. "mmm2" is for the Mars surface stay. "mmm3" is the Mars to Earth leg. "mmm" is the total mission fluence.

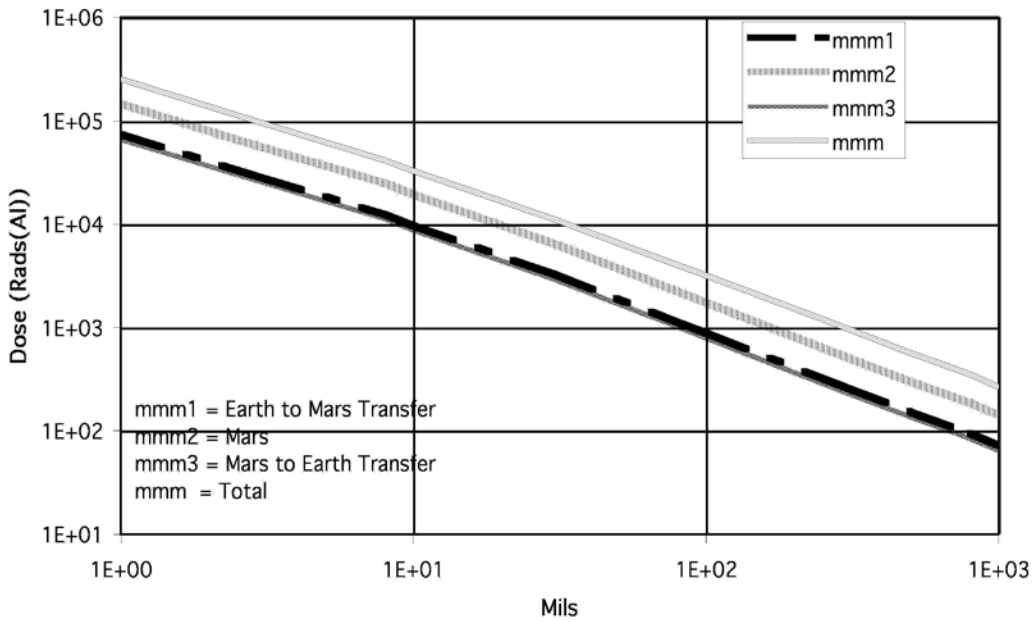

NOTE:95% PROBABILITY FLUENCES FOR 3 SEGMENTS AND TOTAL MISSION
4π SPHERICAL SHIELD OF ALUMINUM IS ASSUMED

Figure 71. Solar proton event mission doses for sample Mars mission corresponding to the segments in Fig. 70.

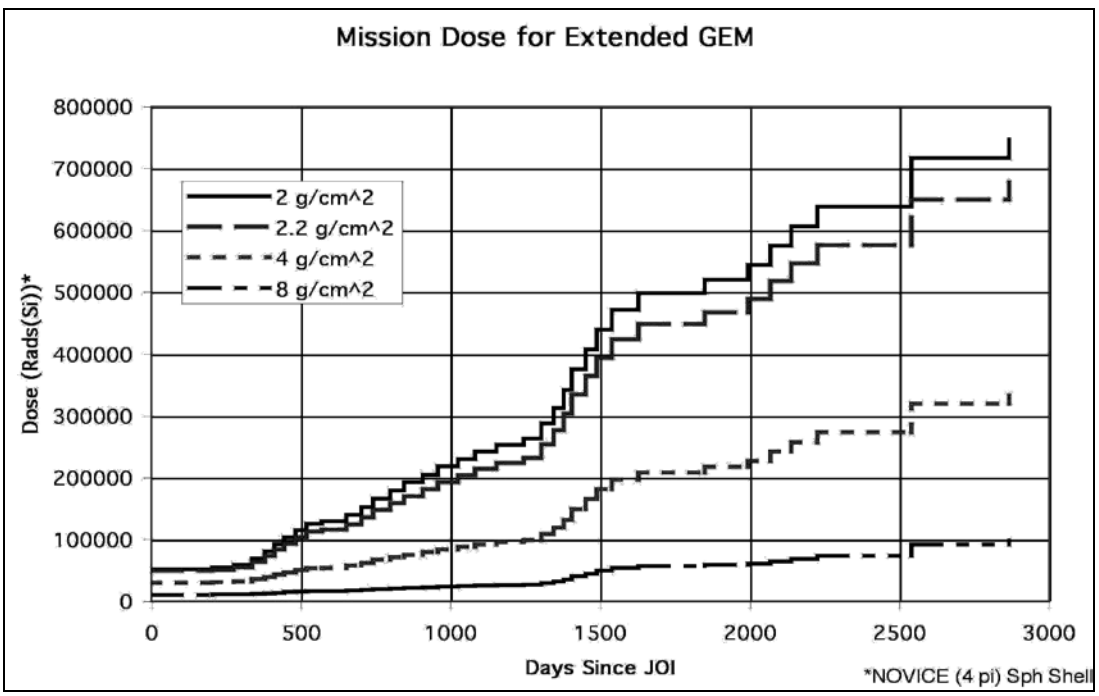

Figure 72. Comparisons of the expected Galileo dose versus time (the steps correspond to perijove passages) the complete mission (~35 orbits) for different shielding levels. 2, 2.2, 4, and 8 g-cm^{-2}. 2.2 g-cm^{-2} was considered the "average" shielding for mission purposes.

4.3 Jovian Model Applications

The JPL jovian trapped radiation models [43, 44] were developed for several practical applications. These applications, as would be expected, ranged from establishing radiation dosage guidelines to single event upset modeling. Two unique applications will be discussed. First consider the effects of total dose. In Fig. 72, the model predictions for the total electron dose expected for Galileo as a function of mission time (the steps correspond to perijove passages) and for different levels of aluminum shielding (2, 2.2, 4, and 8 g-cm^{-2}; 2.2 g-cm^{-2} was considered the "average" shielding for mission purposes). The design hardness level for the Galileo electronic components was ~150 krads(Si) (75 krads with an RDM of 2) for the primary mission. The use and impact of the model in determining the dose levels for the radiation hardness design of Galileo is obvious. That the mission experienced only minor radiation effects and survived over 5 times the design is not only a statement of the value of careful shielding design and part selection for mitigating radiation effects but also serendipity—it was not fully appreciated that Galileo would spend most of its time at apojove well outside the radiation belts and would have time to anneal. This annealing and the time allowed to correct the impact of radiation of the various systems permitted a greatly extended mission.

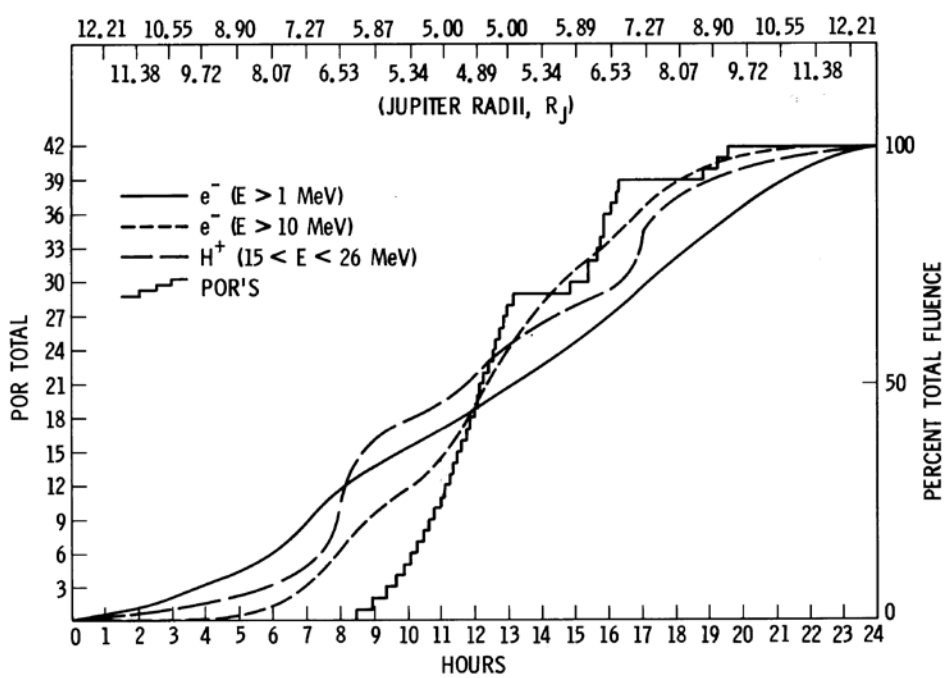

Figure 73. Correlation of Voyager Power On Reset (POR's) Anomalies with the High Energy (E> 1 MeV and E> 10 MeV) Electron Environment. [91]. Also shown for comparison is the high energy proton environment (15 MeV<E<26 MeV).

Another application of the Jupiter radiation model was in studying anomalies on Voyager. During the Voyager I flyby of Jupiter, 42 anomalies were observed. It has been postulated [91] that these anomalies were caused by arc discharges during the flyby. Although surface charging was ruled out as a possible cause, subsequent estimates of the total electron fluence indicated that there was a sufficient radiation environment of high energy electrons present to cause IESD. That is, it has been proposed that the E>~100 KeV electron environment deposited sufficient charge in an external cable on Voyager to generate arc discharges that could cause POR anomalies. To test this assumption, the total fluence of electrons at E>1 MeV and E>10 MeV and protons between 15<E<26 MeV were computed as a function of time. The resulting normalized curves are plotted versus the cumulative sum of Voyager POR anomalies in Fig. 73 (cumulative was used as the charge buildup is a cumulative process). As this figure implies, IESD-caused charging is the likely source of the Voyager anomalies in a temporal sense as the energetic electron fluence roughly follows the pattern of POR events. The major evidence for buried charge as the cause, however, came from an estimate of the charge deposited in each arc that would be necessary to cause the observed POR upsets. This indicated that the total E>100 KeV (i.e., the minimum energy necessary to penetrate several mils of shielding and deposit charge) electron fluence was very close to the actual level required to account for all 42 arcs (~10^{10} e-cm^{-2} per event). This is believed to be one of the earliest examples of internal arc discharges occurring in space ever published and demonstrates another application of radiation modeling. Subsequent ground testing of the Galileo vehicle supported the buried charge hypothesis and revealed several potential sources of such arcing that led to its redesign.

4.4 Heinrich Flux Estimates

In addition to total mission dose and IESD, SEU effects are another critical component of a radiation analysis. The Heinrich flux curve is the starting point for most SEU calculations. Here, several practical examples of the effects of source, location, and shielding will be presented. These calculations are based primarily on the results of Adams [92]. Fig. 74 is the first example and illustrates the effects of shielding on the solar flare and GCR environments in interplanetary space. Fig. 74a is a Heinrich curve showing the effects aluminum shielding (0.173 g-cm^{-2} (0.064 cm) to 10.8 g-cm^{-2} (4.0 cm)) has on a severe solar proton event. This event is assumed to have the same spectrum as the worst case August 4, 1972 flare and a 90% worst case enrichment of the heavy ions [9]. Fig. 74b is a similar plot for the effects of shielding on the GCR (elements 1 to 26). The aluminum shielding in this example ranges from 2 g-cm^{-2} (.74 cm) to 100 g-cm^{-2} (37 cm)–a very thick shield. It is clear from these plots that the solar proton event environment, dominated by protons, can be fairly effectively attenuated by shielding whereas the GCR environment is little effected even for the lighter components. Even so, the GCR environment does not begin to dominate until LETs well above 20-30 MeV-cm^{2}-mg^{-1}.

Next consider the effects of magnetospheric shielding. In Fig. 75 [92], the Heinrich integral flux diagram for a spacecraft with 0.064 cm of aluminum shielding is graphed as a function of orbital inclination at an altitude of 400 km. A 90% (Adams) worst case event and an AP8 trapped proton environment are assumed. As noted by Adams [92], below an LET of 0.5 MeV-cm^{2}-mg^{-1}, the population is dominated by the trapped protons. As the LET increases and the inclination increases, more and more event particles can penetrate to the spacecraft. The steps correspond to the large drops in abundance beyond iron, nickel, bismuth, and uranium in the Adams model of the heavy ions. Fig. 76, for the same environment, illustrates the variations produced by increasing the altitude for a 60° inclination orbit and for 0.064 cm of aluminum shielding. What variations exist are primarily below 0.5 MeV-cm^{2}-mg^{-1} and are due almost entirely to the trapped proton environment. These variations go through a maximum between 4000 and 6000 km.

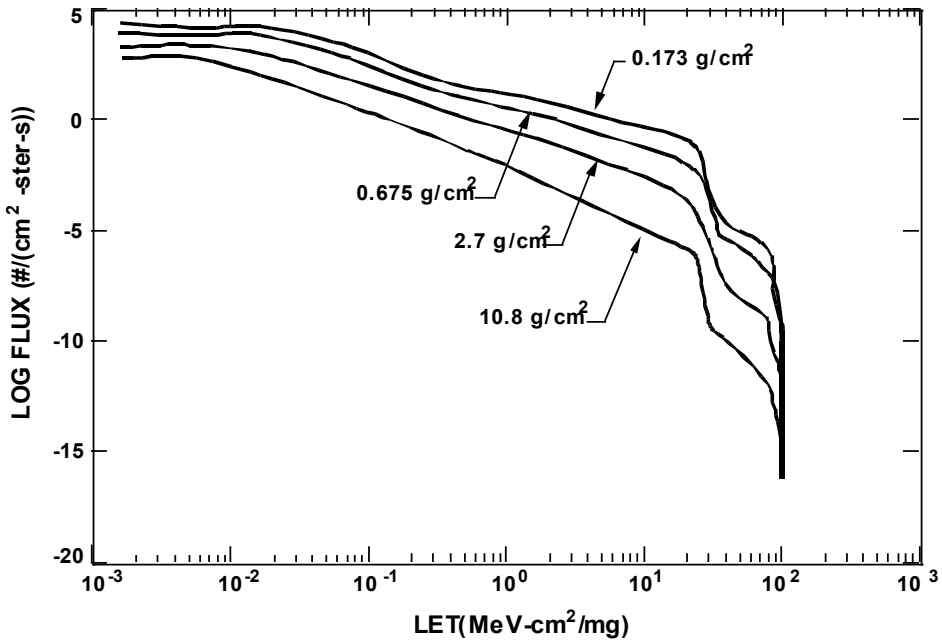

(A)

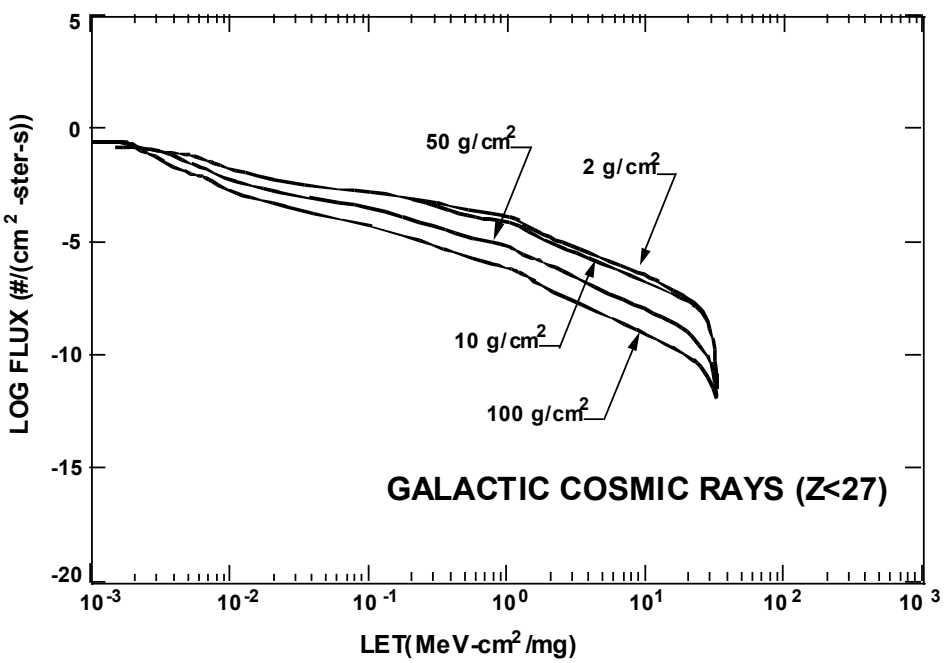

(B)

Figure 74. Integral LET spectra as functions of spacecraft wall thickness for A) the Adam's worst case composite solar flare [92, 93] and B) the GCR environment (elements 1 to 26) [92, 93].

Of what value are these results? First, they predict that, even for substantial levels of shielding, the solar flare environment normally will dominate SEU calculations even at high LET levels in interplanetary space. Indeed, these figures provide upper limits on the SEU environment expected at 1 AU (for no magnetospheric shielding). Second, given the increasing importance of solar flares to the overall SEU environment, statistical techniques such as

represented by the JPL solar events models will need to be utilized for predicting SEU effects. Third, in Earth orbit, the picture is very complex because of geomagnetic shielding, but, at low LETs (i.e., LET < 5-10 MeV-cm^2-mg^{-1}), the trapped protons will normally dominate the environment. Unfortunately, with the desire to fly "commercial parts" and CCDs, these LET levels, which have previously been too low to be of concern, are beginning to become an issue as part sensitivities approach LETs of 1 to 10 MeV-cm^2-mg^{-1}.

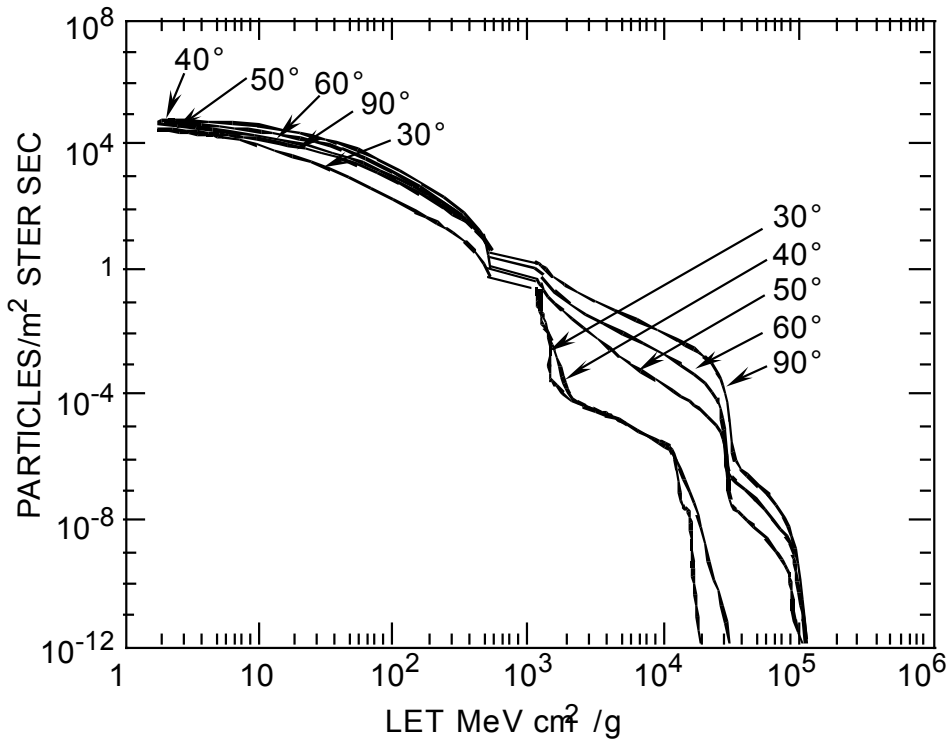

Figure 75. Integral LET spectra inside a spacecraft (with 0.064 cm aluminum walls) in a 400 km circular orbit [92]. The 90% worst case environment is assumed in the interplanetary medium and the GSFC AP trapped proton environment at the Earth. The LET spectra are for the various orbital inclinations indicated.

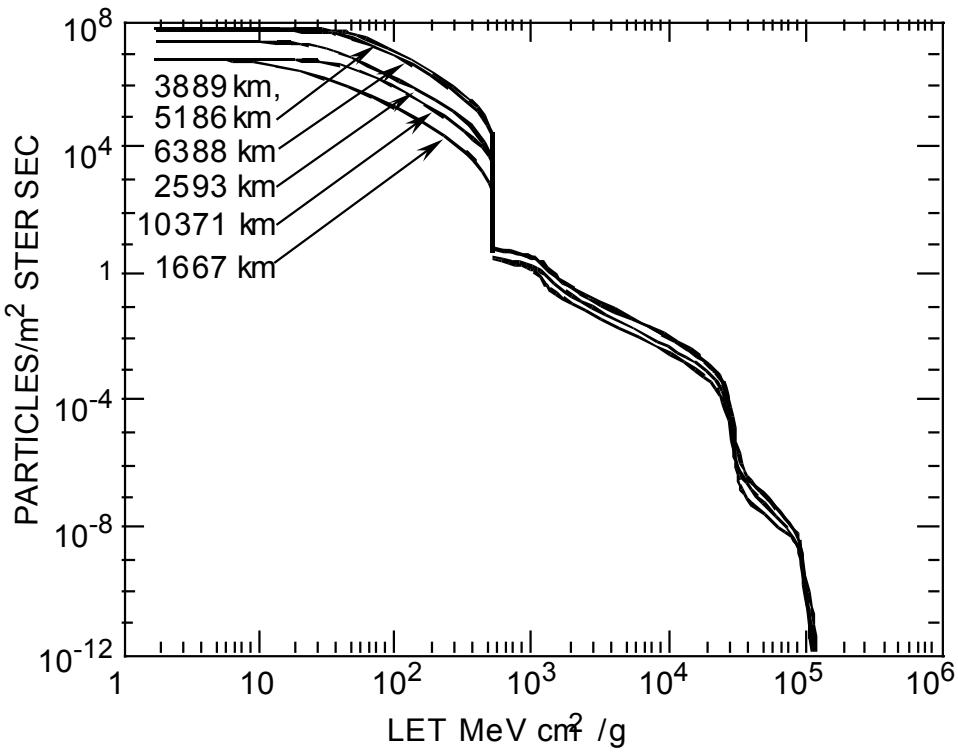

Figure 76. Integral LET spectra inside a spacecraft with 0.064 cm aluminum walls that is in a circular orbit at a 60° inclination [92]. As in Fig. 75, the 90% worst case environment is assumed in the interplanetary medium and the GSFC AP trapped proton environment at the Earth. The LET spectra are for the various altitudes as shown.

5 Conclusion

The objectives of this section were to address 3 aspects of the radiation problem. First, a review was provided of the natural and man-made space radiation environments. This description included both particulate and, where applicable, electromagnetic (i.e., photon) environments. Secondly, the methods used to propagate the external environment through the complex spacecraft structures surrounding the point where the internal radiation environment was required were discussed. Finally, examples of the environment inside the spacecraft were presented. While it was not intended to treat in detail all aspects of the problem of the radiation environment within a spacecraft, by dividing the problem into these 3 parts—external environment, propagation, and internal environment—a basis for understanding the process of predicting the internal spacecraft radiation environment has been established. The consequences of this environment are discussed by the other presenters at this seminar.

6 Acknowledgements

Copyright 2011 California Institute of Technology. Government sponsorship acknowledged. The research was carried out at the Jet Propulsion Laboratory, California

Institute of Technology, under a contract with the National Aeronautics and Space Administration.

References

[1] E. U. Condon and H. Odishaw, *Handbook of Physics*, 2 ed. New York: McGraw-Hill, 1967.

[2] J. G. Roederer, *Dynamics of Geomagnetically Trapped Radiation* vol. 2. New York: Springer-Verlag, 1970.

[3] J. H. Adams, Jr., "Cosmic Ray Effects on Microelectronics, Part IV," Naval Research Laboratory, Washington D.C. NRL Memorandum Report 5901, 1986.

[4] V. A. J. van Lint, "Radiation Effects Testing Short Course," in *IEEE 1986 Nuclear and Space Radiation Effects Conference*, Providence, Rhode Island, 1986, p. 12.

[5] E. L. Petersen, "Single Event Upsets in Space: Basic Concepts," in *Tutorial Short Course, IEEE Nuclear and Space Radiation Effects Conference*, Gatlinburg, Tenn., 1983, p. 15.

[6] D. F. Smart and M. A. Shea, "Galactic Cosmic Radiation and Solar Energetic Particles," in *Handbook of Geophysics and the Space Environment*. Accession No. ADA 167000, A. S. Jursa, Ed. Springfield, VA: National Technical Information Service, 1985, Chapter 6.

[7] J. Feynman, T. P. Armstrong, L. Dao-Gibner, and S. M. Silverman, "A New Interplanetary Proton Fluence Model," *J. Spacecraft,* vol. 27, p. 403, 1990.

[8] J. H. Adams, Jr. , J. R. Letaw, and D. F. Smart, "Cosmic Ray Effects on Microelectronics, Part II: The Geomagnetic Cutoff Effects," Naval Research Laboratory, Washington D.C. NRL Memorandum Report 4506, May 1983.

[9] J. H. Adams, Jr. , R. Silverberg, and C. H. Tsao, "Cosmic Ray Effects on Microelectronics, Part I: The Near-Earth Particle Environment," Naval Research Laboratory, Washington D.C. NRL Memorandum Report 4506, August 25 1981.

[10] C. H. Tsao, R. Silberberg, J. H. Adams, Jr., and J. R. Letaw, "Cosmic Ray Effects on Microelectronics, Part III: Propagation of Cosmic Rays in the Atmosphere," Naval Research Laboratory, Washington D.C. NRL Memorandum Report 4506, August 9 1984.

[11] J. Barth, "Solar Particle Events," in *IEEE NSREC Short Course Session I*, 2000.

[12] J. Feynman and S. Gabriel, "Interplanetary Particle Environment, Proceedings of a Conference," JPL 88-28, Pasadena, CA: Jet Propulsion Laboratory, 1988, p. 167.

[13] A. Luhn, B. Klecjer, D. Movestact, G. Gloeckler, F. M. Ipavich, M. Scholer, C. Y. Fan, and A. Fisk, "Ionic Charge States of N, Ne, Mg, Si, S in Solar Particle Events," *Advances in Space Research,* vol. 4, pp. 161-164, 1984.

[14] S. Fischer, K. Vandas, B. Kuznetsov, and R. Ramatay, "Determination of the Effective Charge of Solar Cosmic Ray Nuclei Using the Earth's Magnetic Field," in *Advances in Space Research*. vol. 4, 1984, pp. 169-172.

[15] R. A. MeWaldt and E. C. Stone, "A Search for Deuterium Tritium and ^{3}He in Large Solar Flares." vol. 66 Bull. of the Am. Phys. Soc., 1983, p. 742.

[16] H. H. Breneman and E. C. Stone, "Solar and Photospheric Abundance from Solar Energetic Particle Measurements," *Astrophys. J.,* vol. 229, pp. L57-61, 1985.

[17] O. R. White, "The Solar Output and its Variation," Boulder, CO: Colorado Associated University Press, 1977.

[18] H. B. Garrett and J. M. Forbes, "A Model of Solar Flux Attenuation During Eclipse Passage and Its Effects on Photoelectron Emission from Satellite Surfaces," *Planet.*

Space Sci., vol. 29, pp. 601-607, 1981.
[19] J. H. Allen, "GOES X-Ray Measurements," *EOS,* 1985.
[20] T. N. Divine, "Interplanetary Charged Particle Models," NASA SP-8118, March 1975.
[21] J. A. Van Allen, *Geomagnetically Trapped Radiation*. New York-London: J. Wiley & Sons, Inc., 1963.
[22] D. J. Knecht and B. Shuman, *The Geomagnetic Field*, Accession No. ADA 167000. Springfield, VA: National Technical Information Service, 1985.
[23] W. P. Olson and K. A. Pfitzer, "A Quantitative Model of the Magnetospheric Magnetic Field," *J. Geophys. Res.,* vol. 79, p. 3739, 1974.
[24] Tsyganenko, "A Model of the Cis-Lunar Magnetospheric Field," *Annals. Geophys.,* vol. 32, pp. 1-12, 1976.
[25] G. H. Voigt, "A three dimensional, analytical magnetospheric model with defined magnetopause," *Z. Geophys.,* vol. 38, pp. 319-346, 1972.
[26] D. R. Barraclough, "International Geomagnetic Reference Field: The 4th Generation," *Physics of the Earth and Planetary Interiors,* vol. 48, p. 279, 1987.
[27] C. C. Finlay, S. Maus, C. D. Beggan, T. N. Bondar, A. Chambodut, T. A. Chernova, A. Chulliat, V. P. Golovkov, B. Hamilton, M. Hamoudi, R. Holme, G. Hulot, W. Kuang, B. Langlais, V. Lesur, F. J. Lowes, H. Luhr, S. Macmillan, M. Mandea, S. McLean, C. Manoj, M. Menvielle, I. Michaelis, N. Olsen, J. Rauberg, M. Rother, T. J. Sabaka, A. Tangborn, L. Toffner-Clausen, E. Thebault, A. W. P. Thomson, I. Wardinski, Z. Wei, and T. I. Zvereva, "International Geomagnetic Reference Field: the eleventh generation (International Association of Geomagnetism and Aeronomy, Working Group V-MOD)," *Geophys. J. Int.,* vol. 183, pp. 1216-1230, December 2010.
[28] M. Walt, *Introduction to Geomagnetically Trapped Radiation* Cambridge, UK: Cambridge University Press, 2005.
[29] M. S. Gussenhoven, E. G. Mullen, D. H. Brautigam, E. Holeman, C. Jordan, F. Hanser, and B. Dichter, "Preliminary comparison of dose measurements on CRRES to NASA model predictions," *IEEE Trans. Nuc. Sci.,* vol. 38, pp. 1655-1662, 1991.
[30] J. I. Vette, "The AE-8 Trapped Electron Model Environment," NSSDC/WDC-A-R&S 91-24, November 1991.
[31] J. I. Vette, M. J. Teague, D. M. Sawyer, and K. W. Chan, "Modeling the Earth's Radiation Belts," in *Solar-Terrestrial Prediction Proceedings*, Boulder, 1979.
[32] D. M. Sawyer and J. I. Vette, "AP-8 Trapped Proton Environment for Solar Maximum and Solar Minimum," NSSDC/WDC-A-R&S 76-06, 1976.
[33] A. L. Vampola, "The Space Particle Environment," in *Materials in Space*, Langley Res. Cntr., 1988.
[34] R. E. Smith and G. S. West, "Space and Planetary Environment Criteria Guidelines for Use in Space Vehicle Development, 1982 Revision." vol. 1, TM-82478: NASA, 1983.
[35] J. S. Chang, S. M. L. Prokopenko, R. Goddard, and J. G. Laframboise, "Prediction of Ion Drift Effects on Spacecraft Floating Potentials," in *Spacecraft Charging Technology-1978*, 1979, pp. 179-187.
[36] K. Chan, M. J. Teague, N. Schofield, and J. I. Vette, "Modeling of electron time variations in the radiation belts," in *Quantitative Modeling of Magnetospheric Processes*, W. P. Olson, Ed. Washington, D.C.: American Geophysical Union, 1979, p. 121.
[37] J. B. Blake and L. M. Friesen, "A Technique to Determine the Charge State of the Anomalous Low Energy Cosmic Rays," in *15th International Cosmic Ray Conference*, Plovdiv, 1977, p. 341.
[38] J. M. Cornwall, "Radial Diffusion of Ionized Helium and Proton: A Probe for

Magnetospheric Dynamics," *J. Geophy. Res.,* vol. 77, p. 1756, 1972.
[39] T. A. Fritz and W. N. Spjeldvik, "Simultaneous Quiet Time Observations of Energetic Radiation Belt Protons and Helium Ions: the Equatorial α/p Ratio Near 1 MeV," *J. Geophys. Res.,* vol. 84, pp. 2608-2618, 1979.
[40] W. N. Spjeldvik and T. A. Fritz, "Theory of Charge States of Energetic Oxygen Ions in the Earth's Radiation Belts," *J. Geophys. Res.,* vol. 83, p. 1583, 1978.
[41] G. P. Ginet and T. P. O'Brien, "AP-9/AE-9: New Radiation Specification Models--Overview," in *AP-9/AE-9 Introductory Briefing*, 2010.
[42] Anon., "Physics of the Jovian and Saturnian Magnetospheres, Highlights of Conference," in *Physics of the Jovian and Saturnian Magnetospheres*, John Hopkins University, 1981.
[43] T. N. Divine and H. B. Garrett, "Charged particle distributions in Jupiter's magnetosphere," *J. Geophys. Res.,* vol. 88, pp. 6889-6903, 1983.
[44] H. B. Garrett, I. Jun, J. M. Ratliff, R. W. Evans, G. A. Clough, and R. W. McEntire, "Galileo Interim Radiation Electron Model," JPL Publication 03-006, The Jet Propulsion Laboratory, California Institute of Technology, Pasadena, CA, 2003.
[45] A. Sicard-Piet and S. Bourdarie, "Physical Electron Belt Model from Jupiter's surface to the orbit of Europa," *J. Geophys. Res.,* vol. 109, 2004.
[46] A. Sicard-Piet and S. Bourdarie, "JOSE (JOvian Specification Environment)," February 2010.
[47] H. B. Garrett, S. M. Levin, S. J. Bolton, R. W. Evans, and B. Bhattacharya, "A revised model of Jupiter's inner electron belts: Updating the Divine radiation model," *Geophys. Res. Lttrs.,* vol. 32, p. 5, 2005.
[48] F. D. Drake and H. Havatum, "Non-thermal microwave radiation from Jupiter," *Astron. J.,* vol. 64, pp. 329-330, 1959.
[49] N. M. Brice and G. A. Ioannidis, "The magnetospheres of Jupiter and Earth," *Icarus,* vol. 13, pp. 173-183, 1970.
[50] G. Ioannidis and N. Brice, "Plasma densities in the Jovian magnetosphere: Plasma slingshot or Maxwell demon?," *Icarus,* vol. 14, pp. 360-363, 1971.
[51] A. J. Dessler, "Physics of the Jovian Magnetosphere," in *Cambridge Planetary Science Series*, W. I. Axford, G. E. Hunt, and R. Greeley, Eds. New York: Cambridge University Press, 1983, p. 544.
[52] N. Gehrels, "Jupiter," Tucson, AZ: University of Arizona Press, 1976.
[53] E. J. Smith, L. Davis, Jr., and D. E. Jones, "Jupiter's magnetic field and magnetosphere," in *Jupiter*, T. Gehrels, Ed. Tucson, AZ: University of Arizona Press, 1976, pp. 788-829.
[54] M. H. Acuna and N. F. Ness, "Results from the GSFC Fluxgate Magnetometer on Pioneer 11," in *Jupiter*, T. Gehrels, Ed. Tucson, AZ: University of Arizona Press, 1976, p. 830-847.
[55] M. H. Acuna and N. F. Ness, "The main magnetic field of Jupiter," *J. Geophys. Res.,* vol. 81, pp. 2917-2922, 1976.
[56] Anon., "Highlights of Conference," in *Physics of the Jovian and Saturnian Magnetospheres*, John Hopkins University, 1981.
[57] J. E. Connerney, M. H. Acuna, N. F. Ness, and T. Satoh, "New models of Jupiter's magnetic field constrained by the Io flux tube footprint," *J. Geophys. Res.,* vol. 103, pp. 11929-11940, 1998.
[58] J. E. P. Connerney, "Magnetic fields of the outer planets," *J. Geophys. Res.,* vol. 98, pp. 18,659–18,679, 1993.
[59] P. K. Seidelmann and T. N. Divine, "Evaluation of Jupiter longitudes in System III (1965)," *Geophys. Res. Lett.,* vol. 4, pp. 65-68, 1977.

[60] K. K. Khurana and H. K. Schwarzl, "Global structure of Jupiter's magnetospheric current sheet," *J. Geophys. Res.,* vol. 110, 2005.
[61] S. M. Krimigis, T. P. Armstrong, A. I. Axford, C. O. Bostrom, G. Gloeckler, E. P. Keath, L. J. Lanzerotti, J. F. Carbary, D. C. Hamilton, and E. C. Roelof, "Low-energy charged particles in Saturn's magnetosphere: Results from Voyager 1," *Science,* vol. 212, pp. 225-231, 1981.
[62] T. N. Divine, "Numerical Models for Electron and Proton Distributions in Saturn's Radiation Belts," Jet Propulsion Laboratory IOM 5217-90-029, February 28, 1990.
[63] H. B. Garrett, J. M. Ratliff, and R. W. Evans, "Saturn Radiation (SATRAD) Model," October 2005.
[64] P. R. Meyer, R. Ramaty, and R. Webber, "Cosmic Rays - Astronomy with Energetic Particles," in *Physics Today*. vol. Oct., 1974.
[65] D. F. Smart and M. A. Shea, (Private Communication), 1989.
[66] R. A. Nymmik, M. I. Panasyuk, T. I. Pervaja, and A. A. Suslov, "A Model of Galactic Cosmic Ray Fluxes," *Nucl. Tracks and Radiat. Meas.,* vol. 20, pp. 427-429, 1992.
[67] J. H. Adams, Jr., A. F. Barghouty, M. H. Mendenhall, R. A. Reed, B. Sierawski, J. W. Watts, and R. A. Weller, "The Revised Space Environment Models in CRÈME-MC, a replacement for CREME96," https://creme-mc.isde.vanderbilt.edu/, 2010.
[68] R. A. Nymmik, M. I. Panasyuk, and A. A. Suslov, "Galactic cosmic ray flux simulation and prediction," *Adv. Space Res.,* vol. 17, 1996.
[69] J. R. Jokipii, E. H. Levy, and W. B. Hubbard, "Effects of Particle Drift on Cosmic Ray Transport. I. General Properties," *Astrophys. J.,* vol. 213, p. 861, 1977.
[70] L. A. Fisk, B. Kpzlovsky, and R. Ramaty, *Astrophys. J. (Lttrs.),* vol. 190, pp. 135-137, 1974.
[71] E. S. Claflin and R. S. White, "A study of equatorial inner belt protons from 2 to 200 MeV," *J. Geophys. Res.,* vol. 79, p. 959, 1974.
[72] H. Mannheimer, "Environmental Impact Statement for Galileo and Ulysses Missions," NASA Office of Space Transportation, January, 1986.
[73] D. F. Salisbury, "Radiation Risk and Planetary Exploration—The RTG Controversy," *The Planetary Report,* vol. VII, pp. 3-7, 1987.
[74] A. Hoffman, "Galileo Orbiter Functional Requirements Book, Environmental Design Requirements," JPL GAL-3-240, Rev. C, May 21, 1987.
[75] H. C. Koons, J. E. Mazur, R. S. Selesnick, J. B. Blake, J. F. Fennell, J. L. Roeder, and P. C. Anderson, "The Impact of the Space Environment on Space Systems," in *Proceeding of the 6th Spacecraft Charging Technology Conference*, 2000.
[76] H. B. Garrett and A. C. Whittlesey, "Mitigating In-Space Charging Effects--A Guideline," NASA-HDBK-4002A, Washington, DC National Aeronautics and Space Administration, 2011.
[77] P. D. Group, "Passage of Particles through Matter; Review of Particle Properties," *Phys. Lttrs., B,* vol. 239, pp. 1-38, 1990.
[78] P. S. Winokur, "Total-Dose Radiation Effects (From the Perspective of the Experimentalist)," in *IEEE Nuclear and Space Radiation Effects Conference Short Course*, New Orleans, LA, 1992, p. 68.
[79] M. J. Berger and S. M. Seltzer, "Penetration of Electrons and Associated Bremsstrahlung through Aluminum Targets," NASA, Washington, DC, SP-169, pp. 285-322, 1968.
[80] J. F. Janni, "Proton Range-Energy Tables, 1 keV-10 GeV, Part 1." vol. 27, Atomic Data and Nuclear Data Tables, 1982, pp. 150-339.
[81] J. F. Janni, "Proton Range-Energy Tables, 1 keV-10 GeV, Part 2," vol. 27, Atomic Data

and Nuclear Data Tables, 1982, pp. 341-529.
[82] D. B. Brown, "Total Dose Effects at Dose Rates Typical of Space," in *NSREC Short Course*, 1990, pp. 9-10.
[83] L. Curgenven and P. Duncumb, "Report 303," Tube Investments Research Laboratories July 28, 1971.
[84] E. G. Stassinopoulos, "Electron Depth-Dose Profiles in CaFMn TLDs," (Personal Communications), 1993.
[85] E. G. Stassinopoulos, "Proton Energy Deposition in CaF_2," (Personal Communications), 1993.
[86] T. M. Jordon, "Electron Dose Attenuation Kernels for Slab and Spherical Geometries," AF Weapons Laboratory, AFWL-TR-81-43, November 1981.
[87] T. M. Jordon, "NOVICE: A Radiation Transport/Shielding Code; Users Guide," Experimental and Mathematical Physics Consultants, 87.01.02.01, January 2, 1987.
[88] R. D. Evans, *The Atomic Nucleus*: McGraw-Hill,1955 [reprinted Kliegler Publishing], 1982.
[89] E. Fermi, *Nuclear Physics*. Chicago, IL: University of Chicago Press, 1950.
[90] V. A. J. van Lint, T. M. Flanagan, R. E. Leadon, J. A. Naber, and V. C. Rogers, *Mechanisms of Radiation Effects in Electronic Materials* vol. 1. New York, NY: Wiley-Interscience, 1980.
[91] P. Leung, A. C. Whittlesey, H. B. Garrett, P. A. Robinson, Jr., and T. N. Divine, "Environment-Induced Electrostatic Discharges as the Cause of Voyager 1 Power-On Resets," *J. Spacecraft,* vol. 23, pp. 323-330, 1986.
[92] J. H. Adams, Jr., "The Ionizing Particle Environment Near Earth," in *AIAA Aerospace Sciences Meeting*, 1982, p. 7.
[93] F. W. Sexton, "Measurement of Single Event Phenomena in Devices and ICs," in *IEEE Nuclear and Space Radiation Effects Conference Short Course*, New Orleans, LA, 1992, p. 68.